



UNIVERSITÀ DEGLI STUDI DI PADOVA

Dipartimento di Fisica e Astronomia “Galileo Galilei”

Corso di Laurea Magistrale in Fisica

Phase I of the ANNIE experiment: Data Acquisition system and preliminary data analysis

RELATORE

Dott. Gianmaria Collazuol

CANDIDATO:

Tommaso Boschi
matr. 1105506

CORRELATORI:

Prof. Francesca Di Lodovico (QMUL)
Dr. Benjamin Richards (QMUL)

*Agli amici più grandi.
A chi ho perso per strada.*

Overview

This thesis is placed within the context of the The Accelerator Neutrino Neutron Interaction Experiment (ANNIE), a water Cherenkov detector built at the Fermi National Accelerator Laboratory. The main aim of ANNIE is to study in depth the nature of neutrino-nucleus interactions by analysing the yield of final state neutrons produced in this kind of interactions. New technologies, such as gadolinium-loaded water and, for the first time, Large Area Picosecond Photodetectors (LAPPDs) will be also employed in future phases of the experiment. The measurement will have relevant implications for next generation Water Cherenkov detectors, in that these techniques may play a significant role in reducing backgrounds in relation to proton decay measurements, supernova neutrino observations and neutrino interaction physics.

This paper deals with the Phase I of the experiment, in which photomultipliers (PMT) are adopted within the tank and the forward Veto and the Muon Range Detector (MRD) are partially being employed. A small container, called Neutron Volume Capture (NVC) is also inside the tank, for preliminary neutron yield studies. The main work of the thesis consists of the development of the CAMAC electronics Data Acquisition system (DAQ); the already existing VME electronics DAQ, for the water PMTs, is described. Early stage data are also analysed, and event reconstruction techniques are proposed.

The R&D activities were undertaken in the Particle Physics Research Group of the Queen Mary University of London.

This thesis is divided as follows:

Chapter 1 Neutrino Physics is briefly introduced, as well as some experimental techniques for their detection.

Chapter 2 The concept and the apparatus of ANNIE is described.

Chapter 3 The DAQ system is illustrated and some future developments are proposed.

Chapter ?? The data analysis algorithm, developed for signal/noise discrimination, is shown.

Chapter 5 The analysis procedures are applied to preliminary data sets and their validity are also tested.

Chapter 6 Conclusion.

Contents

Overview	iii
1 Introduction	1
1.1 Neutrino interactions	2
1.2 Neutrino detection	5
1.2.1 Water cherenkov	6
1.2.2 Gadolinium neutron capture	7
1.3 Neutrino Production	9
2 The ANNIE Experiment	11
2.1 Physics of the experiment	12
2.2 Neutrino beam	14
2.3 The Hall	15
2.3.1 Water tank	15
2.3.2 Photodetectors	17
2.3.3 Veto and MRD	19
3 Data Acquisition	21
3.1 Main DAQ Chain and VME Chain	22
3.1.1 Hardware	22
3.1.2 Software	23
3.2 MRD Chain	25
3.2.1 Hardware	25
3.2.2 Software	26
3.3 Future improvement	28
4 Data Analysis procedures	31
4.1 Data selection	31
4.2 Individual pulse analysis	31
4.3 Signal and noise discrimination	35
4.4 Data size reduction	37
5 Data analysis results	41
5.1 Cosmic muons	41
5.2 Centre of interaction	42
5.3 Beam events	45
5.4 Muon decay	45
5.5 Neutron yield	48
5.6 First MRD data	50
6 Conclusions	53

A	Booster Neutrino Beam	55
A.1	The target	55
A.2	The Horn	56
A.3	Monitoring	57
B	Monte Carlo simulation	59
C	Fit results	63
C.1	Event	63
C.2	Noise	65
C.3	All data	69

Chapter 1

Introduction

The Standard Model (SM) is a gauge theory that describes the strong, electromagnetic, and weak interactions of elementary particles in the framework of quantum field theory. The theory is based on the local symmetry group

$$\mathrm{SU}(3)_C \otimes \mathrm{SU}(2)_L \otimes \mathrm{U}(1)_Y \quad (1.1)$$

where C , L and Y denote color, left-handed chirality and weak hypercharge, respectively. The gauge group uniquely determines the interactions and the number of vector gauge bosons that correspond to the generators of the group. They are eight massless gluons that mediate strong interactions, corresponding to the eight generators of $\mathrm{SU}(3)_C$, and four gauge bosons, of which three are massive (W^\pm and Z) and one is massless, corresponding to the three generators of $\mathrm{SU}(2)_L$ and one generator of $\mathrm{U}(1)_Y$, responsible for electroweak interactions. The symmetry group of the SM fixes the interactions, i.e. the number and properties of the vector gauge bosons, with only three independent unknown parameters: the three coupling constants of the $\mathrm{SU}(3)_C$, $\mathrm{SU}(2)_L$, and $\mathrm{U}(1)_Y$ groups, all of which must be determined from experiments. On the contrary, the number and properties of scalar bosons and fermions are left unconstrained, except for the fact that they must transform according to the representations of the symmetry group, while the fermion representations must lead to the cancellation of quantum anomalies. The known elementary fermions are divided in two categories, quarks and leptons, according to the scheme:

Generation	1st	2nd	3rd
Quark	u d	c s	t b
Leptons	e ν_e	μ ν_μ	τ ν_τ

and their respective antiparticles. They are distinguished by the fact that quarks participate in all the interactions whereas leptons participate only in the electroweak interactions [7].

In the SM, electroweak interactions can be studied separately from strong interactions, because the symmetry under the color group is unbroken and there is no mixing between the $\mathrm{SU}(3)_C$ and the $\mathrm{SU}(2)_L \otimes \mathrm{U}(1)_Y$ sectors. On the other hand, the Glashow, Salam, and Weinberg theory well explains the group mixing between electromagnetic and weak interactions caused by a symmetry breaking process. This model and the discovery of the predicted W and Z bosons, in addition to the gluon, the top, and charm quarks, made the fortune of the Standard Model. Their predicted properties were experimentally confirmed with good precision and the recent discovery of the Higgs Boson [5] [6] is the last crowning achievement of SM.

Despite being the most successful theory of particle physics to date, the SM is actually limited in its approximation to reality, in that some clear evidences cannot be explained. The most outstanding breakthrough is the neutrino oscillations, which was awarded the Nobel Prize in Physics in 2015 and has proved that the neutrinos are not all massless, as it is assumed by theory. Mass terms for the neutrinos can be included in the SM, with the implications of theoretical problems. Likewise, the SM is unable to provide an explanation of the observed asymmetry between matter and anti-matter. It was noted by Sakharov that a solution to this puzzle would require some form of C and CP violation in the early Universe, along with Baryon number violation and out-of-equilibrium interactions. These facts suggest that the Standard Model is not a complete theory and additional physics Beyond the Standard Model (BSM) is required.

The study of neutrinos is for sure one of the most promising probe to BSM physics and is of vital importance to the future development of particle physics, in particular through precision measurement of their interactions. A deep understanding of neutrino interactions, and neutrino-nucleon interactions in particular, could lead to a great impact on long-baseline experiments, proton decay search, and supernova detection.

1.1 Neutrino interactions

Neutrinos are colourless and chargless particles, thus sensitive only to weak interactions. Because of their nature, these leptons have small cross-sections and are difficult to measure. All the interactions are described by the electroweak part of the SM, based on the symmetry group $SU(2)_L \otimes U(1)_Y$, and are governed by the lagrangian $\mathcal{L} = \mathcal{L}^{(CC)} + \mathcal{L}^{(NC)}$. In fact, neutrinos are mediated by the W^\pm for charged-current (CC) interactions and by the Z boson for neutral-current (NC) ones, whose respective lagrangians are:

$$\mathcal{L}^{(CC)} = -\frac{g}{2\sqrt{2}}(j_{W,L}^\mu W_\mu + \text{h.c}) \quad (1.2)$$

$$\mathcal{L}^{(NC)} = -\frac{g}{2\cos\vartheta_W} j_{Z,\nu}^\mu Z_\mu, \quad (1.3)$$

where the two currents are given by

$$j_{W,L}^\mu = 2 \sum_{\alpha=e,\mu,\tau} \overline{\nu_{\alpha L}} \gamma^\mu l_{\alpha L} \quad (1.4)$$

$$j_{Z,\nu}^\mu = \sum_{\alpha=e,\mu,\tau} \overline{\nu_{\alpha L}} \gamma^\mu \nu_{\alpha L}, \quad (1.5)$$

and $\vartheta_W = 28.7^\circ$ is the Weinberg angle.

The easiest interaction that can be studied is the neutrino-electron elastic scattering

$$\nu_\alpha + e^- \rightarrow \nu_\alpha + e^-, \quad (1.6)$$

and its antineutrino counterpart¹. For the electronic neutrino, both CC and NC interactions are allowed, while for $\alpha = \mu, \tau$ the charged-current interactions are forbidden. The respective Feynman diagrams are shown in Fig. 1.1 and ???. For low neutrino energies, where the effects of the W and Z propagators can be neglected, the above processes are described by the effective charged-current and neutral-current lagrangians

$$\mathcal{L}_{\text{eff}}(\nu_e e^- \rightarrow \nu_e e^-) = -\frac{G_F}{\sqrt{2}} [\bar{\nu}_e \gamma^\mu (1 - \gamma^5) \nu_e] [\bar{e} \gamma_\mu ((1 + g_V^l) - (1 + g_A^l) \gamma^5) e] \quad (1.7)$$

$$\mathcal{L}_{\text{eff}}(\nu_\alpha e^- \rightarrow \nu_\alpha e^-) = -\frac{G_F}{\sqrt{2}} [\bar{\nu}_\alpha \gamma^\mu (1 - \gamma^5) \nu_\alpha] [\bar{e} \gamma_\mu (g_V^l - g_A^l) \gamma^5 e] \quad (\alpha = \mu, \tau). \quad (1.8)$$

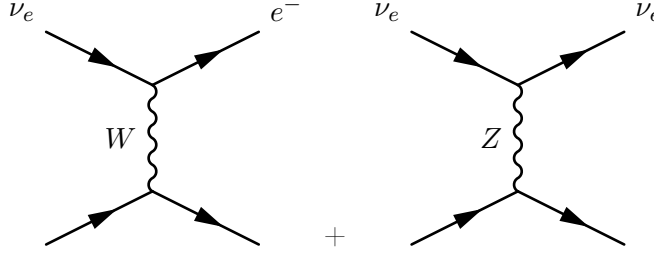


Figure 1.1: Tree-level Feynman diagrams for the process $\nu_e + e^- \rightarrow \nu_e + e^-$. The respective anti-neutrino CC interaction is a s -channel process, instead.

$\nu_{\mu,\tau}$

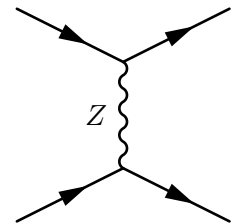


Figure 1.2: Tree-level Feynman diagrams for the process $\nu_{\mu,\tau} + e^- \rightarrow \nu_{\mu,\tau} + e^-$. Only the NC process is permitted, which is also valid in the anti-neutrino case.

The differential cross-section with respect to the momentum transfer Q^2

$$\frac{d\sigma}{dQ^2} = \frac{G_F^2}{\pi} \left[g_1^2 + g_2^2 \left(1 - \frac{Q^2}{2p_\nu \cdot p_e} \right)^2 - g_1 g_2 m_e^2 \frac{Q^2}{2(p_\nu \cdot p_e)^2} \right]. \quad (1.9)$$

The quantities g_1 and g_2 depend on the flavour of the neutrino and related to the vector and axial couplings, g_V and g_A . They are:

$$g_1^{\nu_e} = \frac{1}{2} + \sin^2 \vartheta_W \quad , \quad g_2^{\nu_e} = \sin^2 \vartheta_W \quad (1.10)$$

$$g_1^{\nu_{\mu,\tau}} = -\frac{1}{2} + \sin^2 \vartheta_W \quad , \quad g_2^{\nu_{\mu,\tau}} = \sin^2 \vartheta_W. \quad (1.11)$$

The differential cross-section as a function of the electron scattering angle in the laboratory frame is

$$\frac{d\sigma}{d\cos\theta} = \sigma_0 \frac{4E_\nu^2(m_e + E_\nu)^2 \cos\theta}{[(m_e + E_\nu)^2 - E_\nu^2 \cos^2\theta]^2} \left[g_1^2 + g_2^2 \left(1 - \frac{2m_e E_\nu \cos^2\theta}{(m_e + E_\nu)^2 - E_\nu^2 \cos^2\theta} \right)^2 - g_1 g_2 \frac{2m_e^2 \cos^2\theta}{(m_e + E_\nu)^2 - E_\nu^2 \cos^2\theta} \right], \quad (1.12)$$

where

$$\sigma_0 = \frac{2G_F^2 m_e^2}{\pi}. \quad (1.13)$$

For what concern the experiments, neutrino interactions with nucleons are easier to study thanks to the much larger cross-section and a more diverse range of processes, despite being less straightforward to deal with theoretically. In general, these processes can be categorised according to the momentum transfer. At small Q^2 , elastic interactions dominate and may be brought about by both charged and neutral currents. When this occurs via neutral currents, all flavour of neutrinos and anti-neutrinos can scatter off both neutrons and protons in what is referred to as “NC elastic” scattering. The process is:

$$\nu_l + N \rightarrow \nu_l + N, \bar{\nu}_l + N \rightarrow \bar{\nu}_l + N, \quad (1.14)$$

¹In terms of Feynman diagrams, the t -channel diagram is replaced by the s -channel diagram.

Once neutrinos acquire sufficient energy they can also undergo the analogous charged current interactions, called “quasi-elastic”, due to the fact that the recoiling nucleon changes its charge and mass transfer occurs. The processes are

$$\nu_l + n \rightarrow p + l^- \quad (1.15)$$

$$\bar{\nu}_l + p \rightarrow n + l^+, \quad (1.16)$$

with $l = e, \mu, \tau$. For the muonic neutrino with energy below one GeV, the CCQE is the dominant interaction, even though the cross-section plateaus at higher energies, as the available Q^2 increases: it becomes increasingly unlikely for the nucleon to remain intact.

The physics behind the CC quasi-elastic processes is more complicated. The differential cross-section for the scattering in the laboratory frame is given by

$$\frac{d\sigma_{CC}}{dQ^2} = \frac{G_F^2 |V_{ud}|^2 m_N^4}{8\pi (p_\nu \cdot p_N)^2} \left[A(Q^2) \pm B(Q^2) \frac{s-u}{m_N^2} + C(Q^2) \frac{(s-u)^2}{m_N^4} \right], \quad (1.17)$$

where the plus sign refers to the $N = n$ interactions, while the minus sign to $N = p$.

$$\frac{d\sigma_{CC}}{d\cos\theta} = -\frac{G_F^2 |V_{ud}|^2 m_N^2}{4\pi} \frac{p_l}{E_\nu} \left[A(Q^2) \pm B(Q^2) \frac{s-u}{m_N^2} + C(Q^2) \frac{(s-u)^2}{m_N^4} \right], \quad (1.18)$$

The functions $A(Q^2)$, $B(Q^2)$, and $C(Q^2)$ depends on the nucleon form-factors in the following way:

$$A = \frac{m_l^2 + Q^2}{m_N^2} \left\{ \left(1 + \frac{Q^2}{4m_N^2} \right) G_A^2 - \left(1 - \frac{Q^2}{4m_N^2} \right) \left(F_1^2 - \frac{Q^2}{4m_N^2} F_2^2 \right) + \frac{Q^2}{m_N^2} F_1 F_2 - \frac{m_l^2}{4m_N^2} \left[(F_1 + F_2)^2 + (G_A + 2G_P)^2 - \frac{1}{4} \left(1 + \frac{Q^2}{4m_N^2} \right) G_P^2 \right] \right\} \quad (1.19)$$

$$B = \frac{Q^2}{m_N^2} G_A (F_1 + F_2) \quad (1.20)$$

$$C = \frac{1}{4} (G_A^2 + F_1^2 + \frac{Q^2}{4m_N^2} F_2^2). \quad (1.21)$$

The form factors $F_1(Q^2)$, $F_2(Q^2)$, $G_A(Q^2)$, and $G_P(Q^2)$ are called, respectively, *Dirac*, *Pauli*, *axial*, and *pseudoscalar* weak charged-current form factors of the nucleon. These funtions of Q^2 describe the spatial distributions of electric charge and current inside the nucleon and thus are intimately related to its internal structure.

CCQE interactions are particularly important to neutrino physics for mainly two reasons:

- measurements of the differential cross-section in Eq. 1.17 give information on the nucleon form-factors, which are difficult to measure;
- their nature as two-body interactions enable the kinematics to be completely reconstructed, and hence the initial neutrino energy determined which is critical for measuring the oscillation parameters.

In fact, if the target nucleon is at rest, at least compared to the neutrino energy, then this can be calculated as:

$$E_\nu = \frac{m_n E_l + \frac{1}{2} (m_p^2 - m_n^2 - m_l^2)}{m_n - E_l + p_l \cos\theta_l}, \quad (1.22)$$

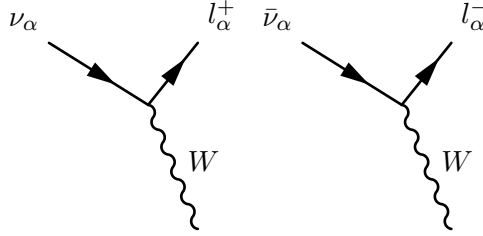


Figure 1.4: Production vertices for neutrinos in CC.

where the measurement of the momentum, p_l and the angle with respect to the neutrino, θ_l , of the outgoing charged lepton are only required.

Similar calculations can be made for the NCQE scatterings. The cross-sections have the same form as the CC cross-sections in Eq. 1.17 and 1.18, without the mixing term $|V_{ud}|^2$ and with the proper nucleon form factors. Since the values of the electromagnetic form factors, F_1 and F_2 , are reasonably well known and the part in Eq. 1.19 containing G_P can be often neglected, thanks to the different mass magnitudes of leptons and nucleons, the axial form factor, G_A , can be determined through measurements of the charged-current quasielastic scattering processes. On the contrary, measurements of the neutral-current elastic scattering cross-section give information on the *strange* form factors of the nucleon, whose main contribute comes from the strange quark.

The low Q^2 region also presents an inelastic scattering contribution mostly affected by resonance production, where the nucleon is excited into a baryonic resonance before decaying. At high Q^2 , inelastic scattering is dominated by deep inelastic scattering (DIS), because the neutrino can scatter directly off a constituent quark, fragmenting the original nucleon. In between these extreme scenarios, an additional contribution comes from interactions where the hadronic system is neither completely fragmented nor forms a recognisable resonance. These interactions are referred to as “shallow inelastic scattering”, and there is no clear model for dealing with them.

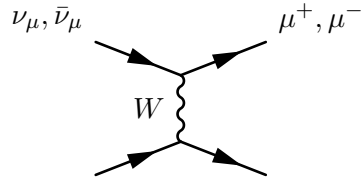


Figure 1.3: CC interaction of a neutrino with a nucleon, producing the corresponding lepton. This interaction is called Quasi Elastic.

1.2 Neutrino detection

Being electrically neutral and uncoloured particles, neutrinos can only interact through weak interactions. For this reason, coupled with the small cross-sections typical of the weak force, the study of neutrino results in a challenging task. Direct observation is unfeasible, thus detection must rely on weak interactions with matter, where their SU(2) charged counterparts are either produced or scattered, by CC or NC interactions respectively. The physics is mediated by the lagrangians in Eq. 1.2 and 1.3.

Large active volumes have to be employed, such that a significant number of neutrino can be considered and interaction probability is thus increased. These apparatus are often built underground to shield the detector from cosmic rays and other background radiation. Apart from providing matter to interact with, at the same time these volumes must be capable of detecting the scattered charged leptons. Many are the materials or substances that can be used, like chlorine, gallium, solid or liquid scintillators.

One of the most promising techniques is to combine liquid argon with time projection chambers. As with most other liquefied noble gases, argon has a high scintillation light yield (ca 51 photons/keV[arXiv:1004.0373]), is transparent to its own scintillation light, and is relatively easy to purify. Compared to xenon, argon is also cheaper and has a

distinct scintillation time profile which allows the separation of electronic recoils from nuclear recoils.

A more dated and better-known technology is the *water Cherenkov* method, where the detector is used to record the Cherenkov light produced when the particles pass through tanks full of purified water.

1.2.1 Water cherenkov

The speed of light in vacuum is a universal constant, c , and it is a physical limit of the propagation of information, as stated by the special theory of Relativity. However, when in a medium, light may travel at speed significantly less than c . This reduction of speed depends on the relative permittivity, ε , of the material in which light is propagating. Because of the non-zero real part of the dielectric constant, the electromagnetic (EM) field is modified and the phase velocity of light changes into

$$v_P = \frac{c}{\sqrt{\varepsilon(\lambda)}} = \frac{c}{n(\lambda)}, \quad (1.23)$$

where $n(\lambda) > 1$ is the *refractive index* of the medium and depends on the wavelength (energy) of the wave.

A charged particles moving at a constant velocity in a dielectric medium disrupts the local electromagnetic field, by deforming its molecules and temporarily polarising the material. The dipoles are restored almost instantaneously and thus become impulsive sources of EM waves. If the velocity of the passing particle, $v = \beta c$, is less than the speed of the light in the medium as expressed in Eq. 1.23, i.e. $\beta < 1/n$, then the total energy flux of the excited field is zero and EM waves are not irradiated. On the contrary, if $\beta > 1/n$, the perturbation left by the passage of the particle is such that the energy is released coherently. The result is that the field is different from zero in a cone coaxial with respect to the direction of the charged particle, whose direction is opposite to the particle motion. As far as the photons are concerned, these are emitted coherently to a fixed angle with respect to the particle motion. With the help of Fig. 1.5, it is easy to find that:

$$\sin \alpha = \frac{1}{\beta n} \quad (1.24)$$

$$\cos \theta = \frac{1}{\beta n}. \quad (1.25)$$

where α is the apex angle of the cone and θ is the photon angle with respect to the particle direction. For an ultra-relativistic particle, for which $\beta \sim 1$, there is a maximum angle of emission, given by:

$$\cos \theta_{MAX} = \frac{1}{n}. \quad (1.26)$$

The phenomenon is called *Cherenkov effect*, and it occurs everytime a charged particle passes through a dielectric medium at a speed:

$$\beta > \frac{1}{n}. \quad (1.27)$$

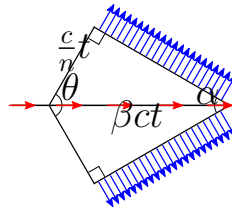


Figure 1.5: The geometry of the Cherenkov radiation. The blue arrows represent the emitted photons, the red ones the track of the charged particle.

According to the theory of electromagnetic waves, a charged particle moving uniformly does not irradiate and this proves that the Cherenkov radiation is not related with Bremsstrahlung.

This condition can be expressed in terms of the particle energy, given that $E^2 = p^2 + m^2$ and $\beta = p/E$. The threshold becomes:

$$\frac{E}{m} > \frac{1}{\sqrt{1 - 1/n^2}}, \quad (1.28)$$

with m the mass of the charged particle.

The radiation is emitted in the visible and near visible regions of the EM spectrum, for which $n > 1$. A real medium is always dispersive and radiation is restricted to those frequencies bands for which $n(\nu) > \frac{1}{\beta}$. In the x-ray region, for instance, $n(\nu)$ is always less than one and radiation is forbidden at this energies, because Eq. 1.27 cannot be satisfied.

Truly, coherent emission of light needs two more conditions to be fulfilled:

- the length of the track of the particle in the medium should be large compared with the wavelength, λ , of the radiation in question, otherwise diffraction effects will become dominant;
- the velocity of the particle must be constant during its passage through the medium, or, to be more specific, the differences in the times for particle to traverse successive λ distances should be small compared with the period $\frac{\lambda}{c}$ of the emitted light.

The number of photons emitted by a charged particle of charge Ze per unit path length and per unit energy interval, or equivalently to λ , of the photons is equal to:

$$\frac{d^2N}{dx d\lambda} = \frac{2\pi\alpha Z^2}{\lambda^2} \left(1 - \frac{1}{\beta^2 n^2(\lambda)}\right). \quad (1.29)$$

This means that the greater part of Cherenkov photons are emitted in the ultraviolet range, because of the proportionality to $1/\lambda^2$.

Cherenkov detectors take advantage of this effect, detecting the light produced by charge particles. A large volume of transparent material, such as water, ice, or liquid scintillator, can be surrounded by lightsensitive detectors in order to capture the Cherenkov radiation. This technique is largely used in neutrino detection, since they cannot be detected directly: the charged lepton, yeilded in CC or NC interactions, is observed. From the light collected, it is possible to reconstruct information on the interaction, such as the velocity of the charged particle, which is somehow related to the energy of the incident neutrino, or the position of the interaction vertex. If the charged lepton drop under the Cherenkov threshold, the light is emitted in the shape of a ring, which further data can be inferred from. Not every neutrino energy allows the production of a charged lepton³, but only MeV-scale neutrinos can be observed in a Cherenkov detector.

1.2.2 Gadolinium neutron capture

to be improved.

Current multi-kiloton scale water Cherenkov detectors, like Super-Kamiokande (SK), have provided many clues in the experimental understanding of the neutrino, be it originated in solar, atmospheric, or accelerator reactions. However, in spite of the large lifetime of the experiment, some analyses are still limited by statistical uncertainty, and would benefit from increasing exposure. Other analyses suffer from background contamination, as in

²For this calculation, the convention $c = 1$ is adopted.

³For instance, the CCQE process $\bar{\nu}_e + p \rightarrow n + e^+$ has a energy threshold of 1.81 MeV and the interaction $\nu_\mu + n \rightarrow p + \mu^-$ has the threshold of 110.16 MeV, because of the muon mass.

the case of the supernova relic neutrinos (SRN) search, and would benefit more from the development of new background suppression techniques. This hindrance can be overcome by studying the yield of neutrons in neutrino interactions, such as the *inverse beta decay* (the antineutrino CCQE scattering). It would allow a handle on antineutrinos rate, and possibly a method of background reduction for other studies.

Since neutrons are chargeless, they cannot interact with matter by means of the Coulomb force, which dominates the energy loss mechanisms for charged particles, described by the Bethe formula. Neutrons can interact with nuclei in various way, depending on the energy:

- elastic and inelastic scattering;
- transmutation;
- neutron activation;
- spallation reaction;
- neutron-induced fission;

As a result of the interaction, the neutron may either be absorbed, or change its energy and direction significantly. In this way the average energy of a neutron beam can be completely or partly reduced up to thermal energies, close to 0.025 eV. In this range of energy, the neutron presents a different and often much larger effective neutron absorption cross-section for a given nuclide, compared to, for instance, fast neutrons, hence *thermalisation* can result in a *neutron activation* process. This occurs when atomic nuclei capture free thermal neutrons, creating heavier nuclei, often in an excited state. The excited nucleus decays almost instantaneously emitting usually gamma rays.

The neutron energy distribution is adopted to the Maxwellian distribution known for thermal motion. The time required by the thermalisation of neutrons follows an exponential, and the time constant is largely studied, [ref needed], amongst all the thermalisation in water. It was found that neutron thermalisation in water has a time constant of $5\mu\text{s}$ [fujino, sumita, shiba]. Neutrons can be captured by either the hydrogen or the oxygen. Free neutron will capture on a hydrogen nucleus, releasing a 2.2 MeV gamma. In SK, for instance, this gamma results in about seven photo-electrons, and thus only detectable with $\simeq 20\%$ efficiency.

Gadolinium-157 has the highest thermal neutron capture cross-section among any stable nuclides: 259,000 barns. Dissolving gadolinium compounds in water could considerably increase the neutron capture probability. The neutron in water thermalises quickly and can thus be captured by a Gd nucleus with a probability of 90 %. Upon capturing a neutron the Gd emits 3-4 gamma rays having a total energy of about 8 MeV. The time and spatial correlation of the positron and neutron capture events (20 μs and 4 cm) can significantly reduce the backgrounds, and hence enhance the neutrino signal events. Even moderately energetic neutrons ranging from tens to hundreds of MeV will quickly lose energy by collisions with free protons and oxygen nuclei in water. Once thermalised, the neutrons undergo radiative capture, combining with a nearby nucleus to produce a more tightly bound final state, with excess energy released in a gamma-ray () cascade. Gd-doped water enhances the capture cross-section compared to pure water (49,000 barns compared with 0.3 barns on a free proton) and, since the cascade happens at higher energies (8 MeV vs 2.2 MeV), it produces enough optical light to be reliably detected in a large target volume.

1.3 Neutrino Production

Numerous are the neutrino sources at the reach of neutrino experiments. Neutrinos are produced in CC interactions, which can happen in nuclear reaction, as for *solar* or *reactor* neutrinos, or in cosmic rays impacts with the Earth's atmosphere, conveying energetic *atmospheric* neutrinos.

Artificial neutrinos are also yielded in high-energy proton accelerators. Accelerator neutrino beams are fundamental instrumental discovery tools in particle physics, in that more control less variables are involved. Neutrino beams are derived from the decays of charged π and K mesons, which in turn are created from proton beams striking thick nuclear targets. The precise selection and manipulation of the π/K beam control the energy spectrum and type of neutrino beam.

The π^\pm mesons have a mass of 139.6 MeV and a mean lifetime of 2.6×10^{-8} s. The primary decay mode of a pion, with a branching fraction of 99.9877 %, is a leptonic decay into a muon and a muon neutrino:

$$\begin{aligned} \pi^+ &\rightarrow \mu^+ + \nu_\mu & (1.30) \\ \pi^- &\rightarrow \mu^- + \bar{\nu}_\mu & (1.31) \end{aligned}$$

The second most common decay mode of a pion, is the leptonic decay into an electron and the corresponding neutrino, $\pi^\pm \rightarrow \nu_e + e$. In spite of the considerable differences in the space momentum, this process is suppressed with respect to the muonic one. This effect is called *helicity suppression* and is due to the great mass of the muon ($m_\mu = 105.658$ MeV) compared to the electron's ($m_e = 0.510$ MeV); this results in a stronger helicity-chirality correspondence for the electron rather than for the muon. Given that the π mesons are spinless, neutrinos are left-handed, and antineutrinos are right-handed, the muonic channel is preferred because of spin and linear momentum preservation. The suppression of the electronic decay mode with respect to the muonic one is given approximately within radiative corrections by the ratio:

$$R_\pi = \left(\frac{m_e}{m_\mu} \right)^2 \left(\frac{m_\pi^2 - m_e^2}{m_\pi^2 - m_\mu^2} \right) = 1.283 \times 10^{-4} \quad (1.32)$$

The measured branching ratio of the electronic decay is indeed $(1.23 \pm 0.02) \times 10^{-4}$.

As far as the charged K meson is concerned, it mainly decays in a muon and its corresppective neutrino, with a branching ratio of 63.55 %:

$$\begin{aligned} K^+ &\rightarrow \mu^+ + \nu_\mu & (1.33) \\ K^- &\rightarrow \mu^- + \bar{\nu}_\mu & (1.34) \end{aligned}$$

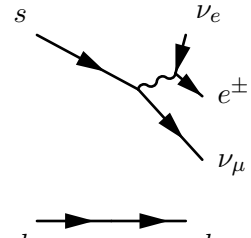
The second most frequent decay (20.66 %) is the decay into two pions, $K^\pm \rightarrow \pi^0 + \pi^\pm$. Other decays have a branching ratio of 5 % or less and are listed in table Tab. 1.1. On the contrary, the decays of the neutral kaon produce neutrino in few cases. Because of the oscillation phenomenon given by the mixing between K^0 and \bar{K}^0 , the neutral kaon has two manifestations, the short kaon K_S and the long kaon K_L , named after their lifetimes. While the K -short decays only in two pions ($2\pi^0$ or $\pi^+ + \pi^-$), the K -long has a wider variety of final state combination, all of them involving three particles. Among these, neutrinos are produced in the processes:

$\mu^\pm + \nu_\mu^{(-)}$	65.55 ± 0.11
$\pi^\pm + \pi^0$	20.66 ± 0.08
$\pi^+ + \pi^\pm + \pi^-$	5.59 ± 0.04
$\pi^0 + e^\pm + \nu_e^{(-)}$	5.07 ± 0.04
$\pi^0 + \mu^\pm + \nu_\mu^{(-)}$	3.35 ± 0.03
$\pi^\pm + \pi^0 + \pi^0$	1.76 ± 0.02

Table 1.1: Decay mode for a charged kaon, K^\pm , sorted by branching ration (in percent).

$$K_L^0 \rightarrow \pi^\pm + \mu^\mp + \nu_\mu^{(-)} \quad (1.35)$$

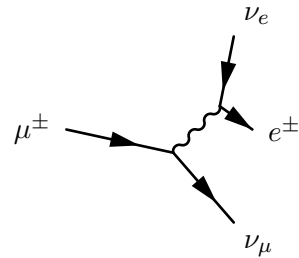
$$K_L^0 \rightarrow \pi^\pm + e^\mp + \nu_e^{(-)} \quad (1.36)$$



Neutrinos are also produced by the decay of muons. Muons are unstable elementary particles and decay via the weak interaction. The dominant decay mode, called *Michel decay*, is also the simplest possible: because lepton numbers must be conserved, one of the product neutrinos of muon decay must be a muonic neutrino and the other an electronic antineutrino, along with an electron, because of the charge preservation. Vice versa, an antimuon decay produces the corresponding antiparticles. These two decays are:

$$\mu^- \rightarrow e^- + \bar{\nu}_e + \nu_\mu \quad (1.37)$$

$$\mu^+ \rightarrow e^+ + \nu_e + \bar{\nu}_\mu \quad (1.38)$$



The neutrino source provided by the muon decay, is more of a nuisance background, because of the long lifetime, which give rise to electronic component in neutrino spectrum. Usually a beam absorber is located at the end of the decay region of an accelerator line, to stop the hadronic and muonic component of the beam, and only an almost pure neutrino beam pointing towards the detector remains.

Chapter 2

The ANNIE Experiment

As more neutrino data become available, lack of knowledge of the fine details of neutrino-nucleus interactions begins to limit the physics reach of future experiments. For instance, final-state neutron abundance from pure neutrino interactions is currently poorly known and difficult to measure. Data on neutron yield in relation to energy and direction of final-state muons can be used to better constrain nuclear models of neutrino interaction physics and are an essential input for Monte Carlo models, used for calculating detection efficiencies, expected background rates, accurate limits, and confidence levels. The count of neutrons can also be used to reject contamination by atmospheric neutrino interactions in proton decay experiments and in a sample of diffuse supernova background neutrinos and may also help to statistically address wrong-sign contamination in oscillation analyses. In addition to helping understand fundamental neutrino-interaction physics, tagging events by the presence and number of final-state neutrons can provide physics analyses with a better handle for signal/background separation and even allow for discrimination between different types of neutrino interactions.



Figure 2.1: Logo of the ANNIE experiment.

A study of final-state neutron abundance can be accomplished by the Accelerator Neutrino Neutron Interaction Experiment (ANNIE), which will provide a complementary measurement of neutron yields in neutrino-nucleon interactions [4]. The ANNIE experiment is a prototype neutrino detector currently taking data at the Fermi National Accelerator Laboratory (FNAL, Fermilab), in Chicago, USA. It consists of a small water Cherenkov detector, placed at the former location of the SciBooNE experiment [13] and deployed on the intense Booster

Neutrino Beam (BNB). An upstream forward Veto and a downstream Muon Range Detector (MRD) are also installed in the hall. The experiment aims to be a test bed for many new technologies, such as the gadolinium-doped water and the use of early prototype Large Area Picosecond Photodetectors (LAPPDs). The ANNIE experiment will be an innovative application of these devices demonstrating their feasibility for Water Cherenkov neutrino detectors.

The experiment is planned to proceed in two stages, spread over five years:

Phase I a partially-instrumented test-beam run using only Photomultipliers (PMTs) for the purpose of measuring critical neutron backgrounds to the experiment;

Phase II a longer run with a more fully-instrumented detector where incremental research and development for the LAPPDs and accompanying fast electronics will be fulfilled, as long as the expansion of the photodetector coverage (both LAPPDs and PMTs)

required.

Year 1 will focus on the R&D, particularly on the development of the Data Acquisition system, along with the testing in water of the first model of LAPPD. Installation of the first LAPPDs and a significant fraction of the additional PMTs, as well as the calibration system, will take place in *Year 2*. Data-taking would commence in *Year 3* and continue through *Year 5*, with the physics reach of the detector improving as the fraction of LAPPDs increases over time. Publication of derived results would occur by the end of *Year 5* [3]

This thesis takes place at the beginning of *Year 1*, where the experimental setup of Phase I is tested and R&D is undertaken.

2.1 Physics of the experiment

Aside from the opportunity to test new technologies, ANNIE will also collect valuable data by observing interactions between neutrinos and nucleons. Little is known about the Physics behind these processes, except from that it is strictly influenced by the complex interplay of multiple particles; current models are limited in their approximation to reality.

The principal process at first order, that the experiment is sensitive to, is the charged current quasi-elastic scattering (CCQE, see section 1.1) of the muon neutrino on a bound nucleon; the interaction yields a proton (neutron) from the neutrino (anti-neutrino) interaction. CC scattering without pions in the final state is a critical component for neutrino oscillation experiments. However, CCQE cross section precise measurements have been unavailable, for several reasons:

- neutrino beams typically span a wide energy range thereby preventing an incoming energy constraint on the reaction;
- the neutrino flux itself is often poorly known, hampering normalization of reaction rates;
- background processes are frequently significant and difficult or impossible to separate from the CCQE signal;
- the target nucleon is not free but bound in a nucleus and correlations between nucleons are important.

The theory describing these interactions is under development and is often weakly constrained by the available data [10]. Higher-order processes and multi-scale nuclear physics, including secondary (p,n) scattering of struck nucleons within the nucleus, charge exchange reactions of energetic hadrons in the nucleus (e.g., $\pi^- p \rightarrow n \pi^0$), and Meson Exchange Currents (MEC) [15], where the neutrino interacts with a correlated pair of nucleons, all modify theoretical expectations.

The MiniBooNE experiment [8] has been able to measure the double differential cross section for the CCQE interactions of muon neutrinos [1] and antineutrinos [2], on a carbon-12 target. Employing a modified Real Fermi Gas model [14], the axial mass, M_A , of the dipole axial form factor was measured to be greater than older measures. Within the model prediction, a larger value for M_A implies a larger cross section, because the CCQE cross section increases approximately linearly with the axial mass. This may indicate a significant contribution from neglected mechanisms for CCQE-like scattering from a nucleus such as multi-nucleon processes. For instance, the double differential cross section for CCQE interactions is better described by models including *two-body currents*, where low-energy neutrinos scatter off correlated pairs of nucleons. Several models [11] have been developed on two body currents, but there is no consensus on many details how these events look like.

A model-independent consequence of two-body currents is higher multiplicity of final state neutrons, therefore a key handle in understanding neutrino-nucleus interaction would be the number and type of nucleons ejected from the interaction. As established previously, detection of neutrons from nuclear interactions would have a transformative impact on a wide variety of neutrino physics measurements. Nevertheless there are major limitations on the effective execution of neutron tagging techniques, for both sides of Physics:

theoretically large theoretical uncertainties on the nuclear mechanisms that produce neutrons in GeV-scale neutrino interactions are not still clear;

experimentally the neutron yield hasn't been satisfactorily measured yet.

ANNIE can study neutron yields from mostly-pure neutrino interactions separately, by measuring neutron yields in relation to the energy and direction of final-state muons with respect to the original neutrino. The search for a delayed signal from neutron capture on Gadolinium (Gd) salts dissolved in water is a promising technique for detecting final state neutrons [9]. The probability of producing zero, one, or multiple neutrons from a neutrino interaction must be characterised, as a function of both interaction type and momentum transfer. This evaluation is expected to require on the order of ten thousands neutrino interactions, considering the efficiencies and acceptances of the experimental setup, which should be around the 10 % of the interactions in the detector. This corresponds to one year of data with the detector fully instrumented. With additional statistics (additional two years of data) and improved detector performance, the more demanding goal of studying neutron yields for specific event classes can be met.

A precise evaluation of the neutron production requires a high efficiency measure and event reconstruction. The experiment relies on the detection of Cherenkov light and photocoverage should be wisely optimised. It is possible to estimate the number of photons produced by the Cherenkov effect, starting from Eq. 1.29. Its integration with respect to space and wavelength, λ , returns:

$$N = L2\pi\alpha Z^2 \int_{\lambda_2}^{\lambda_1} \frac{1}{\lambda^2} \left(1 - \frac{1}{\beta^2 n^2(\lambda)}\right) d\lambda. \quad (2.1)$$

If the λ dependence of the refractive index is negligible, the formula for an ultra-relativistic charged lepton becomes:

$$N = 2L\pi\alpha \sin^2 \theta_C \left(\frac{1}{\lambda_1} - \frac{1}{\lambda_2}\right). \quad (2.2)$$

Inasmuch as the quantum efficiency (QE) of most PMTs peaks near 20 % in the spectrum that spans from 300 nm to 500 nm, it is possible to roughly calculate the number of gammas detected to the passage of a muon. Saying $\lambda_1 = 300$ nm, $\lambda_2 = 500$ nm, $\theta_C = 41^\circ$, and $L = 4$ m, with a detection efficiency of 20 %, the detectable photons are:

$$N = 21,050.4. \quad (2.3)$$

Geometry relections effects can significantly modify this result.

The sizes of the water tank are reduced compared to other detectors. For this reason, the difference in transit time between two photons arriving at the same photosensor from two different forward-pointing tracks is just a few nanoseconds. Such deferments are not of nuisance, as far as the data analysis is concerned. After pulse phenomenon of the PMTs and light reflection are more disturbing, but the knowledge of their characteristic time helps the discrimination. A late pulse takes up to three times the transit time of the photoelectron to occur (generally between 30 ns and 150 ns), while the actual after pulse can happen

much later (from 100 ns to 15 μ s) than the pulse¹. Light reflection effects are constrained to the geometry of the tank. The longest path possible is the diagonal of the cylinder, which is about five metres. The maximum transit time for direct light to travel back and forth in the ANNIE tank is near thirty nanoseconds.

2.2 Neutrino beam

ANNIE is run on axis from the *Booster Neutrino Beam* (BNB), which deploys 8.89 GeV protons accelerated from the Fermilab booster operating at 15 Hz. The primary beam from the *Linac* uses protons accelerated to 8 GeV kinetic energy by the Fermilab booster. Selected batches containing approximately 5×10^{12} protons are extracted and bent toward a beryllium target via dipole magnets. Each spill is composed of 81 bunches of protons, approximately 6 ns wide each and 19 ns apart, for a total spill duration of 1.6 μ s. As far as the detector is concerned, the neutrino beam is seen to arrive with a spill frequency of 15 Hz, divided in pulse train, around 1 s apart each other [12].

Beam proton trajectories and positions are monitored on a pulse-by-pulse basis. Upstream of the target, the primary proton beam is monitored on a pulse-by-pulse basis using four systems: two toroids measuring its intensity (protons-per-pulse), beam position monitors (BPM) and a multi-wire chamber determining the beam width and position, and a resistive wall monitor (RWM) measuring both the time and intensity of the beam spills. A logic signal is also generated by the last device for every intensity peak. It is employed to trigger the experiment in correspondence of each spill. The BNB is dealt in detail in the appendix A.

Hadronic interactions of the protons with the target material produce a beam of secondary mesons, mostly pions and kaons. A magnetic focusing horn surrounds a beryllium target, bending and selecting the secondary particles emitted along the direction pointing to the hall. The focusing is produced by the toroidal magnetic field present in the air volume between the two coaxial conductors of the horn. The beam of focused, secondary mesons emerging from the target/horn region is further collimated, via passive shielding, and allowed to decay into neutrinos in a cylindrical decay region filled with air at atmospheric pressure, 50 m long and 90 cm in radius. The polarity of the horn current flow can be (and has been) switched, in order to focus negatively charged mesons, and therefore produce an antineutrino instead of a neutrino beam.

Neutrino flux predictions are the same produced by the SciBooNE collaboration, obtained via a GEANT4-based beam Monte Carlo simulation [1]. The same simulation code developed by the MiniBooNE Collaboration is used, where a realistic description of the geometry and materials present in the BNB target hall and decay region is used. Primary protons are generated according to the expected beam optics properties upstream of the target. The interactions of primary protons with the beryllium target are simulated according to state-of-the-art hadron interaction data. Of particular importance for this analysis is a π^+ production in proton-beryllium interactions, which uses experimental input from the HARP [cite] and BNL E910 [cite] experiments. Production of secondary protons, neutrons, charged pions, and charged and neutral kaons is taken into account, and elastic and quasi-elastic scattering of protons in the target are also simulated. Particles emanating from the primary proton-beryllium interaction in the target are then propagated within the GEANT4 framework, which accounts for all relevant physics processes. Given the importance of the target (beryllium and aluminium) hadronic reactions, these are described by custom models, while other hadronic processes and all electromagnetic

¹The late pulse is caused by the back scattering of the photoelectrons on the first dynode without multiplication. The after pulse is provoked by residual ionisation in the vacuum tube which produces an additional photoelectron.

processes (energy loss, multiple scattering, effect of horn magnetic field, etc.) are described according to default GEANT4 physics lists.

A second, FORTRAN-based Monte Carlo code is responsible for generating the neutrino kinematics distributions from meson and muon decays, and for obtaining the final neutrino fluxes extrapolated to the detector hall with negligible beam Monte Carlo statistical errors. Once produced by the simulation, neutrinos are extrapolated along straight lines toward the detector and all neutrinos whose traces cross any part of the active volume are considered for the flux predictions. Based on accurate survey data, the distance between the centre of the beryllium target and the centre of the SciBar detector is taken to be 99.9 m, with the detector located on beam axis within a tolerance of a few centimetres.

The neutrino flux prediction at the detector location and as a function of neutrino energy is shown in Fig. 2.2. A total neutrino flux per proton on target of $2.2 \times 10^{-8} \text{ cm}^{-2}$ is expected at the hall location and in neutrino running mode (positive horn polarity), with a mean neutrino energy of 0.7 GeV. The flux is dominated by muon neutrinos (93 % of total), with small contributions from muon antineutrinos (6.4 %), and electron neutrinos and antineutrinos (0.6 % in total). For the neutrino flux predictions, no information from BNB (SciBooNE or MiniBooNE) neutrino data was used as experimental input. The projected number of protons incident on the target (POT) per year for the BNB is about 2×10^{20} POT. The rates expected per year when running in neutrino mode for one ton of water (see section ref) are about sixteen thousands neutrino interactions, where eleven thousands of those would be ν_μ CC interactions. This spectrum peaks ideally in the region of interest at 700 MeV as a result of the simulation shown in Fig. 2.2, and has the target rate of neutrino interactions per year. Another consideration beyond the rates and spectra of in-detector neutrino interactions is the probability of seeing multiple events in one beam spill. The number of muon neutrino per spill at the SciBooNE location is found to be significantly less than one. In fact from the preliminary simulations, the neutrino interactions occur in the tank approximately every 150 spills of 4×10^{12} POTs. Additionally our simulations suggest an externally generated muon enters the tank once every ~ 195 spills. These rates are ideal as they ensure single neutrino interactions in the detector.

2.3 The Hall

The experiment is set up in the former site of the SciBooNE experiment, located 8 m below the surface and the 100 m from the BNB target. Already existing instrumentation in the hall is borrowed by the ANNIE experiment.

2.3.1 Water tank

The main component of the experiment is the water tank, built and installed in the hall. It consists of a welded steel water tank, which dimensions are 10 ft (slightly more than three metres) of diameter per 13 ft (nearly four metres) of height, enclosing roughly 23 tonnes

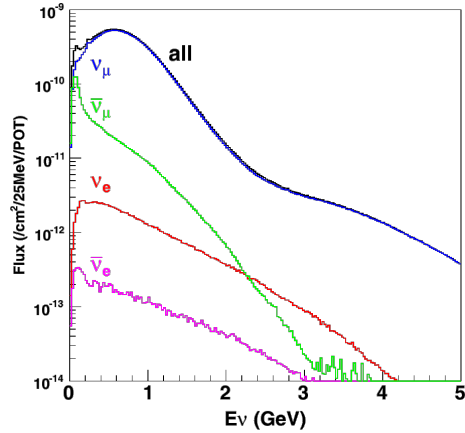


Figure 2.2: Neutrino flux predictions from the GEANT4/FORTRAN simulation. Picture taken from cite.

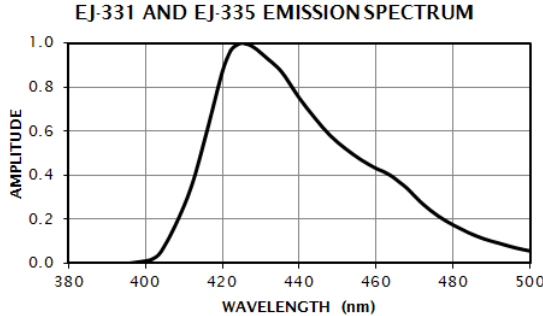


Figure 2.4: EJ-335 emission spectrum. This scintillator contains mineral oil substituted for some of the aromatic solvent for purposes of higher hydrogen content and higher flash point for use in very large tanks. The gadolinium content is 0.25% by weight. The wavelength of peak emission is 424 nm.

of water. The characteristic dimension of the tank can be compared to the diagonal of the cylinder, which is about five meters. It corresponds to circa seventeen light-nanoseconds. The inner volume is lined with a black, water tight plastic bag and outfitted with a PVC (87 % light reflection) inner support structure mounted with 60 PMTs, and capable of ultimately housing several hundred photo-sensors. The tank is filled with pure water and used in conjunction with a smaller acrylic vessel containing Gd-loaded scintillator to measure neutron backgrounds, called Neutron Volume Capture (NCV). Due to its two orders of magnitude smaller volume compared to Super-Kamiokande, ANNIE's water transparency requirements are less stringent: ANNIE needs only to keep a transparency about 25 meters to lose less than 10 % of the light, as opposed to SK's effective water attenuation length of 90 meters. The ANNIE water volume requires a source of dry nitrogen in order to suppress the growth of biologics in the water. This nitrogen is bubbled through the water during fill and afterwards a blanket of nitrogen will be maintained above the surface of the water. The re-circulation is kept as low as necessary to maintain a pure N₂ environment. ANNIE also relies on the plastic liner to prevent ions, that might compromise transparency, from leaching into the water from the tank walls. Water quality is supposed to be monitored using the detected light intensity from cosmic ray muons.

A concentrated solution of high-quality (99.99% TREO²) gadolinium sulphate Gd₂(SO₄)₃ will be mixed in a portable polypropylene barrel with pure water. The available 50 kg of Gd are enough for one test loading (4 kg) and one full loading (40 kg), with 6 kg left over for various other studies and tests. Thanks to the complex of water re-circulation system, the Gd-loaded water can be removed and stored in a secondary tank, then returned and re-purified with minimal loss of Gd, between ANNIE's runs. Upon completion of the experiment the gadolinium can be easily recovered using a portable demineraliser. Measurement of neutron background will be possible thanks to the NCV. It consist of a moveable 2.5 cm thick, 50 cm×50 cm transparent acrylic vessel, which holds 100 L of Gd-doped EJ-335 liquid scintillator, specialised for neutron detection. The light spectrum is shown in Fig. 2.4.

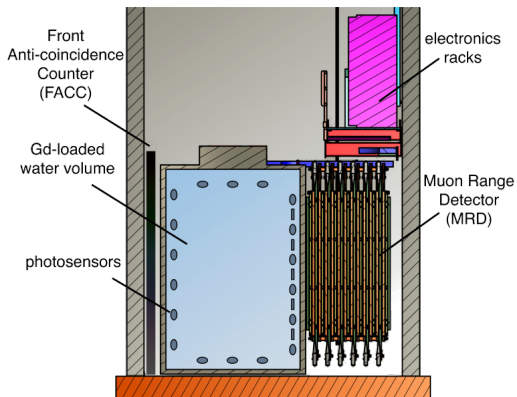


Figure 2.3: Schematic of the experimental hall.

²TREO expresses the Total Rare Earth Oxide percentage in the element.

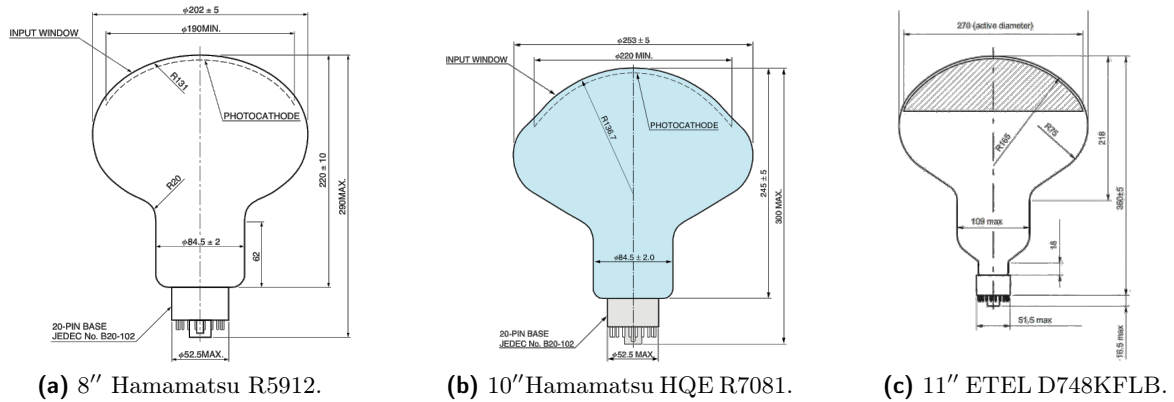


Figure 2.5: Schematic of the PMTs selected for the experiment.

The vessel is weighted so as to have a negative buoyancy. Position dependence of the neutron rates from different overburdens of water can be studied by raising and lowering the NCV and translating it along the beam axis.

2.3.2 Photodetectors

Voltage of PMTs, positive because of water. Little electric scheme? Impedance etc. The core of the experiment is the Cherenkov light detection. The coverage provided by 60 8'' PMTs borrowed from the WATCHBOY experiment³ is enough for the Phase I. The photomultipliers are mounted in a frame on the bottom of the tank, facing upward. The frame is designed to support both the weight of the phototubes in gravity as well as the buoyant forces in water. The detectors, immersed in water, are operated at a positive high-voltage (HV), with a single cable for both power and signal. This is due to the fact that the water volume acts as a ground and the employed voltages could lead to electrical breakdown through the glass of the PMT, if a negative voltage is applied to the cathode. Supplying a positive voltage to the anode, instead, help avoid this issue, since the cathode is set to ground. Capacitors are required in order to filter the signal from the power supply voltage.

As noted earlier, the necessary photo-coverage to reconstruct events in water will be achieved in ANNIE Phase II by:

- reusing the 8'' Hamamatsu PMTs recovered from ANNIE Phase I.
- purchasing new High Quantum Efficiency (HQE) 10'' Hamamatsu PMTs;
- employing refurbished 11'' Electron Tubes Enterprise PMTs ref[arXiv:1512.06916v2].

In order to determine the necessary photocathode coverage, a series of simulations has been run with different sizes and numbers of PMTs. These full simulations consider neutron captures on both Gd (90 %) and the hydrogen from the water (10 %). After cost and availability are taken into account, it is found that the detection can be optimised by using 58 8'' tubes, 20 11'' tubes, and 45 HQE 10'' tubes. Detection probability depends on the number of PMTs hit per neutron capture. Gadolinium captures typically produce several photons, therefore the probability of observing enough hits to detect the event

³The WATCHBOY experiment was designed to measure the rate of radionuclide production in water created by muon spallation. Three primary nuclei of interest, ^{11}Li , ^8He , and ^9Li , can produce a high energy beta particle in coincidence with a neutron, thus mimicking an antineutrino induced inverse beta decay. The experiment was constructed in 2013 at the Kimballton Underground Research Facility (KURF) in Virginia, US.

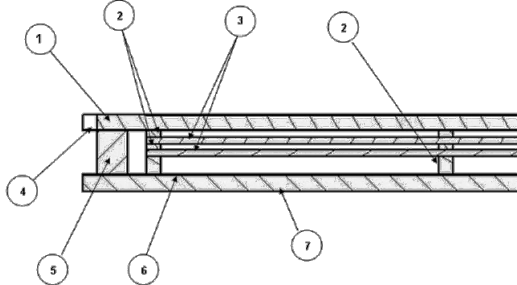


Figure 2.6: The basic structure of the LAPPD detector. The sealed vacuum tube consists of a top window with the photocathode on the inner surface (1), an accelerating gap for the initial photo-electron (2), a pair of 20-cm-square MCPs in a Cherenkov geometry that amplify the photo-electron by factors up to 5×10^7 (3), a gap after the output of the second MCP (2), and the anode that collects the exiting electrons (6). The package is less than 15 mm thick.

is related to the number of photoelectrons produced. This number is strictly correlated with the number of hits. The predictions agree well with a simple scaling argument based on measurements at Super-Kamiokande. Using the planned mix of 11" tubes, 8" tubes, and HQE 10" tubes, it is found that 5 (good correlation) and 10 (strong correlation) photoelectrons are produced respectively 99 % and 94 % of the time.

Precise vertex reconstruction will be required for the next stages of the experiment. In addition to the PMT coverage improvement, the use of advanced, high resolution photodetectors could have a transformative impact on future neutrino detectors relying on light collection. The most promising technology, selected for ANNIE, is the Large Area Picosecond Photodetector (LAPPD), a microchannel plate (MCP) based photomultiplier. Thanks to atomic layer deposition (ALD) technique⁴, is possible to produce large-format MCP detector systems using by conformally coating inactive, micro-pore glass substrates. The technique allows for the independent optimization of the geometric, resistive, and secondary electron emission properties of the channel plates. The final detector can achieve single photoelectron time resolutions less than 100 ps and spatial imaging capabilities to within a single centimetre. This provides a much crisper detection of the Cherenkov radiation edge and greatly improves the ability to distinguish between closely separate rings, compared to PMTs which have time resolution of the order of the nanosecond and act as a single pixel, despite the large active area. The combination of LAPPDs and PMTs allows the full detector to work as a tracking detector, with track and vertex reconstruction approaching size scales of just a few centimetres. It also favours the reconstruction of events very close to the wall of the detector, thanks to the small thickness of the LAPPDs (less than 1.5 cm): the fiducial volume is thus maximised. The LAPPD capabilities also translate into better energy resolution and better discrimination between dark noise and photons from neutron captures. Large Monte Carlo ensembles show that photon pileup on LAPPDs is low enough that only one or two hist per channel are typically visible. Thus, each photon can individually be measured. Preliminary studies show that 20 LAPPDs can provide sufficient coverage and have well-suited performance characteristics for addressing the challenges of water Cherenkov reconstruction in a small volume. Better reconstruction could be possible as larger numbers of LAPPDs become available. Reaching a 10% isotropic coverage would allow not only from identifying multi-track events but in also identifying the constituent particles and the exact topology potentially expanding the physics reach of the experiment.

⁴ALD is a thin film deposition technique that is based on the sequential use of a gas phase chemical process. The process is based on binary reaction sequences where two surface reactions occur and deposit a thin binary compound film.

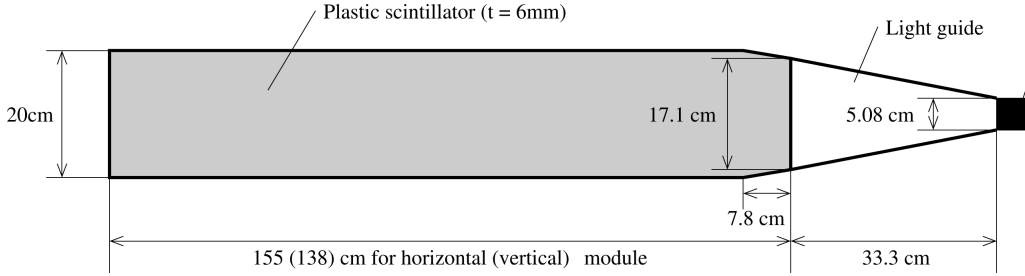


Figure 2.8: Paddle used for the MRD.

2.3.3 Veto system and Muon Range Detector

ANNIE is composed of two more detectors other than the water tank in the hall: the Veto system and a muon detector.

The Veto is provided by a Forward Anti-Coincidence Counter (FACC) consisting of two layers of overlapping scintillating paddles. Each layer employs 13 paddles to detect charged particles produced in the dirt upstream of the hall or muons from the BNB, which hasn't decayed. This allows the rejection of events in the tank unrelated to neutrino interactions. It employs 2" PMTs to read the signals from the scintillator.

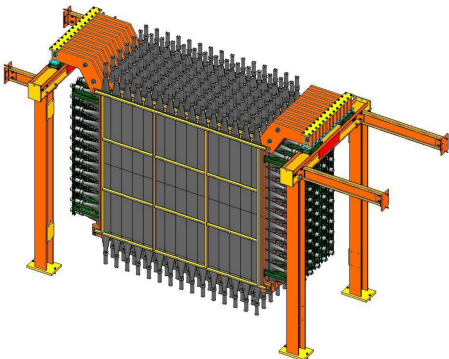


Figure 2.7: Drawing of the MRD.

An iron-scintillator sandwich, inherited from the SciBooNE experiment, is also in the hall. The Muon Range Detector (MRD) is used to range out and fit the direction of daughter muons produced by CCQE interactions in the water target. Its schematic drawing is shown in Fig. 2.7. The muon's energy can be reconstructed thus giving also a handle on the neutrino energy. The MRD is designed to measure the momentum of muons up to 1.2 GeV/c using the range measurement. It consists of 12 iron plates and 13 alternating horizontal and vertical scintillator planes. Each iron plate is 5 cm thick, and covers an area of $274 \times 305 \text{ cm}^2$. The total mass of absorber material is approximately 48 tonnes, while the detector weighs about sixty tonnes. The density of a spare iron plate has been measured at several positions of the plate, to be $7.841 \pm 0.002 \text{ g/cm}^3$. Each scintillator plane consists of 20 cm wide, 6 mm thick scintillator paddles, as illustrated in Fig. 2.8. Each vertical plane is comprised of 138 cm long paddles, arranged in a 2×15 array to have an active area of $276 \times 300 \text{ cm}^2$. On the other hand, each horizontal scintillator plane consists of 155 cm long paddles, arranged in a 13×2 array to have an active area of $260 \times 310 \text{ cm}^2$. In total, 362 paddles, 182 vertical and 180 horizontal, are used in the MRD. The scintillator paddles are read out by five types of 2" PMTs; the vertical planes consist of Hamamatsu 2154-05 and RCA 6342A PMTs, the horizontal planes consist of EMI 9954KB, EMI 9839b and 9939b PMTs. All PMTs used for horizontal modules have 14 stage dynodes, while those used for vertical modules have 10 stage dynodes. This choice is due to space limitations. Hence, the PMTs used for the vertical planes have relatively low gain and efficiency compared to that used for horizontal planes. To ensure the same efficiencies, the vertical modules are amplified by the factor of 10 using LeCroy 612 amplifiers. **MRD is not magnetised.**

As far as the electronics are concerned, the FACC and MRD are essentially the same system. Both detectors are composed of scintillating paddles and small phototubes, and

both detectors follow the same rectilinear geometry. The FACC consists of two layers of 13 horizontal paddles. On the MRD side, only a fraction of the detector is operation for Phase I of ANNIE. One vertical and one horizontal layer of the MRD (the second and the third layers, respectively) are read. *Layer 2* consists of two sets of 13 horizontal paddles, while *Layer 3* consists of two sets of 15 paddles. The number of needed readout channels from these two subsystems are

- 26 channels for the forward Veto;
- 26 channels for *Layer 2* of the MRD;
- 30 channels for *Layer 3* of the MRD;

for a total of 82 channels.

In place of the full CAMAC electronics implementation (see section ref), the two detectors signals are summed and read by VME electronics (section ref) to give a primary handle on these devices. CAMAC electronics (see section ref) is employed to read these channels.

Chapter 3

Data Acquisition system

Modern high energy Physics experiments require automated procedures to collect data from detectors and save them in long term storage for ensuing analysis. These routines are gathered in automated system called Data Acquisition systems (DAQ), which typically include three fundamental components:

1. sensors, to convert physical parameters to electrical signals;
2. signal conditioning circuitry, to convert sensor signals into a form that can be converted to digital values.
3. conversion from analog signals to digital values and subsequent storage.

The last step is vital in that it allows data manipulation and analysis by a computer.

As far as ANNIE is concerned, the first requirement has already been mentioned in section 2.3.1: the experiment has multiple simultaneous data sources, i.e. the forward Veto, water PMTs and the MRD, as well as a blend of front-end electronics technologies (VME, CAMAC and custom FADCs) for ADC/TDC and waveform digitisation. Considering this variety of devices, the whole system has also some requirements to achieve:

- stability, on long acquisition runs;
- handling over all the aspect of the experiment;
- calibration;
- real time online monitoring;
- direct and remote user control.

Provided a solid electronic system, these tasks are thoroughly accomplished on the software's side, since the system is based upon the *ToolDAQ Framework*¹, developed by Dr Benjamin Richards [ref] for the Hyper Kamiokande collaboration (HK). The HK group has used this opportunity to undertake R&D and testing of DAQ software and tools for future use in the HK experiment. ANNIE has allowed extensive testing of the flexibility of the software and all the above features to take place within a single deployment.

ToolDAQ is designed to incorporate the best features of other frameworks along with:

- being very easy and fast for developing DAQ implementations in a very modular way;
- scalable network infrastructure, provided by a service discovery protocol, to allow its use on large scale experiments.

¹ToolDAQ is open source and available on GitHub [repo].

The main executable relies on user-defined modular classes, called *Tools*, which present three chief functions: *Initialise*, *Execute*, and *Finalise*. The Tools can be daisy-chained to a *ToolChain* and then handled sequentially by the process whenever one of those functions is called. A ToolChain also manages the more complicated aspects of the DAQ system, like the remote control, the service discovery, and the status of its Tools. Parameters, data and other variables are passed between Tools by an editable shared data class. Each tool is allowed to read, update, and modify it, due to it is owned by the ToolChain. The bare structure is sketched in Fig. 3.1.

In the following sections, the whole DAQ structure is delineated as it currently is. It is composed of three parallel ToolChains: the Main DAQ Chain, the VME Chain, and the CAMAC/MRD Chain. The latter hasn't been implemented in the Main DAQ system yet, which is composed by the first two Chains only. At the moment the MRD Chain is employed as a standalone DAQ, working aside to the Main DAQ, on a different CPU with understandable difficulties. Ways of overcoming this issues and future integration of the two DAQ in the same machine are also discussed.

3.1 Main DAQ Chain and VME Chain

3.1.1 Hardware

The primary readout for ANNIE Phase I is provided by a VME-based system developed for the KOTO experiment² by University of Chicago. The *VMEbus* is a computer architecture, where “VME” stands for VERSA Module Eurocard. It is widely used in High Energy Physics due to the fact that it is of public domain and its data transfer speed is quite fast³. The crates are governed by a VME-based CPU board, interfaced with an Internet Rack Monitor system (IRM) of Fermilab. The latter allows network connection and supports widely-used Internet protocols that manage data request and setting access as well as alarm reporting, all based upon the User Datagram Protocol (UDP) transport layer.

The system consists of two types of VME module:

- custom flash analog-to-digital converters (FADC), each with four channels, 500 MHz sampling pipeline, 14 bit resolution
- Master Trigger (MT) cards which distribute the 125 MHz clock, synchronises the FADC cards, provides the trigger, and provides a *busy* signal.

The leading edge of photomultiplier signal is too fast for an 8 ns sampling. To reduce dead time and allow the 500 MHz sampling, the output signals from the detectors are stored in 8000 samples pipelines inside Field Programmable Gate Arrays (FPGAs) until a trigger decision is made. The three levels trigger system uses the waveform information with increased sophistication at each level. Each MT card can address 8 FADC cards, but

²The KOTO experiment at J-PARC, Japan, aims at observing the rare kaon decay $K_L \rightarrow \pi^0 \bar{\nu} \nu$ to search for new physics beyond the standard model that breaks the CP symmetry. The experiment, with a new beam line and new detector components, is underway and the first run was performed in May 2013.

³For instance the latest manifestation, the VME320/2eSST protocol, can double the theoretical bandwidth of VME to 320MB/s. cite[<http://www.vita.com/VME320-2eSST-Protocol>].

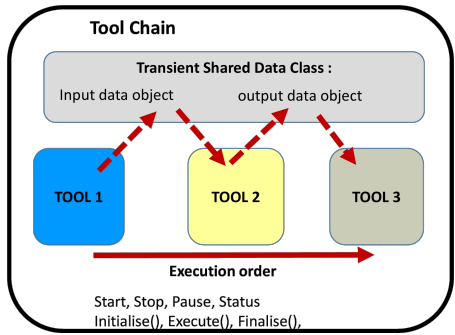


Figure 3.1: Schematic of a ToolChain.

can be daisy-chained or arrange hierarchically to address more total cards. Given the 16 FADC cards of the ANNIE readout, 3 MT cards are used: one Level-0 card distributes the clock between two Level-1 MT cards, each addressing 8 FADCs. For storage limitations, a down-sampling to 125 MHz was established. The resolution of 8 ns suffices the needs of the R&D stage of Phase I. Given that an 80 μ s long time window is collected, four data sets can be hold in the 40000 samples buffer with this time resolution. Each set corresponds to a spill from the beam.

The system primarily records the traces from the PMTs in the ANNIE water volume. The Muon Range Detector and the Forward Veto nominally rely on the same FADC system, but the signals from the scintillating paddles are combined through an analog OR and sent to a few spare FADC channels on the KOTO boards.

3.1.2 Software

The data from the water PMTs and the logical sum from the Veto and MRD are acquired by the Main DAQ, which hinges upon two strictly complementary ToolChains: the Main Chain and the VME Chain. The Main Chain is the primary ToolChain of the DAQ system, which communicates with the other two processes.

The Chain's tools are depicted in Fig. 3.2 and they are the following:

Main DAQ	VME
Input variables	
PostSQL	VME Trigger Send
Trigger	Board Reader
Network Receive Data	Network Send Data
Monitor	
Data Recorder	

The *Input variables* tool loads some initialisation parameters and the specification of the current *run*, i.e. data taking session. Three typologies of run are available and are sent to the VME CPU: a test run, an LED run for PMTs calibration, a pedestal run, and a beam run. The triggering of the digitisers is influenced by changing the kind of the run. For instance, a beam run is triggered by the RWM, while an LED run is triggered by the LED pulser. The *PostSQL* tool updates an SQL database of the DAQ, where all the information about the run, such as the number of events, the start and the stop time, and others, are saved. *Trigger* tool blocks the Chain, awaiting and sending a trigger query from the VME. When the VME replies, the Chain is run back again. As explained, four 10000samples data sets are collected from the VME cards, which equates to four consecutive spills from the beam. The *Network receive data* tool handles the data transfer via ZeroMQ messaging⁴ between the main chain and the VME one. Like most of the HEP experiments, even ANNIE requires real-time monitoring so as to check whether the DAQ system works flawlessly. This is achieved by the *Monitor* tool, which updates a dedicated web-page with random plots of data collected.

On the VME electronics side, the Chain communicates with the VME CPU retrieving all the information about the cards and the trigger. The *Trigger Sender* tool check the status of the VME controller. If the ADC are triggered, a trigger message is sent to the Main Chain. The data are dumped from the FPGA's buffer by the *Board Reader* tool and are sent to the Main Chain via ZeroMQ messaging over TCP.

⁴ZeroMQ is a high-performance asynchronous messaging library, aimed at use in distributed applications. The API provides *sockets*, each of which can represent a many-to-many connection between endpoints, operating with a message-wise granularity. ZeroMQ is developed by a large community of contributors and distributed under the LGPL license. <http://zeromq.org/>

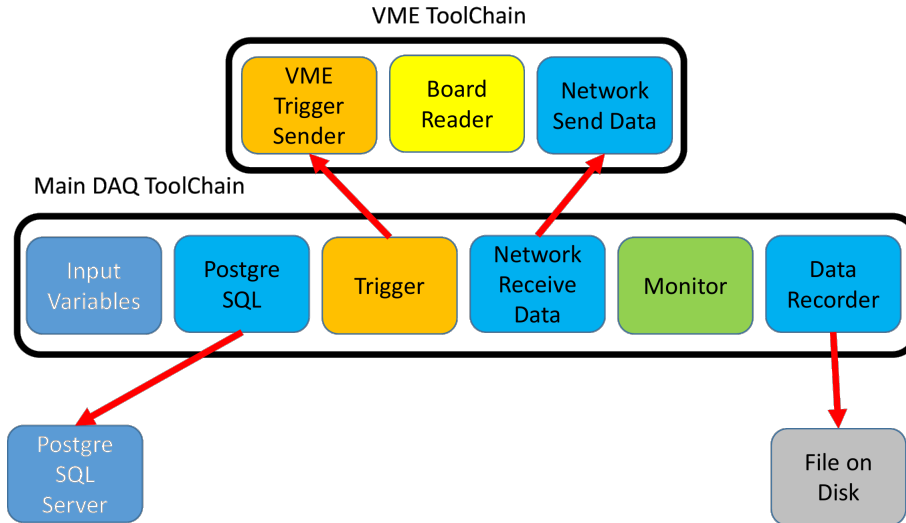


Figure 3.2: ANNIE’s current main DAQ makes use of two parallel tool chains.

The last tool of the Main Chain, *Data recorder*, saves data into the following ROOT tree structure:

LastSync : time of data acquisition;

SequenceID : incrementale number;

StartTime : same as lastsync;

CardID : number of ADC card;

Channels : channel of ADC card;

PMTID : global identifier of PMT (labelled from 1 to 60);

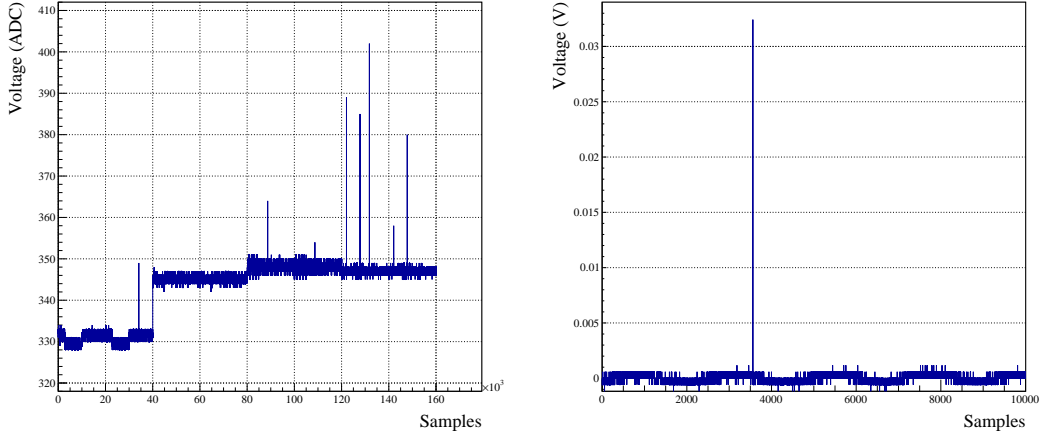
BufferSize : size of the buffer per channel;

FullBufferSize : size of the buffer per card;

Data : an array holding the full buffer of a single card.

Each entry corresponds to an acquisition of the full buffer from the cards saved in a 160000 long float array, i.e. the digitised time profile of four consecutive $80 \mu\text{s}$ data set times the four channels. The ROOT files are then post processed: the buffer is split and an entry is created for each beam event, or trigger, the baseline is calculated and removed from the time profiles, and the precise time stamp is reconstructed. In Fig. 3.3 an example of time profile is shown before and after the post-processing. Moreover, each channel is mapped to its equivalent PMT. This stage reduces the file sizes by a nearly a factor of four.

Provided that the spill’s frequency is ~ 15 Hz and four spills are acquired, the buffer takes around a quarter of a second to fill. The longest portion of the chain to execute is the disk saving and it is meant to be done between pulse trains, so as to minimise the number of spills lost. A whole execution of the chain lasts nearly a second, slightly less than the pulse train frequency.



(a) Before post-processing, arrays include the full buffer from each card.

(b) After post-processing, arrays are split per trigger and hold 80 μ s worth of data.

Figure 3.3: Time profile before and after the post-processing.

3.2 MRD Chain

3.2.1 Hardware

As explained in Sec. ref, the signal from the FACC and two layers of the MRD are logically summed and read by the VME digitisers. The PMTs of these two detectors are supposed to be read individually by both Time-to-Digital Converters (TDC) and ADCs in future stages of the experiment and for this purpose a third ToolChain has been developed to collect data from both the VETO and the MRD’s second and third layers (see section ref).

CAMAC⁵ electronic modules are employed for these two detectors: LeCroy 3377 modules for the time digitisation, while LeCroy 4300B for analog conversion.

The LeCroy Model 3377 is a 32-channel time-to-digital converter (TDC) and optimised with a low conversion time and a high speed readout of 100 ns/word. With 10-bit words, the longest time window achievable is 4088.0 ns, using a resolution of 4.0 ns. A delayed signal from the RWM acts as a “common start” for the TDC cards and each internal counter is individually stopped by hit signals. The channels are fed with the discriminated PMT signals of the VETO and of the second and the third layer of the MRD.

The LeCroy Model 4300B FERA contains 16 independent 11bit charge-to-digital converters. An 8-bit register and a memory containing the individual pedestal values to be subtracted from each ADC are also available. These converters haven’t been installed in the electronic chain yet. Nevertheless the software interface has been developed anyway.

All the cards are addressed via the Weiner CCUSB controller module. The CCUSB is a full-featured CAMAC Crate controller with integrated high speed USB-2 interface. For fast data acquisition applications the CCUSB has a built-in command list sequencer, called *command stack* with data buffering in a 22kB size FIFO. A XILINX Spartan 3 family FPGA performs all CCUSB logic and functions.

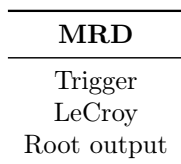
⁵Computer-Aided Measurement And Control (CAMAC) is a bus and modular-crate electronic standard for data acquisition and control used mainly in nuclear and particle physics experiments and in industry. The bus allows data exchange between plug-in modules and a crate controller, which then interfaces to a CPU or to a VME-CAMAC interface.

3.2.2 Software

The thesis's work is mainly focused on the development of a dedicated data acquisition system for the CAMAC electronics of the experiment. A separate MRD DAQ has been created from scratch within the ToolDAQ Framework in order to acquire the MRD and the forward Veto data. These two detectors rely on the CAMAC electronics for front-end read out of the PMTs signals and the USB controller vendor provides a C++ class to interface the controller with the computer.

Some C++ classes were developed with the purpose of handling more easily the modules. A base class takes care of opening the USB connection for the CCUSB controller and storing information on the cards, such as the Slot number. It also allows the configuration of the command stack, i.e. the CAMAC command sequencer. Two derived classes implement wrapper functions to deliver CAMAC commands via the NAF addressing⁶.

The MRD's ToolChain employs the CAMAC classes to interface with the controller and the cards. As illustrated in Fig. 3.2, the Tools contained in the Chain are:



The *Trigger* tool reads the FIFO of a specified card: if it is not empty, then all cards presenting data are read and other tools are executed. Currently, a hit signal is generated in each TDCs by delaying the common start signal of $\sim 1 \mu\text{s}$, such that the FIFOs are never empty in coincidence with the beam's spills. Three triggering behaviours are supported: external trigger, software trigger with random card access, and software trigger with card test function.

The *LeCroy* tool is meant to work for both the TDCs and ADCs cards. If only either TDCs or ADCs are employed, then only one tool should be added in the *ToolChain*. Otherwise, if both are used, then two *LeCroy* tools are required. Given that the ADCs haven't been installed in the crates yet, only one tool is needed for the TDCs. Nevertheless the charge converters have been tested, as well.

The last tool fills a ROOT tree and save it to file. The tree has the following branches:

Trigger : incremental number of the trigger;

OutNumber : number of channels read;

Type : string telling whether the data refer to TDC or to ADC;

Value : actual value retrieved from the card.

Slot : slot number of the card;

Channel : channel of the card from which the value was retrieved;

TimeStamp : UNIX time stamp of the entry, since epoch, in ms.

The MRD Chain runs in a different PC than the Main DAQ and the ToolChain is executed at a different speed, for it is a standalone process. For this reason, a method has been realised to correlate the events between the two DAQs. Timestamps were designated for this fundamental task: both DAQs assign UNIX time to each event, since the clocks are synchronised to the same NTP server, which uses GPS time sources. With the help

⁶Module addressing is achieved knowing the slot Number, the subAddress, and the Function code.

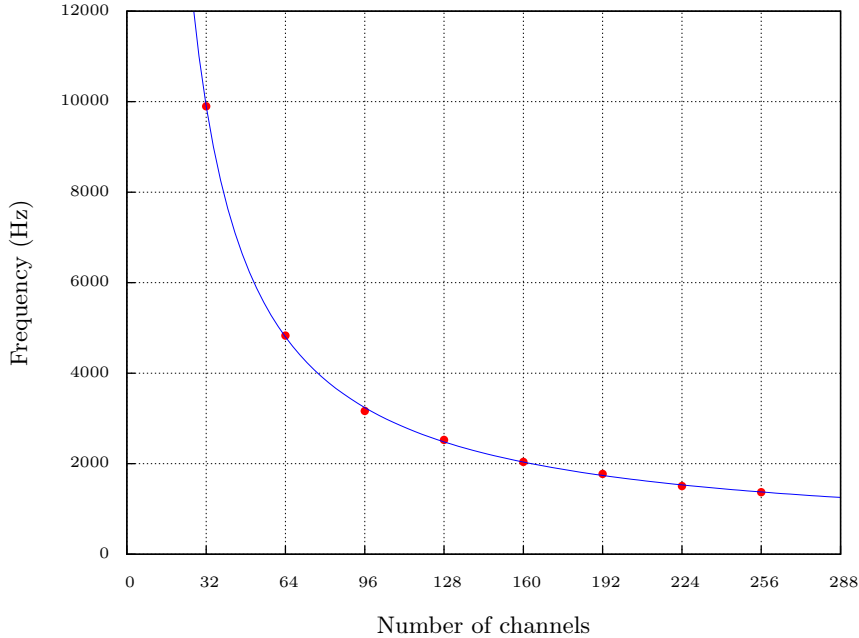


Figure 3.4: DAQ frequency reading TDCs with all channels fired, but 1.6% time occupancy.

of the Fermilab spill database [ref here], the events from the two DAQs can be related to each other.

This method is effective as long as the frequency of the chain execution is greater than the spill frequency. The frequency should be above the 15 Hz spill frequency in order not to miss any beam event. However the CAMAC event rate has been found to be quite low in this early stage, around 0.20 Hz⁷, since only two layers of the MRD are used, in addition to the Veto. This suggest that the modules present data only the ~1.3% of the time.

Concerning the MRD DAQ, the longest portion of the chain is the CAMAC addressing and data collecting. The software has been tested using software triggering, employing the test functions of the modules, and counting the time required for 100,000 repeated cycles with 1.3% firing probability; the frequency was afterwards estimated. The result is shown in Fig. 3.4, where frequency vs number of channel is plotted for TDC modules. It's clear that the frequency is well above the lower theoretical limit of 15 Hz. Rescaling the frequency to full time firing, i.e. the number of channel to be read is maximum for every DAQ cycle, the limit is easily reached with just ten modules, corresponding to five layers of MRD, Veto excluded.

The command stack of the CCUSB controller is not employed, because the USB connection can provide fast enough communication to address all the active cards.

Concerning the TimeStamp, a time variable drift in the MRD TimeStamps has been found, likely due to imprecise synchronisation with the NTP server (accuracy given to be less than 30 ms) which occurs every 1024 ms. A post-processor has been written to fix the TimeStamps, identifying time patterns in the spill spectrum and comparing them to the database information. In Fig. 3.5 a detail of the result of the synchronisation is plotted. The blue lines are given by the database, used as a reference. The TimeStamps before and after the post-processing are printed respectively in red and green.

The post-processor also handles other aspects of the raw data, like converting the module's values into physical quantities and mapping each channel to its PMT.

⁷The rate is measured from output ROOT file, dividing the number of entries, i.e. events, by the time passed between the first and the last TimeStamp.

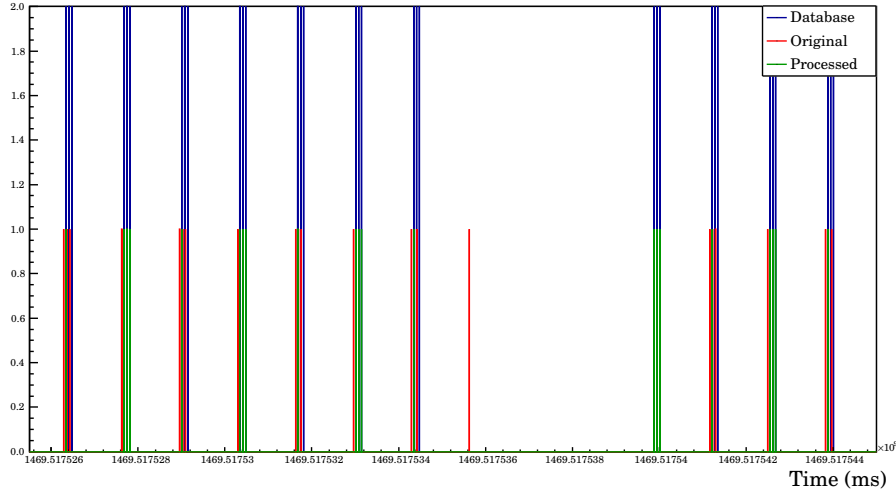


Figure 3.5: Detail of the time stamp alignment with the database data.

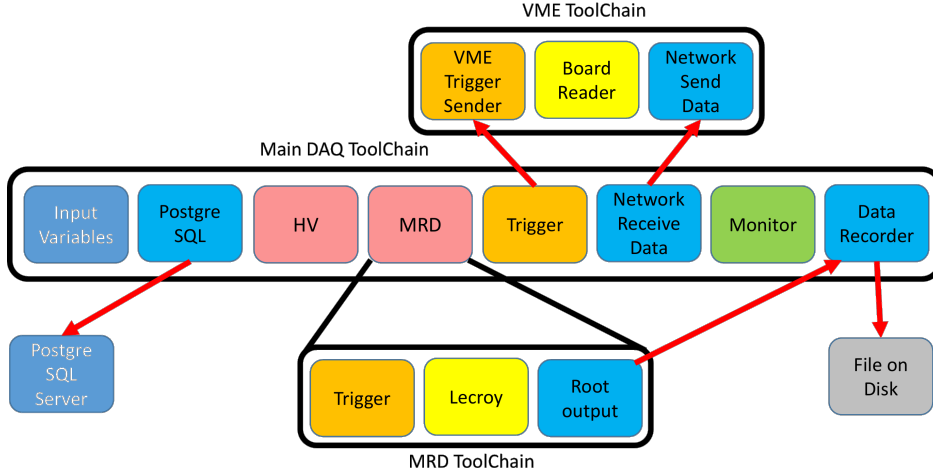


Figure 3.6: Final version of ANNIE's DAQ, with all the Chains integrated.

3.3 Future improvement

The final version of the DAQ system needs a full integration of the Main Chain with the CAMAC one. A possible solution is depicted in Fig. 3.6. A new tool could be employed to embody a simplified version of the MRD ToolChain, rather than run it in a parallel process. The MRD Chain, as proved in previous sections, is fast in execution, so it should not significantly slow down the Main DAQ. In this way, the TimeStamp synchronisation technique is not required anymore because all the acquisitions are done by the same CPU and simultaneously. As far as the output files are concerned, the ROOT trees could be merged into a single ROOT file triggering the two recording tools with ZeroMQ communication. Final reconstruction of PMTs data and MRDs could be done in a post-processing stage.

In view of the next phases of the experiment, an other DAQ-related issue is the memory storage. During early test runs, the digitiser would sample at a frequency of 500 MHz, but it has been promptly downgraded to 125 MHz because of lack of long term memory storage. As a matter of fact, noise is mostly shown in the 80 μ s time window and the meaningful signal is limited short, compared to the time window. Considering that an high time resolution is pointless in the R&D stage of the experiment, the downgrade was established.

Soon, *zero-suppression* method would be employed, which will definitely overcome storage needs. The preliminary data analysis undertaken can back this decision up, as explained in section [ref].

Chapter 4

Data Analysis procedures

Interpreting the electronic signals produced by the detector is a mandatory step for event reconstruction process. Energies, momenta, and directions of the involved particles must be established in order to determine the detected physical interaction, whose study is the ultimate goal of the experiment. ANNIE's early stage data have been studied and analysis algorithms were developed and tested from scratch: they are implemented in a purpose-built software, which studies the signals acquired from the water PMTs. The code's procedures relies on individual pulse analysis and it is largely focuses on the rejection of background with respect to event signals. Some of these methods, illustrated, in this chapter could be employed into a more complete analysis framework, valid even for the future phases of the experiment.

4.1 Data selection

The Main DAQ is programmed to create a new *Run* every time the Chain is stopped and restarted. Due to being an R&D phase, the DAQ has been improved in various occasion during data taking, hence the size and the number of post-processed files, that constitute the *Runs*, are not constant. Nevertheless high statistics were achieved most of the time. The post-processed ROOT files (see section ref) from the DAQ are used in the data analysis. The buffer retrieved from the VME boards is properly split for each trigger, either hardware or software, in that each set of data consists of $80\ \mu\text{s}$ worth of digitised signal. A single file holds 383 full buffers and this translates to 1532 triggers, or physically speaking to 122.560 ms.

Two distinctive couples of consecutive runs were selected as model data set, with the intention to outline the best data analysis procedures. These are:

- two runs with the beam off and a random trigger: these data are mostly *cosmics*;
- two runs with the *beam* on, but with one PMT mounted on top of the NCV, in order to observe the neutron capture.

All the couples have been merged in single files after being scanned by the data analysis algorithm and so treated as ones. Their quantitative features are shown in Tab. 4.1. For the analysis's sake, the *beam* and the *cosmics* data set are the same, but for a different photodetector.

4.2 Individual pulse analysis

The data analysis software scans all the post-processed time profile which the *Run* consists of, as the one shown in Fig. 4.1, sorted by trigger and PMT number. Any peak

Run type	N of files	N of Triggers	Total time (ms)	Data size (MB)
Cosmics	142	217,544	17,403.520	106,130.447
Beam	164	251,248	20,099.840	122,542.009

Table 4.1: Runs selected for data analysis. They are composed of different numbers of file, resulting in diverse number of triggers. Total time is the number of triggers times 80 μs . The listed memory sizes refer to the post-processed files.

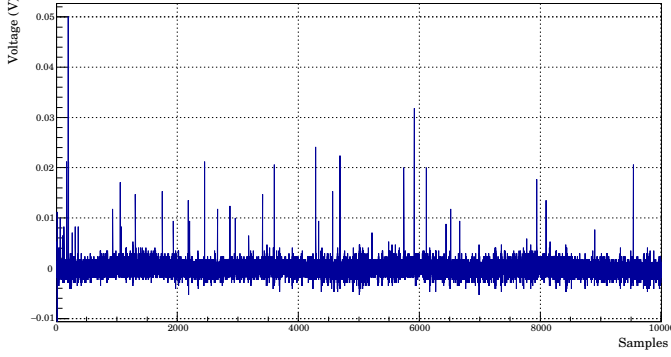


Figure 4.1: Time profile of a single trigger: the signals of the sixty PMTs are here overlaid.

above a certain voltage threshold, V_T , is selected and an enclosing time window of a predefined length, L , is trimmed around it. A length of $L = 100$ samples was chosen, resulting in a 0.8 μs long window. The position of the peak inside this window was set to 20% of its length, i.e. the peak is always set at 0.16 μs from the beginning of the time window. These subsets of data are called *pulses* and are collected in another ROOT file. The choice of window length and the peak position is the result of a compromise between speed of the code, memory usage and loss of physical information. In fact, many pulses shows consecutive multiple peaks, as the one in Fig. 4.2, mainly given by light reflections in the water tank.

Each pulse is individually analysed and processed by a routine of algorithms. As a result, a set of values is gathered from every pulse, in addition to Veto and MRD coincidences. These quantities, outlined in Fig. 4.3, are useful for following analysis and they are labelled as:

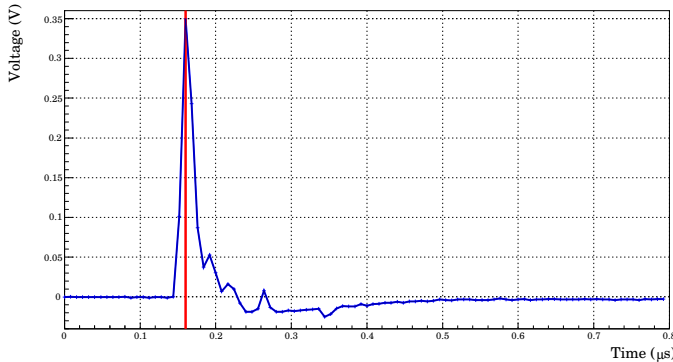


Figure 4.2: Time profile of a single pulse. The red line marks the 20 % of the window's length, at 0.16 μs . The first peak and the second peak are about forty nanoseconds apart, which is the time needed for the light to travel back and forth inside the tank (see section ref).

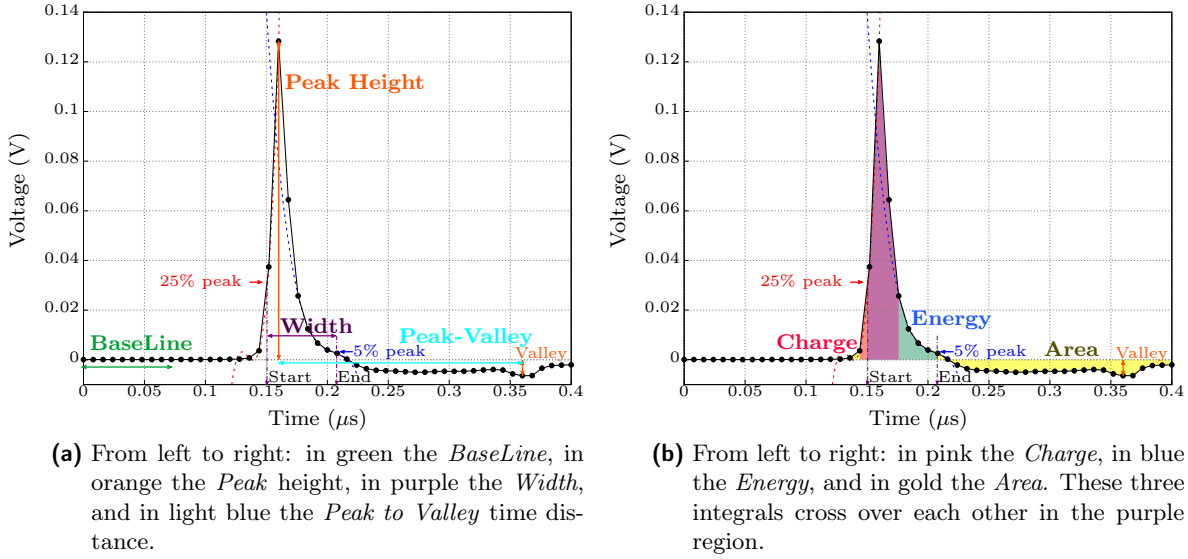


Figure 4.3: Illustration of the pulse analysis values. The 25 % and 5 % peak height marks, which define the Start and End of the signal, are common to both diagrams. The dashed lines represent the cubic interpolations. The shape was realised averaging the collected pulses.

Baseline: it is the arithmetic mean of first ten points of the pulse; this value is then subtracted from the whole array.

Peak: it is the height of the peak (maximum) with respect to the zero.

Start: it is the position of the 25% of the rising edge of the pulse, estimated with precision using cubic interpolation

Previous: is the time difference between the Start and the Start of the previous pulse,

Peak to valley: it is the time distance from the peak to the valley (minimum).

Width: it is the time that spans from Start to the 5% of the falling edge of the pulse (End), calculated using the same algorithm employed for Time.

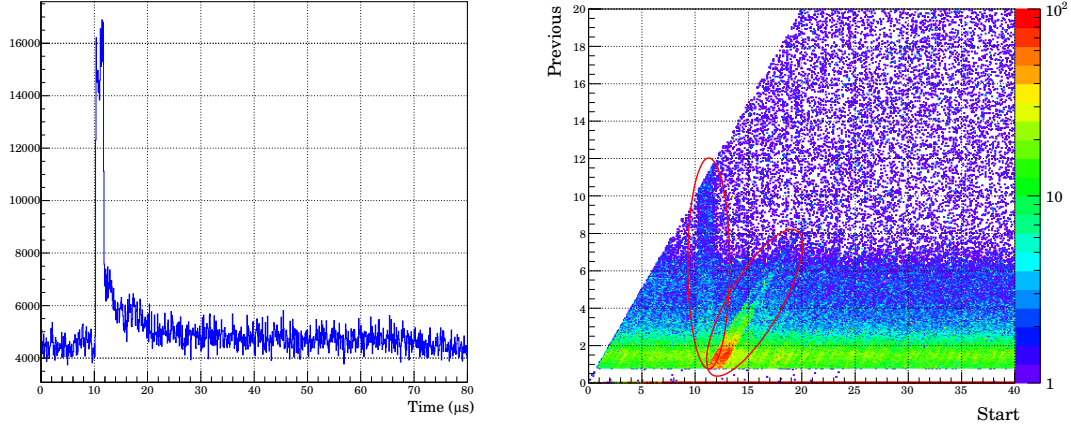
Charge: it is the sum of the 5 points around peak, weighted with the bin width.

Energy: it is the integral of the signal form the Start to the End.

Area: it is the area of the modulus of the pulse. if from the same PMT.

Being a water Cherenkov detector, the event reconstruction in ANNIE relies on time and energy of the signals and for this fact these two quantities must be measured precisely. First of all, each pulse is shifted such that the first ten points of the shape have null mean. Doing so, the *Baseline* are normalised and the peaks of the signals become comparable. The time position of the pulses, or *Start*, is determined with high precision thanks to data interpolation¹, within the time resolution of the ADCs. In Fig. a of 4.4 the spectrum of *Starts* of a beam run is plotted: the frequency boost with respect to the background suggests that the beam occurs ten microseconds after the beginning of the data acquisition.

¹The algorithm looks for four points around the threshold (25 % for the *Start* or 5 % for the *End*), which are used to define a cubic function. Using Newton's method, the correct time position is found.



- (a) The beam is clearly visible at the beginning of the $80\ \mu\text{s}$ buffer; the second half is basically free of beam related events.
- (b) *Start* is plotted against *Previous*; both axes are in μs . The beam pulses are split into two groups: the pulses in the red ellipse are independent of their previous pulse, while a correlation is visible in the set of the blue ellipse.

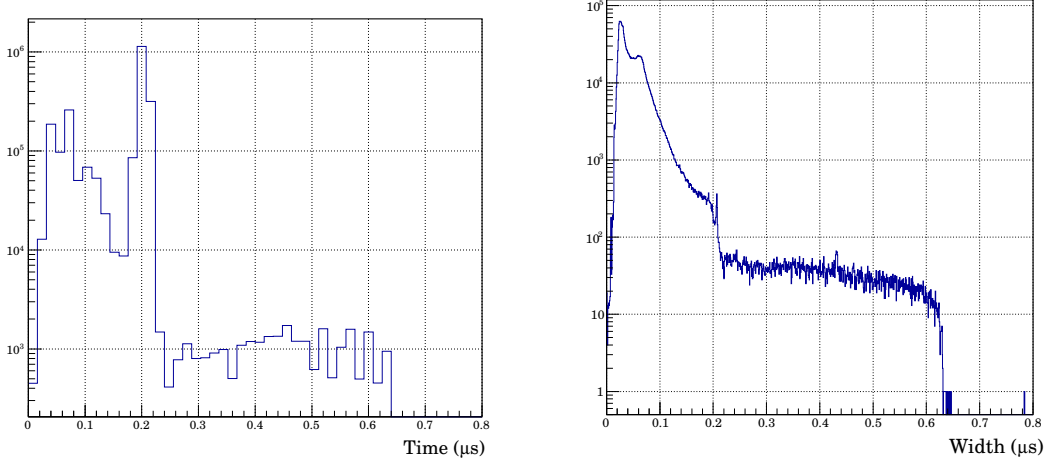
Figure 4.4: Time distribution of the pulses of a beam run.

The distinctive trait of the neutron capture by gadolinium is a delayed signal, detectable tens of microseconds after the main interaction. Therefore studying the relative time distance between pulses is fundamental, particularly in the ANNIE experiment. The *Previous* entry has the potential to accomodate this neccessity and reveal other interesting features. For instance, in Fig. b of 4.4 *Start* is plotted against *Previous*.

Other two interesting and similar quantities are the *Peak to Valley* and the *Width*, whose spectra are reported in Fig. 4.5. The minima, or valleys, are mainly given by negative peaks, as the one in Fig. 4.2, but also visible in averaged pulses. They could be likely due to signal reflection, caused by an impedance mismatch between signal cables and the ADC cards: the shape encounters a smaller impedance on the propagation line, hence it is reflected with the same sign; it is sent back again and inverted when it meets the high impedance of the PMTs. On the whole, the reflection covers the lenght of the line twice. The *Peak to Valley* spectrum suggests that the time delay of the reflection is near $0.2\ \mu\text{s}$, therefore the time needed for a PMT signal to travel to the digitsers is about one hundred of nanoseconds.

Establishing the energy of each shape is more complicated, because of the multiple reflections and possibilities of after-pulses. An evaluation of the pulse integral would be a good indicator of the total charge deposited on each PMT. Three different methods to estimate the area enclosed in a pulse integral have been implemented. The names *Charge*, *Energy*, and *Area* were chosen in order to distinguish them from each other, nonetheless they all are approximations of the charge released by an incoming photon. As shown in Fig. 4.2, there is a partial superimposition of the three: they show indeed interesting correlation patterns, reported in Fig. 4.6. The *Energy* was chosen to be employed for following analysis, in order to make the results coherent with each other.

For every Trigger, the time distribution of the peaks is studied, as well as the time coincidences between the PMTs signals: a time allowance of $0.8\ \mu\text{s}$ is considered to count of pulses happening simultaneously; this easily translates to the number of PMTs fired at the same time. When the latter exceeds a defined threshold, N_{PMT} , then an *Event* is appointed and its precise time position is afterwards estimated by a weighted average of the adjacent coincidences. The multiplicity of an Event is a good indicator of the nature



(a) The distance of the valley with respect to the peak. The mode of the spectrum is at $0.2 \mu\text{s}$.
(b) Distribution of *Width* in logarithmic scale. The spectrum presents an edge near two hundred nanoseconds and then becomes flat. Another edge is visible, close to the peak at shorter widths.

Figure 4.5: Spectra of *Peak to Valley* and *Width*. In both cases, the plot utterly changes for time intervals larger than two hundred nanoseconds.

of the detected interaction. As discussed in section ref, a cosmic muon, likely coming from above, would project the Cherenkov radiation on the bottom of the tank, thus lighting the majority of the water PMTs. On the other hand, a muon arisen from the interaction of a beam neutrino with a nucleon would emit gammas along the beam direction: only a portion of the light cone could be captured, hence the PMTs would be partially triggered. Even natural radioactivity, from radionuclide in the glass of the phototubes for instance, can be detected, although these events have lower multiplicity and are readily filtered by a proper threshold of N_{PMT} . An high-multiplicity event is exemplified in Fig. 4.7.

Not every pulse in a trigger belongs to an event. For instance, in Fig. 4.7 there are at least four pulses outside from the main pulse cluster. These might be likely generated by noise sources and therefore they are useless in view of the event reconstruction. In order to discriminate the pulses, an arbitrary time interval, whose radius is Δ_T , is defined around the Event time position. A pulse that falls within this window is designated as *event*, otherwise as *noise*.

Other orrelation plots.

4.3 Signal and noise discrimination

Discriminating signals from background is a step of utmost importance for data analysis. Being a first stage study, the algorithm only relies on V_T , N_{PMT} , and Δ_T , in order to distinguish event pulses from noise ones. It is necessary, even for future analysis framework, to determine the best combination of the three parameters. To achieve that, these have been varied and the data have been analysed multiple times. Twelve combination were chosen and they are listed in Tab. 4.2. The variation of the voltage threshold affects the total number of pulses, because any peak below V_T is neglected. The five values employed are all well above the electronic noise, which is of the order of the millivolt.

The ratio between *events* and *noises* is rather governed by the other two parameters, the number of PMTs fired and the rejection time window. Respectively four and five

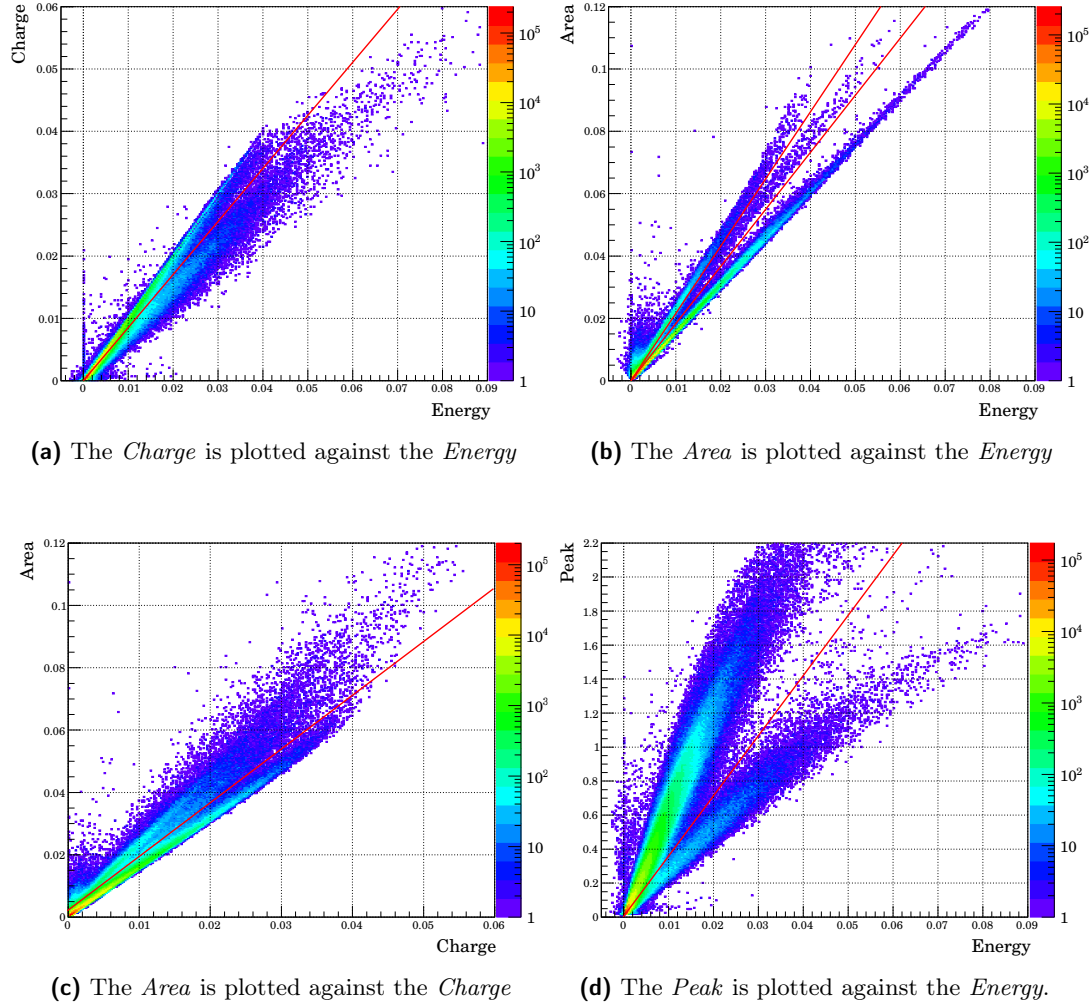
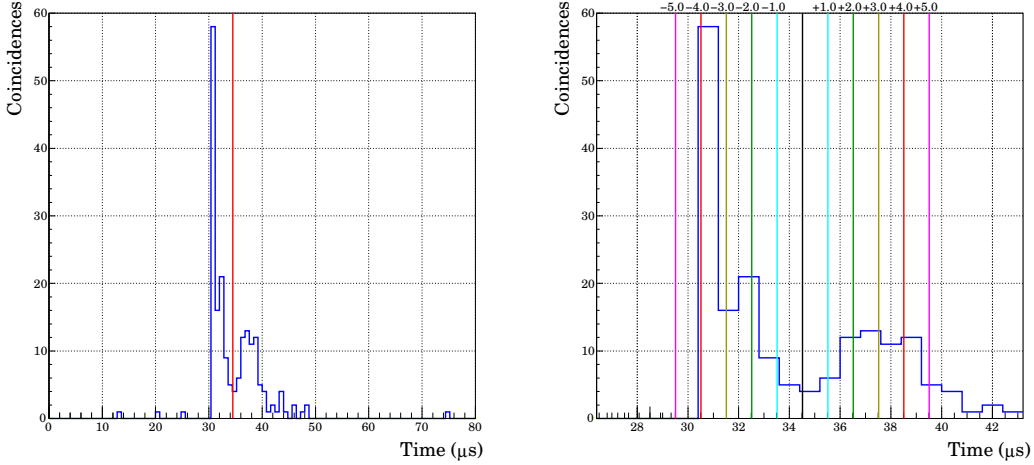


Figure 4.6: Correlation plots among the three integral quantities. The red lines isolate areas with different correlation, likely due to different widths of the pulses. This fact is emphasised in the right-bottom plot: pulses with the same peak height have different energies, and vice versa.



(a) The red line marks the weighted average of the coincidences, which is $34.51\ \mu\text{s}$ in this example. (b) The coloured lines mark the five time window for noise rejection, Δ_T in μs , listed in Tab. 4.2.

Figure 4.7: Both plots show the same histogram, filled with the *Start* time of each pulse belonging to the same trigger. An high multiplicity event is found near $31\ \mu\text{s}$. In this particular case, the time distribution of the signals is quite long: the light in the tank lasts for about twenty microseconds.

values were picked for these parameters. The increase of N_{PMT} restricts the number of *events*, as suggested by Fig. 4.8 where the multileplicity of the events is plotted. This values is indeed closely related to the number of PMTs hit in an interaction. The rise in the frequency, near the end of the x-axis, is likely due to high multileplicity cosmic muon events. The time allowance of the *event* definition was also studied, varying the Δ_T parameter. Understanding the relevance of belated photons, possibly given by reflection inside the tank, is decisive for developing a correct analysis framework. The selected intervals are illustrated in Fig. b of 4.7.

The processed data sets present therefore different number of pulses and different proportion between events and noises. These quantities are summarised in Tab. 4.3, for the Cosmic run, and in Tab. 4.4, for the Beam run. The effects of the different combination of the analysis parameters can be also appreciated by looking at the average pulse shape. As an example, in Fig. 4.9 the average pulses of both the Cosmic and the Beam run are selected from four data sets. The shape of the pulses basically doesn't change, as opposed to the size and the proportion between event and noise, which are sensitive to the three parameters, V_T , N_{PMT} , and Δ_T . The other eight data sets present similar variations as the ones in Fig. 4.9, but with appropriate intensity.

4.4 Data size reduction

A zero-suppression method is planned to be implemented in the data acquisition system for the next stages of ANNIE. As a matter of fact, most of the digitised time window from the VME cards is of no use with respect to the event reconstruction. This can also be easily understood thanks to the Time column in Tab. 4.3 and Tab. 4.4. Taking advantage of circular memory, this technique basically saves a narrower buffer every time an arbitrary voltage threshold is reached. Only individual signals are stored, avoiding long-term memory wasting.

The developed pulse analysis is comparable to the zero-suppression method, even though the signal selection is done after the data acquisition. The outcome is similar:

Label	V_T (V)	N_{PMT}	Δ_T (μ s)
C	0.02	10	4.0
V_{00}	0.005	10	4.0
V_{01}	0.01	10	4.0
V_{05}	0.05	10	4.0
V_{10}	0.10	10	4.0
N_{15}	0.02	15	4.0
N_{30}	0.02	30	4.0
N_{50}	0.02	50	4.0
Δ_{50}	0.02	10	5.0
Δ_{30}	0.02	10	3.0
Δ_{20}	0.02	10	2.0
Δ_{10}	0.02	10	1.0

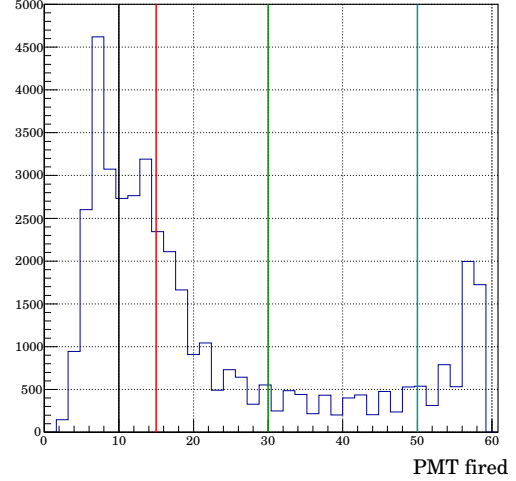


Table 4.2: The combination of the employed thresholds. The first one, in bold letters, is common to each subset.

Figure 4.8: Frequency of the number of PMTs hit in an event.

Label	Total	Event	Noise	Time %	Event %	ENR
C	1,869,473	396,136	1,473,337	8.593	21.190	0.269
V_{00}	3,991,618	718,487	3,273,132	18.349	18.000	0.220
V_{01}	3,199,707	564,810	2,634,897	14.708	17.652	0.214
V_{05}	546,497	252,326	294,171	2.512	46.172	0.858
V_{10}	342,258	200,120	142,138	1.573	58.471	1.408
N_{15}	1,865,579	361,398	1,504,181	8.576	19.312	0.240
N_{30}	1,859,539	305,447	1,554,092	8.548	16.426	0.197
N_{50}	1,850,590	29,622	1,820,968	8.507	1.601	0.016
Δ_{50}	1,869,473	398,012	1,471,461	8.593	21.290	0.270
Δ_{30}	1,869,473	394,194	1,475,279	8.593	21.086	0.267
Δ_{20}	1,869,473	389,014	1,480,459	8.593	20.809	0.263
Δ_{10}	1,869,473	369,047	1,500,426	8.593	19.741	0.246

Table 4.3: Number of pulses in the Cosmic run. The Time column is the percentage of the number of Events times 0.8 μ s with respect to the total time of the run; Event is the ratio between event and the total number of pulses; Event to Noise Ratio (ENR) is the ratio between Event an Noise number.

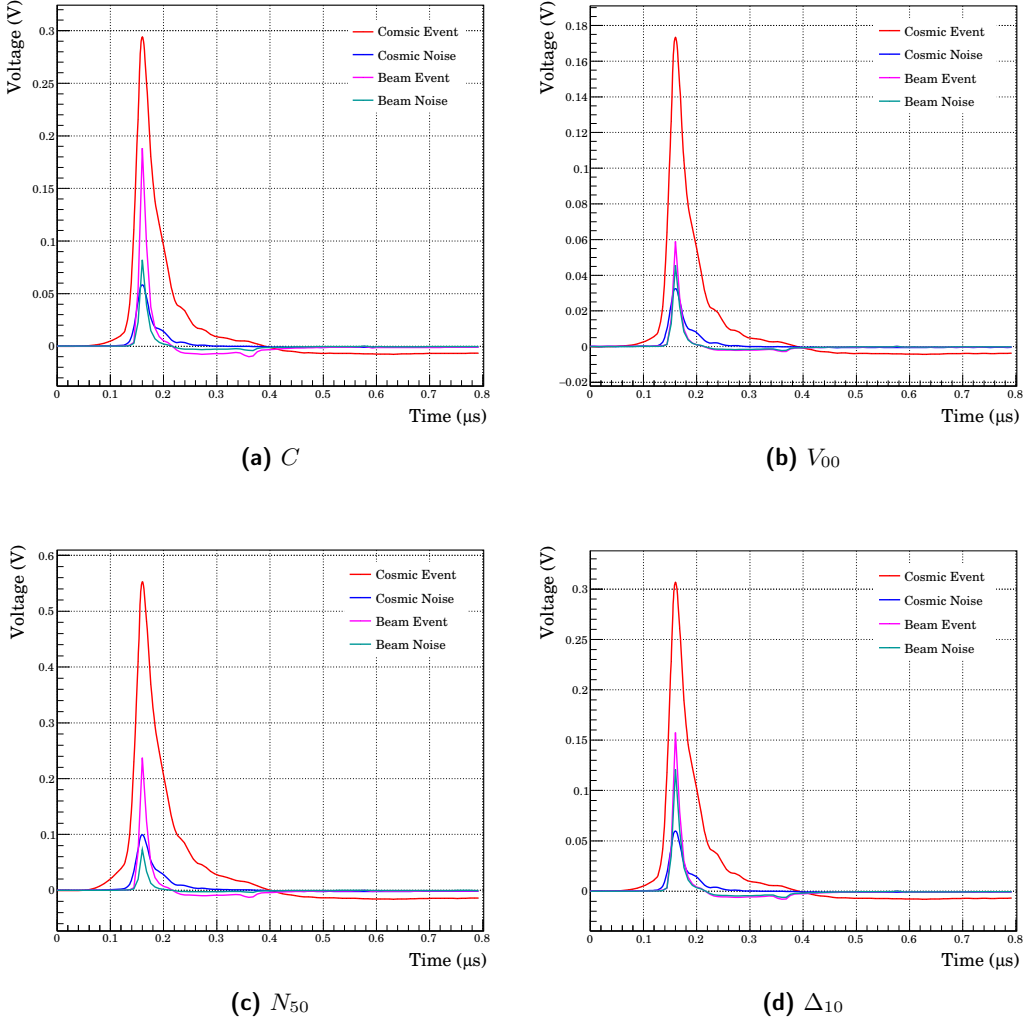


Figure 4.9: Average pulse for Cosmic and Beam's events and noises from four different data sets: C , V_{00} , N_{50} , Δ_{10} . The shapes are all similar, even though their size changes. The proportion between peak heights imply that the Beam data are more influenced by the variation of the parameters.

Label	Total	Event	Noise	Time %	Event %	ENR
C	5,023,868	2,338,273	2,685,595	19.996	46.543	0.871
V_{00}	16,459,218	4,157,391	12,301,827	65.510	25.259	0.338
V_{01}	12,203,561	3,579,758	8,623,803	48.572	29.332	0.415
V_{05}	2,128,895	1,476,111	652,784	8.473	69.337	2.261
V_{10}	1,391,752	1,079,800	311,952	5.539	77.586	3.461
N_{15}	4,881,223	2,643,880	2,237,343	19.428	54.164	1.182
N_{30}	4,743,670	2,026,100	2,717,570	18.880	41.508	0.746
N_{50}	4,616,384	1,581,197	3,035,187	18.374	34.252	0.521
Δ_{50}	5,023,868	2,470,090	2,553,778	19.996	49.167	0.967
Δ_{30}	5,023,868	2,197,769	2,826,099	19.996	43.747	0.778
Δ_{20}	5,023,868	1,820,035	3,203,833	19.996	36.228	0.568
Δ_{10}	5,023,868	1,459,720	3,564,148	19.996	29.057	0.410

Table 4.4: Number of pulses in the Beam run. The Time column is the percentage of the number of Events times $0.8 \mu\text{s}$ with respect to the total time of the run; Event is the ratio between event and the total number of pulses; Event to Noise Ratio (ENR) is the ratio between Event and Noise number.

Label	Cosmics		Beam	
	Data size (MB)	Ratio %	Data size (MB)	Ratio %
C	329.331	0.310	675.355	0.886
V_{00}	621.029	0.585	1779.345	2.333
V_{01}	510.056	0.481	1384.335	1.815
V_{05}	121.439	0.114	351.355	0.461
V_{10}	91.656	0.086	249.068	0.327
N_{15}	326.970	0.308	669.110	0.877
N_{30}	321.029	0.302	646.297	0.848
N_{50}	318.970	0.301	631.707	0.828
Δ_{50}	320.291	0.302	678.463	0.890
Δ_{30}	321.040	0.302	675.090	0.885
Δ_{20}	321.896	0.303	679.243	0.891
Δ_{10}	320.299	0.302	666.223	0.874

Table 4.5: Data sizes of the analysed data sets. The *ratio* columns present the ratio between the final data size and the original size of the post-processed files, listed in Tab. 4.1.

the unnecessary information are nullified. It is easy to appreciate the benefits derived from this technique, just by looking at Tab. 4.5. The memory size of the analysed files varies from 0.3 % to 3 %, with minima of the order of 0.1 %, depending on the choice of the parameters. The results in Tab. 4.5 indicates that V_T has the strongest influence on the final data size, as expected. The other two parameters, instead, are not of great concern, since they don't impact on the effective number of the pulses. Combined with the post-processor software, which reduces the raw data files to almost a quarter of the initial size, the zero-suppression method could achieve a compression factor of about four-hundred.

Chapter 5

Data analysis results

Some data analysis results are presented in this chapter, regarding either the method developed or simulation. The plots reported here were realised using the *C* data set.

5.1 Cosmic muons

High energy particles, mainly originated outside the Solar System and thus called *Cosmic Rays*, impact on the Earth's atmosphere and producing mesons, which in turn generate secondary particle shower by decaying. The primary particles are about 99 % made of ionised nuclei (whose 86 % made of protons, 12.7 % of helium nuclei, and 1.3 % of heavier nuclei), while the remaining 1 % is mostly composed by electrons cite[theodorsson]. The intensity of the nucleons in the energy range from several GeV to somewhat beyond 100 TeV is given approximately by

$$I_N(E) \simeq 1.8 \times 10^4 \left(\frac{E}{1 \text{ GeV}} \right)^{-\alpha} \frac{\text{nucleons}}{\text{m}^2 \text{ s sr GeV}}, \quad (5.1)$$

where E is the energy-per-nucleon, including rest mass energy, and $\alpha = \gamma + 1 = 2.7$ is the differential spectral index of the cosmic ray flux, with γ the integral spectral index.

Many are the secondary products reaching the sea level, among which muons, neutrinos, nucleons, and electrons. The first two, muons and neutrinos, derive from the decay chain of charged mesons, while electrons and photons originate in decays of neutral mesons. As Fig. 5.1 shows, muons are the most numerous charged particles at sea level. Their direction of propagation is the same as that of their parents pions and in average they receive close to 80 % of their parent's energy. They are very penetrating as their nuclear interaction cross section is only about $2 \times 10^{-29} \text{ cm}^2$ (or two microbarns). The energy loss to ionisation is at a fairly constant rate of about 2 MeV per g/cm². Given that the vertical depth of the atmosphere is about 1000 g/cm², muons will lose about two GeV before reaching the ground. The mean energy of muons at sea level is about four GeV; therefore the mean energy at creation, typically fifteen kilometres high, is probably near six GeV. Their energy and angular distribution reflect a convolution of the production spectrum, energy loss in the atmosphere, and decay. The integral intensity of vertical muons above 1 GeV/c at sea level is nearly

$$I_{\text{MSL}} \simeq 70 \text{ m}^{-2} \text{s}^{-1} \text{sr}^{-1}, \quad (5.2)$$

for horizontal detectors. The overall angular distribution of muons at the ground is somehow:

$$\frac{dN}{dA\Omega dt} \propto \cos^k \theta, \quad (5.3)$$

where $k \simeq 2$. There is no expected dependence on the azimuthal angle ϕ , while the above relation is not expected to be valid for $\theta > 80^\circ$ where the Earth's curvature becomes

an important consideration. However, integrating with respect to the solid angle, with a zenith angle $0 < \theta < \pi/2$, it is possible to estimate the rate of muons per area unit:

$$I_0 = 2\pi I_{\text{MSL}} \int_0^{\pi/2} \cos^2 \theta \sin \theta d\theta = \frac{2}{3}\pi I_{\text{MSL}} \simeq 147 \text{ m}^{-2}\text{Hz}, \quad (5.4)$$

With the beam off, only cosmic rays leave a trace in the ANNIE detector. From Eq. 1.28, every muon with an energy $E \gtrsim 160$ MeV can produce Cherenkov radiation, given that the refractive index of water is $n = 1.33$ and the muon mass is 105 MeV¹. Since the average energy of the muon reaching the ground is well above the Cherenkov threshold, the nominal flux at sea level can be used to evaluate the cosmic background rate. The water tank is placed eight meters below the surface, and it fits the hall's walls, hence only the top area of the tank (slightly more than 7 m²) could be taken in consideration. A rough estimation suggests that the rate of muons reaching the detector is

$$I \simeq (7 I_0) \text{ m}^2 \simeq 1036 \text{ Hz}. \quad (5.5)$$

This rate can be estimated, counting the Events found by the analysis algorithm. For a more realistic calculation, events that show coincidences with the Veto or the MRD are discarded. The Beam run could also be used for this evaluation, for instance exploiting the fact that beam events are limited to the first half of the 80 μs buffer. However either the Veto or the MRD signals are on most of the time, being the trigger synchronised with the beam, therefore the tally is not feasible, but with the Cosmic run. The rate is the result of the division between the number of events and the time of the considered triggers. The number of pulses in this kind of event are also counted in order to find the average number of pulses in a muon event. The measured rate is compared to the theoretical value in Eq. 5.5: the outcome ratio is a combination of the detector's efficiency (geometry and photodetector quantum efficiency), as well as the validity of the data analysis algorithm. In Tab. 5.1 the results are shown. The Δ_T parameter doesn't influence the count of the cosmic muons as much as the other parameters do. The cut in the PMT number selects the most energetic events, while the voltage threshold remove a lot of low energy pulses, instead.

5.2 Centre of interaction

Simple event reconstruction was undertaken with preliminary data, although the spatial resolution of the present photodetector array is limited. The idea is to analyse the pattern

¹The muon mass is known with an accuracy of order 10^{-8} . According to the PDG, $m_\mu = 105.658,371,5 \pm 0.000,003,5$ MeV.

Label	Trigger	Event	Pulse	Mean pulse	Rate (Hz)	Ratio (%)
C	217,530	8078	330,111	40.865	464.189	44.806
V_{00}	225,412	14,210	635,602	44.729	788.002	76.064
V_{01}	222,539	11,362	488,371	42.983	638.203	61.603
V_{05}	111,640	5590	229,456	41.048	625.896	60.415
V_{10}	59,690	5056	195,273	38.622	1058.804	102.201
N_{15}	216,157	6692	296,674	44.333	386.987	37.354
N_{30}	214,474	4980	247,709	49.741	290.245	28.016
N_{50}	210,007	458	25,212	55.048	27.261	2.631
Δ_{50}	217,506	8079	331,452	41.026	464.298	44.816
Δ_{30}	217,574	8095	328,772	40.614	465.072	44.891
Δ_{20}	217,634	8122	324,632	39.969	466.494	45.028
Δ_{10}	217,964	8135	307,014	37.740	466.533	45.032

Table 5.1: Cosmic muon rate, estimated using the analysed Cosmic data. For evaluating the rate, the total time is given by the number of triggers time $80 \mu\text{s}$. The last column is the ratio between the measured rate with the theoretical one, in Eq. 5.5.

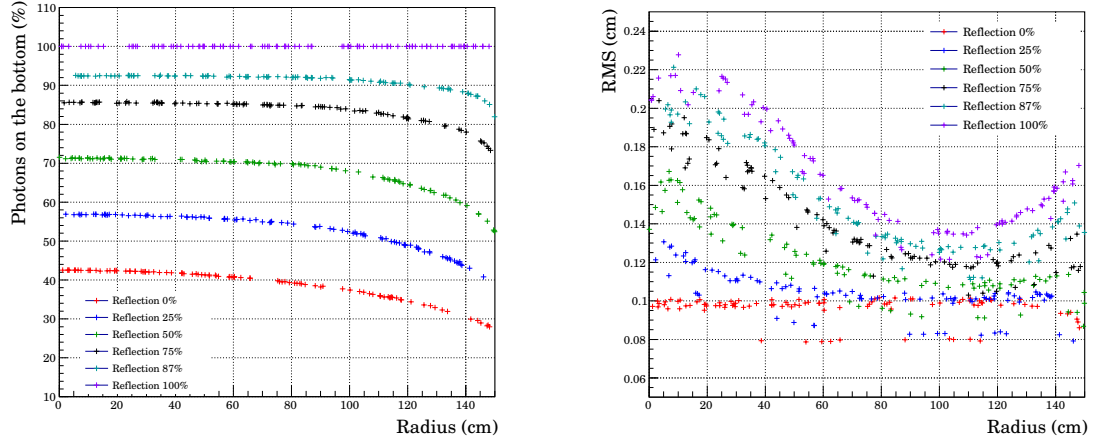
of the photon deposited on the PMTs, in order to infer the nature of the interaction which generated the Cherenkov radiation. As a first step, the Cosmic run has been taken in consideration, because it doesn't contain beam events, but muon ones; the validity of the selection method has been also tested, with also the help of an easy Monte Carlo simulation (see App. B).

For the sake of simplicity, the simulation generates only vertical muons, with $\beta = 1$, and the propagation of Cherenkov photons inside ANNIE's tank is reproduced. Muons don't enter vertically in the tank, but it can be considered as a strong assumption, taking into account the geometry of the hall of the experiment. The distribution of the photons on the bottom of the detector, with respect to the position of the entering muon and the reflection of the inner walls, is thus studied. Five significant reflection percentages were chosen (0 %, 25 %, 50 %, 75 %, 100 %), in addition to the value given by the vendor (87 %). The percentage of photons reaching the bottom of the cylinder is shown in Fig. 5.2 for each reflection values. This plot can help in the pattern reconstruction of collected data, in that the role of the walls has not been determined yet.

The simulation also shows that the position of the muon is strongly correlated with the spot of highest gathering of photons. A linear fit was computed and the results are listed in Tab. 5.2. This suggests that the position where most of the photons are deposited should be used when handling real data. On the other hand, the relation with the barycenter of the light pattern is less straightforward and depends on the reflection of the walls, as shown in Fig. 5.3, even though the behaviour of the dispersion (RMS) of the photons is easier to interpret.

Regarding the data collected, the space is discretised, because of the physical limitation of the photomultipliers. For this reason, using the position of the most frequent hit PMT does not provide any further information. The average position, \hat{d} , of the PMTs with respect to the centre of the water tank, weighted by the overall energy collected², is employed, instead, and is plotted versus the average energy, \hat{E} , per pulse. In Fig. 5.4, the plot for both noise and event signals in data set C are shown. A far resemblance can be seen with the simulation results. A high-frequency region is visible in the noise plot, which misses from the event one. This area can be roughly separated with the following formula:

²The definition of *energy* is explained in section ref.



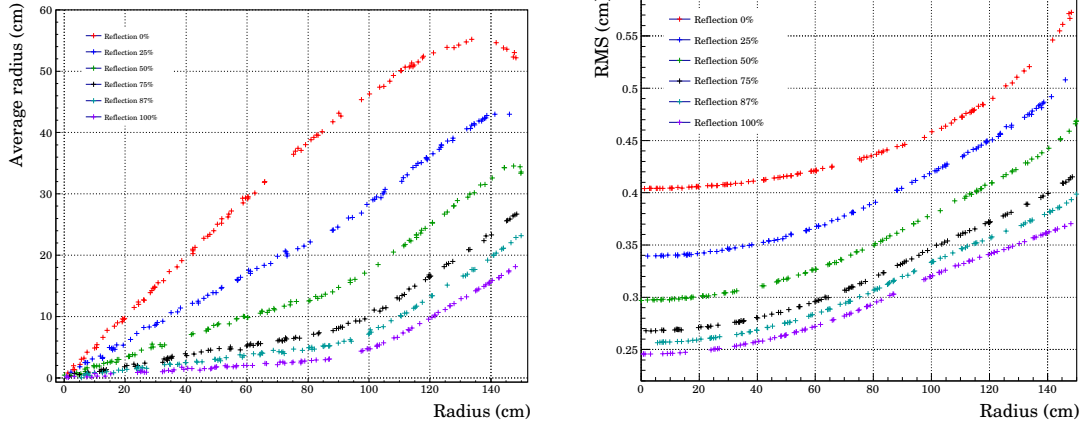
(a) As expected, all photons reach the bottom when the reflection is 100 %. If the walls fully absorbe, about 40 % of the photons hit the base of the tank.

(b) Dispersion of hte photon on the bottom of the tank. If the walls fully absorbe, the photons are evenly distributed, otherwise the minium dispersion is reached at about one metre from the centre.

Figure 5.2: Photons deposited on the bottom of the water tank, with different values of wall reflection. The x-axes is the distance of the muon with respect to the center of the tank.

Reflection	$\rho_{a,b}$	a (cm)	b
0 %	-0.837	0.0 ± 0.2	1.001 ± 0.002
25 %	-0.866	0.2 ± 0.2	0.998 ± 0.002
50 %	-0.839	0.3 ± 0.2	0.998 ± 0.002
75 %	-0.862	0.0 ± 0.2	1.000 ± 0.002
87 %	-0.871	0.2 ± 0.2	0.998 ± 0.002
100 %	-0.878	0.1 ± 0.2	0.999 ± 0.002

Table 5.2: Fit result of the correlation of the plot max hit vs muon position. The function $y = a + bx$ was employed. The correlation is independant of the value of reflection.



(a) Average distance of the deposited photons. The correlation is basically liner if the walls absorbe all the light.

(b) Deviation of the distance of the deposited photons from the average. The relation is somehow parabolic within one metre from the centre of the tank. In all cases, the smallest dispersion occur for coaxial muons.

Figure 5.3: Correlation plots versus the distance of the muon with respect to the centre of the cylinder.

$$\hat{E} = 10^{-3} - 2 \times 10^{-6} \hat{d}, \quad (5.6)$$

that is supposed to count type I errors of the selection algorithm. The results are listed in Tab. 5.3.

5.3 Beam events

Changing the analysis software parameters, the proportion between *signals* and *noises* varies consequently. With the help of the beam run an evaluation on the strength of the rejection method can be undertaken, selecting beam related event only. As illustrated in Fig. 5.6, the beam events happen from 10.2 to 11.8 microseconds. The spill lasts indeed 1.6 μs . To make sure only beam-related processes are counted, signals which have a correspектив Veto signals are discarded, while only the pulses with both layers of the MRD on are selected. As a consequence, these restrictions permit to consider interactions happening inside the water volume and producing outgoing charged particles, i.e. mostly CCQE interaction. In Tab- 5.4, the results.

5.4 Muon decay

As explained in section ref, the dominant decay channel of the muon is the *Michel decay*, which is reported in Eq. 1.37 and 1.38. The muon lifetime is a well known physical quantity and measured to be on average

$$\tau_{\text{avg}} = (2.196,981,1 \pm 0.000,002,2) \mu. \quad (5.7)$$

There is basically no discrepancy between μ^- and μ^+ lifetime, respectively τ_{μ^-} and τ_{μ^+} . It has been measured that

$$\frac{\tau_{\mu^+}}{\tau_{\mu^-}} = 1.000,024 \pm 0.000,078, \quad (5.8)$$

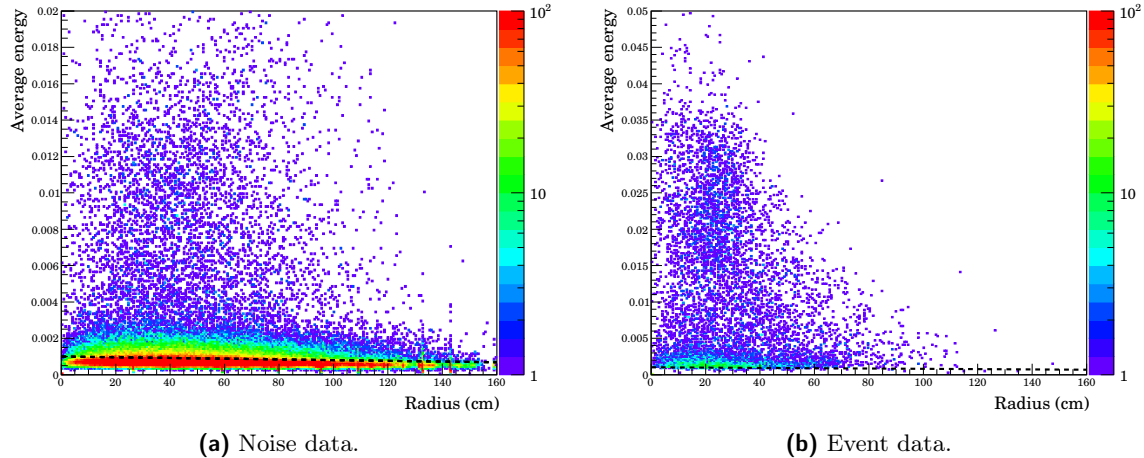


Figure 5.4: Average energy distribution versus the barycenter of the PMTs. The black dashed line is used to reject false positive events and corresponds to Eq. 5.6.

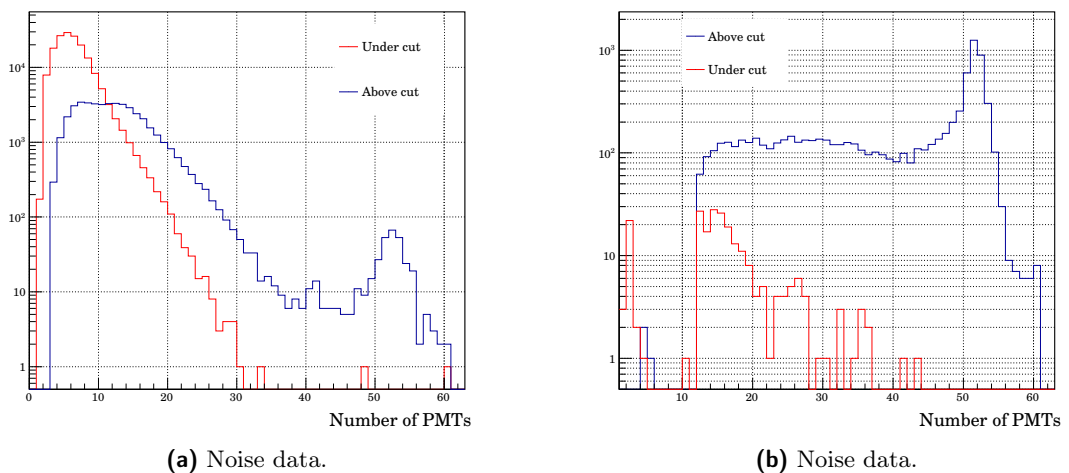
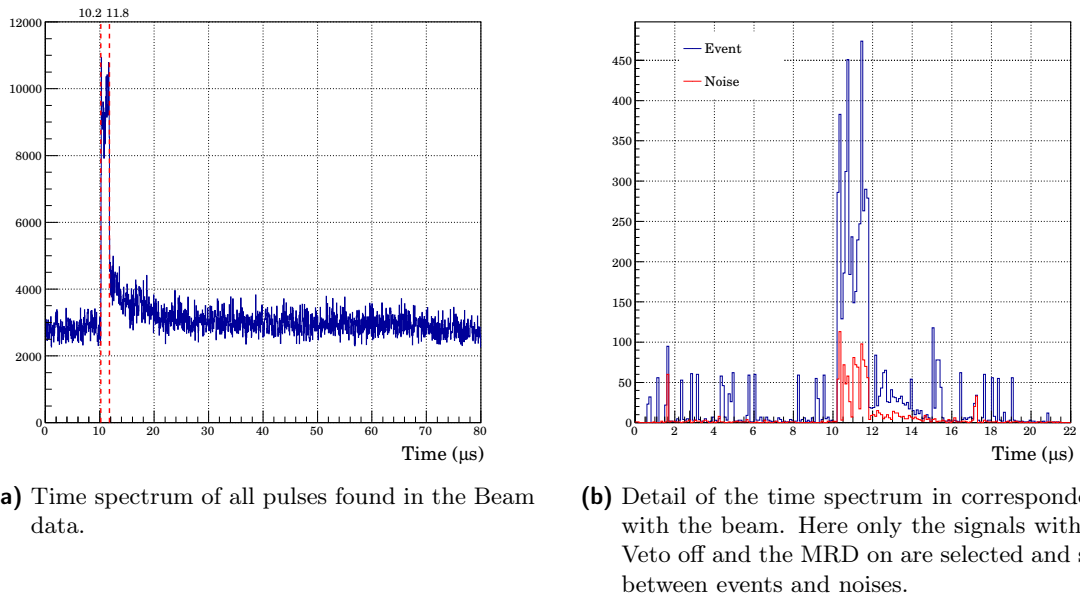


Figure 5.5: Frequency plot of the number of PMT hit. The spectrum is split in the two subset given by the cut rule in Eq. 5.6.

Label	Event				Noise			
	Total	Under	Above	Ratio (%)	Total	Under	Above	Ratio (%)
C	8078	224	7854	2.773	209,452	164,787	44,665	21.325
V_{00}	14,210	5839	8371	41.091	211,202	197,338	13,864	6.564
V_{01}	11,362	2824	8537	24.855	211,177	189,744	21,433	10.149
V_{05}	5590	3	5587	0.054	106,050	63,881	42,169	39.763
V_{10}	5056	1	5055	0.020	59,690	31,404	23,230	38.918
N_{15}	6692	84	6608	1.255	209,465	163,808	45,657	21.797
N_{30}	4980	28	4952	0.562	209,494	162,540	46,954	22.413
N_{50}	458	1	457	0.218	209,549	158,370	51,179	24.432
Δ_{50}	8079	230	7846	2.847	209,427	163,232	46,327	22.121
Δ_{30}	8095	232	7862	2.866	209,479	164,312	45,200	21.577
Δ_{20}	8122	260	7863	3.201	209,512	164,642	44,837	21.401
Δ_{10}	8135	289	7849	3.553	209,559	165,821	44,606	21.287

Table 5.3: False positive count.**Figure 5.6:** Time spectrum realised using the *Start* of the pulses of the Beam run.

Label	Total	Event	Noise	Ratio (%)
C	5176	4254	922	82.187
V_{00}	6480	4232	2248	65.309
V_{01}	6527	4583	1944	70.216
V_{05}	1034	1033	1	99.903
V_{10}	0	0	0	N/A
N_{15}	5070	4179	891	82.426
N_{30}	4998	4038	960	80.792
N_{50}	4724	3780	1398	80.017
Δ_{50}	5378	4505	873	83.767
Δ_{30}	5178	4272	906	82.503
Δ_{20}	5148	4095	1053	79.545
Δ_{10}	5178	3780	1398	73.001

Table 5.4: Count of pure beam events. The last column is the ratio of Events with respect to the totality of pulses.

and

$$\frac{\tau_{\mu^+} - \tau_{\mu^-}}{\tau_{\text{avg}}} = (2 \pm 8) \times 10^{-5}. \quad (5.9)$$

It is possible that a muon, either a cosmic one or produced in a CCQE interaction, decays inside ANNIE's volume, and the daughter electron is ejected with a velocity above the Cherenkov threshold: in this case, the electron can be detected. Measuring the abundance of electrons produced in such way, the muon lifetime can be inferred.

Observing the time spectrum of the Beam run in Fig. 5.7, an exponential tail is found after the beam position, particularly accentuated in the Event signals. The histogram can be fitted with the function:

$$y = N e^{-x/\tau} + c_E. \quad (5.10)$$

On the contrary, the Noise signals show a gaussian distribution right after the beam occurrence, which can be fitted with:

$$y = A \exp\left(-\frac{(x - \mu)^2}{2\sigma^2}\right) + c_N. \quad (5.11)$$

Therefore the spectrum, realised without distinguishing between Events and Noises, may be fitted with the sum of Eq. 5.10 and Eq. 5.11:

$$y = N_T e^{-x/\tau_T} + A_T \exp\left(-\frac{(x - \mu_T)^2}{2\sigma_T^2}\right) + c_T. \quad (5.12)$$

Regarding Eq. 5.10, the τ parameter should be compatible with the muon lifetime, while the gaussian peak of Eq. 5.11 is **I don't know yet**. In Tab. 5.5, the fitted values of these two parameters are reported. The fit results in their entirety are reviewed in App. C.

The most compatible values of the measured lifetime with τ_{avg} are given by V_{05} , V_{10} , Δ_{20} , and Δ_{10} , likely because in these data sets the time correlation between pulses is stricter and other effects, such as reflection, are neglected.

5.5 Neutron yield

The PMT mounted on top of the NCV is able to detect the scintillation light and is analysed just as the other detectors, but discrimination process between event and signal

Label	Event	Noise	Total	
	τ (μ s)	μ (μ s)	τ_T (μ s)	μ_T (μ s)
C	2.94 ± 0.06	17.66 ± 0.05	3.2 ± 0.1	18.13 ± 0.05
V_{00}	4.25 ± 0.04	17.85 ± 0.03	4.29 ± 0.09	17.76 ± 0.02
V_{01}	4.02 ± 0.03	17.73 ± 0.03	4.66 ± 0.09	17.78 ± 0.03
V_{05}	2.8 ± 0.2	18.16 ± 0.05	1.8 ± 0.2	18.10 ± 0.09
V_{10}	2.16 ± 0.05	18.22 ± 0.06	9.3 ± 0.7	17.397 ± 0.002
N_{15}	3.06 ± 0.07	17.61 ± 0.04	4.7 ± 0.2	18.24 ± 0.06
N_{30}	3.07 ± 0.09	17.56 ± 0.06	3.4 ± 0.1	18.26 ± 0.05
N_{50}	3.3 ± 0.1	17.76 ± 0.07	5.31 ± 0.08	17.81 ± 0.02
Δ_{50}	2.48 ± 0.02	18.03 ± 0.04	3.5 ± 0.1	18.16 ± 0.05
Δ_{30}	2.64 ± 0.07	17.04 ± 0.07	3.8 ± 0.1	18.17 ± 0.05
Δ_{20}	2.07 ± 0.04	17.65 ± 0.06	2.76 ± 0.08	18.03 ± 0.05
Δ_{10}	2.09 ± 0.04	17.60 ± 0.05	3.8 ± 0.1	18.17 ± 0.05

Table 5.5: Fit results of the τ and μ parameter of respectively Eq. 5.10, for Event part of the spectrum, and Eq. 5.11, for the Noise one. The entire spectrum is also fitted, with Eq. 5.12, and the two parameters are inferred.

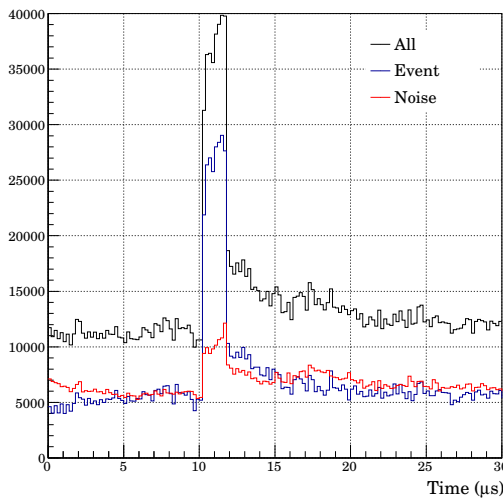


Figure 5.7: The time spectrum of the Beam run has been split, between event (blue) and noise (red) pulses. After the beam position, an exponential tail is visible for the events, while there is a gaussian peak for the noises. The total plot, in black, therefore would present a tail given by the sum of an exponential and a gaussian distribution.

Label	NCV	Mean (μ s)	RMS (μ s)
C	424	26 ± 1	23.6 ± 0.8
V_{00}	1095	25.8 ± 0.7	22.5 ± 0.5
V_{01}	751	26.4 ± 0.8	23.1 ± 0.6
V_{05}	139	26 ± 2	23 ± 1
V_{10}	29	28 ± 4	21 ± 3
N_{15}	414	26 ± 1	23.6 ± 0.8
N_{30}	396	26 ± 1	23.7 ± 0.8
N_{50}	384	26 ± 1	23.9 ± 0.9
Δ_{50}	424	26 ± 1	23.6 ± 0.8
Δ_{30}	424	26 ± 1	23.6 ± 0.8
Δ_{20}	424	26 ± 1	23.6 ± 0.8
Δ_{10}	424	26 ± 1	23.6 ± 0.8

Table 5.6: The pulses acquired from the PMT of the NCV were contend. The arithmetic average of their time position with respect to the time occurrence of the beam and their deviation from the mean are also calculated.

is skipped. The number of pulses extracted from the Beam run is summarised in Tab. 5.6, and the mean of their time delay with respect to the beam position is computed to be around $26 \mu\text{s}$, in agreement with the distinctive time of neutron capture. However, this result is not robust because the statistic is quite low and the dispersion of the measures is very high, as indicated by the standard deviations. The average shape of the signals produced by the scintillator is illustrated in Fig. 5.8 and compared with the event and the noise average pulse.

5.6 First MRD data

The spectrum in Fig. 5.9 is the first run taken with the MRD DAQ. It corresponds to $(345,198.25 \pm 0.03)$ s of acquisition³, or roughly speaking four days. As explained in section ref, only the second and the third layers are instrumented in Phase I. The resolution of the TDCs is set to the maximum value available (4.0 ns), therefore the time window is $4.088 \mu\text{s}$ long. This suffices the aim of this preliminary test, i.e. to observe the beam by muon detection. The events collected are 64,298, resulting in nearly 0.2 per seconds on average. The spectrum exhibits an augmentation, since it rises to an average value of (86.3 ± 0.5) from (45.6 ± 0.4) and (48.9 ± 0.4) respectively before and after it. These last two means are far from being compatible with the middle one, hence the contour of the spectrum can be implied to the presence of the beam. The increase happens from $1.124 \mu\text{s}$ to $2.648 \mu\text{s}$ in the TDC time window: the beam is $1.524 \mu\text{s}$ wide, in agreement with the effective total duration of the spill, which is $1.6 \mu\text{s}$.

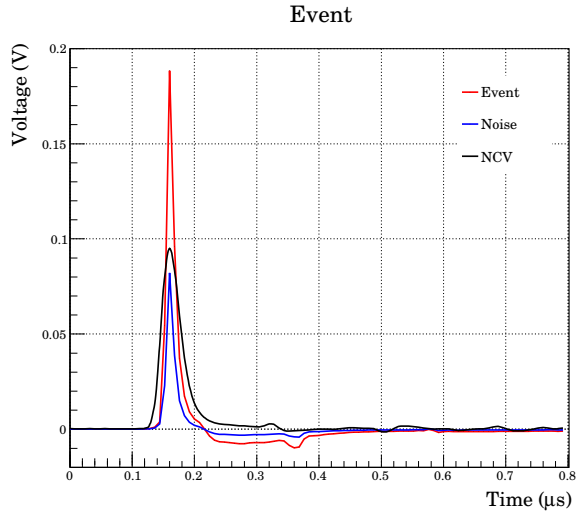


Figure 5.8: Average pulses of the Beam run in comparison with the pulses collected from the NCV.

³The error is given by the accuracy of the NTP server, which is about thirty milliseconds.

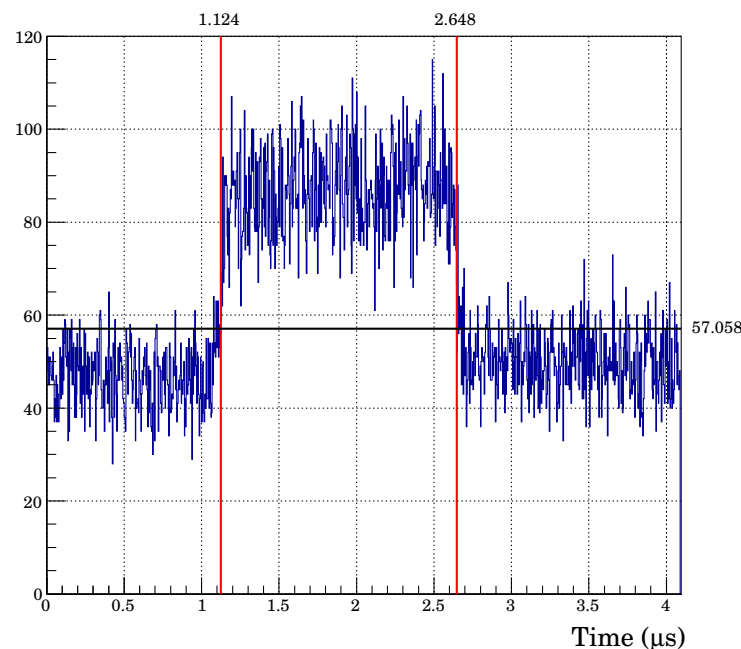


Figure 5.9: The time spectrum of the Beam run, seen by the MRD. The black line represents the arithmetic mean of the frequencies (y-axis), estimated to be 57.1 ± 0.2 . The red lines at 1.124 and 2.648 are respectively the last and first intersection of the black line with the spectrum, in correspondence of the beam.

Chapter 6

Conclusions

Physics sucks.

Appendix A

Booster Neutrino Beam

Arxiv 1311.5958v1. Fermilab has two major neutrino beamlines: the Neutrino Main Injector (NuMI) and the Booster Neutrino Beam (BNB). The energy range of these two neutrino sources on-axis is in the GeV range, which is too high to satisfy the condition for dominance of coherent scattering. The BNB source has substantial advantages over the NuMI beam source owing to suppressed kaon production from the relatively low energy 8 GeV proton beam on the target ref. Therefore, pion decay and subsequent muon decay processes are the dominant sources of neutrinos. At the far-off-axis area, the detector can be placed close enough to the target to gain a large increase in neutrino flux due to the larger solid angle acceptance. Moreover, the far-off-axis ($> 45^\circ$) of the BNB produces more defined neutrinos, with energies below 50 MeV.

The Booster is a 474-meter-circumference synchrotron operating at 15 Hz. The beam is extracted into the BNB using a fast-rising kicker that extracts all of the particles in a single turn: protons from the Fermilab LINAC are injected at 400 MeV and accelerated to 8 GeV kinetic energy, or 8.89 GeV/c momentum by the Booster. It has a harmonic number of 84, but the beam is structured in a series of 81 proton bunches each 2 ns wide and 19 ns apart. Upon leaving the Booster, the proton beam is transported through a lattice of focusing and defocusing quadrupole (FODO) and dipole magnets. A switch magnet steers the beam to the main injector or to the BNB. The BNB is also a FODO that terminates with a triplet that focuses the beam on the target. The maximum allowable average repetition rate for delivery of protons to the BNB is 5 Hz (with a maximum of 11 pulses in a row at 15 Hz) and 5×10^{12} protons per pulse. The 5 Hz limit is set by the design of the horn and its power supply.

A.1 The target

The target is made of beryllium divided in seven cylindrical sections in a total of 71.1 cm, in length, or about 1.7 inelastic interaction length, and 0.51 cm in radius. The target is contained within a beryllium sleeve 0.9 cm thick with an inner radius of 1.37 cm. Each target slug is supported within the sleeve by three “fins” (also beryllium) which extend radially out from the target to the sleeve. The volume of air within the sleeve is circulated to provide cooling for the target when the beam line is in operation. An exploded view of the various components, with the downstream end of the target on the right, is outlined in Fig. A.1. The choice of Be as the target material was motivated by residual radioactivity issues in the event that the target assembly needed to be replaced, as well as energy loss considerations that allow the air-cooling system to be sufficient. The vacuum of the beam pipe extends to about 150 centimetres upstream of the target, minimizing upstream proton interactions.

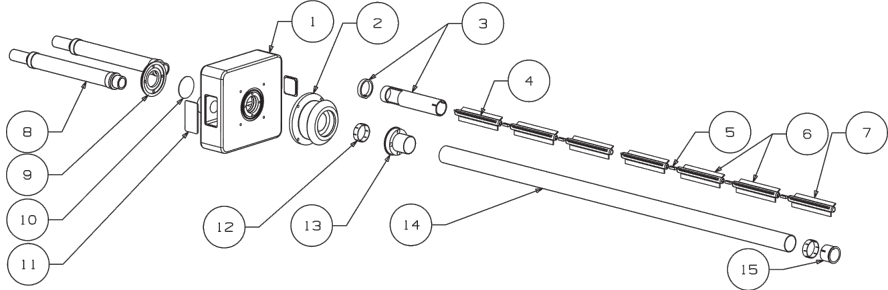


Figure A.1: An exploded view of the beryllium target assembly. 1) target base block; 2) bellow contact system; 3) upstream target slug locator and ring; 4) target slug, upstream; 5) target slug pin; 6) target slug, middle; 7) target slug, downstream; 8) air cool standoff; 9) window flange; 10) beryllium window; 11) base plug; 12) lock ring; 13) outer tube flange; 14) outer tube; 15) onstream target slug locator and gasket.

A.2 The Horn

The horn, shown in Fig. A.2, is a pulsed toroidal electromagnet composed of an aluminum alloy (6061 T6), which surrounds the target. This device bends, sign-selects, and focuses the secondary particles that emerge from the interactions in the beryllium, along the direction pointing to the detector. The current flowing in the horn is a $143 \mu\text{s}$ -long pulse half sinusoid, with a nominal amplitude of 170 kA coinciding with the arrival of the proton beam at the target. The actual operating values are typically 174 kA in both neutrino mode (positive current) and antineutrino mode (negative current), with ± 1 kA variations. In neutrino mode, the flow of current runs along the inner conductor, which folds outwards at a length of 185 cm to return via the outer conducting cylinder of the horn at 30 cm radius. Within the horn cavity, defined by the volume between the outer and inner conducting cylinders, the pulse creates a magnetic field that falls as $1/R$, where R is the distance from the cylindrical symmetry axis of the horn. The largest magnetic field values of 1.5 T are obtained where the inner conductor is narrowest (2.2 cm radius). The “skin effect”, in which the time-varying currents traveling on the surface of the conductor penetrate into the conductor, results in electromagnetic fields within the conductor itself. However, the effects of time-varying fields within the cavity of the horn are found to be negligible. The target assembly is rigidly fixed to the upstream face of the horn, although the target is electrically isolated from its current path.

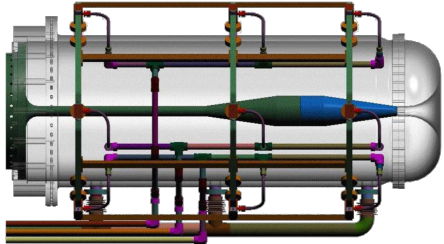


Figure A.2: BNB horn system.

A concrete collimator is located downstream of the target and guides the beam into the decay region. The air-filled cylindrical decay region extends for 45 m, 90 cm radius. The beam stop is made of steel and concrete. The beam of focused, secondary mesons emerging from the target/horn region is further collimated, via passive shielding, and allowed to decay into neutrinos in a cylindrical decay region filled with air at atmospheric pressure, 50 m long and 90 cm in radius. A beam absorber located at the end of the decay region stops the hadronic and muonic component of the beam, and only a pure neutrino beam pointing toward the detector remains, mostly from pion to mu+ nuofmu decays.

A.3 Monitoring

Upstream of the target, the primary proton beam is monitored using four systems:

- two toroids measuring its intensity (protons per pulse);
- beam position monitors (BPM);
- a multiwire chamber, that in combination with the BPMs determines the width and position of the beam;
- a resistive wall monitor (RWM) measuring both the time and intensity of the beam spills.

The number of protons delivered to the BNB target is measured for each proton batch using the toroids located near the target along the beam line. The toroids are continuously calibrated at 5 Hz with their absolute calibrations verified twice a year. The calibrations have shown minimal deviation ($< 0.5\%$). The proton flux measured in the two toroids agree to within 2%, compatible with the expected systematic uncertainties.

The BPMs are split-plate devices that measure the difference of charge induced on two plates. By measuring the change in beam position at several locations without intervening optics, the BPMs are found to be accurate to 0.1 mm. The typical beam alignment and divergence measured by the beam profile monitors located near the target are within 1 mm and 1 mrad of the nominal target center and axis direction, respectively. These parameters are well within the experiment requirements. The multiwire is a wire chamber with 48 horizontal and 48 vertical wires and 0.5 mm pitch. The profile of the beam is measured using the secondary emission induced by the beam on the wires.

The RWM is located upstream of the target to monitor the time and intensity of the proton pulses prior to hitting the target, by measuring the image charge that flows along the vacuum chamber following the beam. The image charge has equal magnitude but opposite sign and in order to measure it, the beam pipe is cut and a resistive gap is inserted. Depending on the beam velocity, the image charge will lag behind and be spread out along its path. The ultimate bandwidth of such a detector is limited by this spreading of the electric field lines between the beam and the inside walls of the beam pipe. Various ferrite cores are used to force the image current through the resistive gap rather than allowing it to flow through other conducting paths.

Appendix B

Monte Carlo simulation

A simple Monte Carlo simulation was developed in order to help study the Cherenkov radiation production to the passage of a charged particle. The minimal model to study the distribution of the photon on the floor of the tank and the role of the walls is implemented. This considers only vertical muons with $\beta = 1$, and both scattering with nucleons and the related energy loss are ignored. A uniform Mersenne Twister (MT) generator¹ defines the position of the muon entering in the tank. Its propagation is stopped every 0.1 cm and a handful of photons is generated isotropically, using the same PRNG. The number of photons at each step is fixed a priori and Eq. 2.2 gives:

$$N_\gamma \simeq 27, \quad (\text{B.1})$$

with $L = 0.1$ cm, θ_C maximum, and λ interval from 300 to 500 nm. As soon as all the photons end their route, the muon is moved and the process is repeated again, until even the charged lepton hits the bottom.

The track of the gammas is precisely defined by its origin, the direction it is emitted, and the reflection coefficient of the PVC walls, because they travel in straight lines. With elementary geometry, it is easy to calculate the track of the photons. Since the muon travels at ultrarelativistic speed, the wavefront of the photons has the maximum angle allowed by the Cherenkov effect, which in water is $\theta_C = 41^\circ$. The muon and the photons tracks are exemplified in Fig. B.1. The impact of the walls is managed by the same MT generator.

For every reflection coefficient, hundred muons are simulated and some illustrative results are shown in Fig. B.2. Being the tank 4 metres tall, the muon makes 4000 steps, hence 108,000 photons are generated everytime. Obviously only when the walls entirely reflects (100 % reflection), all the photons reach the bottom. Despite its simplicity, this model is capable of producing interesting results.

¹The Mersenne Twister is a pseudorandom number generator (PRNG) and its name is due to the fact that its period length is a Mersenne prime. The version used employs the Mersenne prime $2^{219937} - 1$.

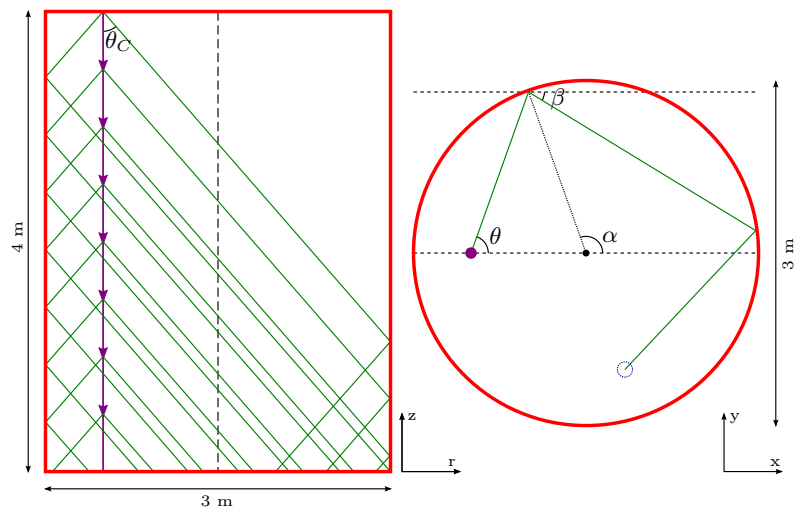


Figure B.1: Track of the incoming muon (in purple) and the emitted photons (in green). On the left, the side view underlines the angle of the wavefront with respect to the z-axis, θ_C . On the right, the top view shows the xy-plane reflections of the photon. Since θ and α are known, the angle after the reflection is $\beta = \pi - \theta + 2\alpha$.

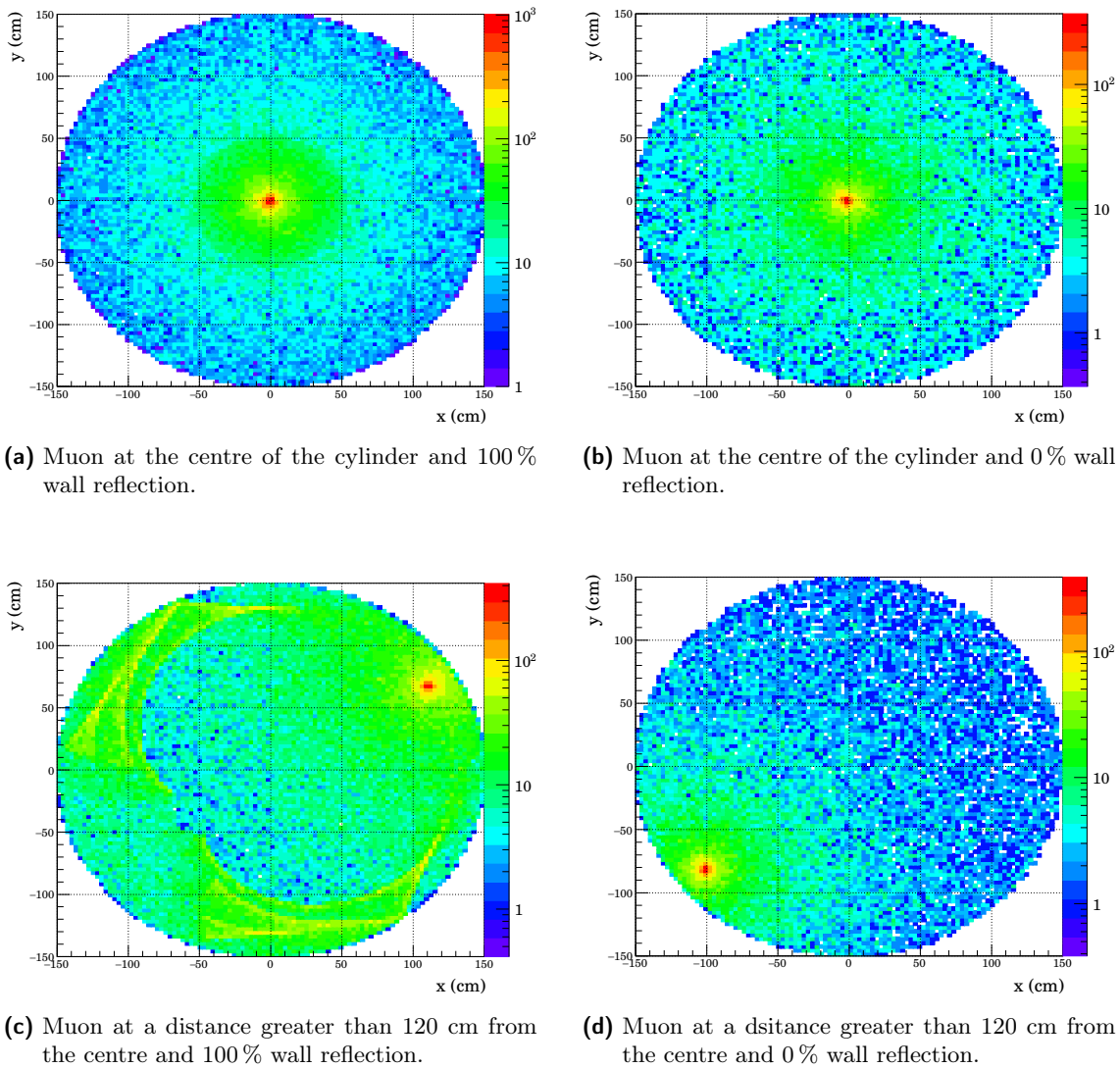


Figure B.2: Patterns created photons deposited on the bottom of the water tank.

Appendix C

Fit results

In this appendix, the fit result mentioned in section 5.4 are reported in their entirety.

C.1 Event

The behaviour of the event spectrum is exponential, thereby the following function was fitted:

$$y = N e^{-x/\tau} + c_E . \quad (\text{C.1})$$

C				
Correlation matrix				Best fit
	N	$1/\tau$	c_E	
N	1.000	-0.996	0.532	0.997
$1/\tau$	-0.996	1.000	-0.563	0.997
c_E	0.532	-0.563	1.000	0.650

V_{00}				
Correlation matrix				Best fit
	N	$1/\tau$	c_E	
N	1.000	-0.989	0.508	0.991
$1/\tau$	-0.989	1.000	-0.568	0.992
c_E	0.508	-0.568	1.000	0.674

V_{01}				
Correlation matrix				Best fit
	N	$1/\tau$	c_E	
N	1.000	-0.990	0.446	0.992
$1/\tau$	-0.990	1.000	-0.518	0.992
c_E	0.446	-0.518	1.000	0.620

V_{05}

Correlation matrix

	N	$1/\tau$	c_E	Global
N	1.000	-0.996	0.434	0.997
$1/\tau$	-0.996	1.000	-0.462	0.997
c_E	0.434	-0.462	1.000	0.554

Best fit

	Value	Error	Err%	Unit
N	11.4	0.2		
$1/\tau$	-0.36	0.02		μs^{-1}
c_E	3594	5		

 V_{10}

Correlation matrix

	N	$1/\tau$	c_E	Global
N	1.000	-0.858	0.709	0.963
$1/\tau$	-0.858	1.000	-0.963	0.995
c_E	0.709	-0.963	1.000	0.990

Best fit

	Value	Error	Err%	Unit
N	6.0	0.1		
$1/\tau$	-0.46	0.01		μs^{-1}
c_E	2.57×10^3	0.02×10^3		

 N_{15}

Correlation matrix

	N	$1/\tau$	c_E	Global
N	1.000	-0.997	0.539	0.997
$1/\tau$	-0.997	1.000	-0.567	0.997
c_E	0.539	-0.567	1.000	0.645

Best fit

	Value	Error	Err%	Unit
N	12.2	0.1		
$1/\tau$	-0.327	0.008		μs^{-1}
c_E	5488	7		

 N_{30}

Correlation matrix

	N	$1/\tau$	c_E	Global
N	1.000	-0.996	0.560	0.997
$1/\tau$	-0.996	1.000	-0.562	0.997
c_E	0.560	-0.592	1.000	0.680

Best fit

	Value	Error	Err%	Unit
N	11.8	0.1		
$1/\tau$	-0.326	0.01		μs^{-1}
c_E	5103	8		

 N_{50}

Correlation matrix

	N	$1/\tau$	c_E	Global
N	1.000	-0.996	0.497	0.996
$1/\tau$	-0.996	1.000	-0.527	0.997
c_E	0.497	-0.527	1.000	0.610

Best fit

	Value	Error	Err%	Unit
N	11.1	0.1		
$1/\tau$	-0.30	0.01		μs^{-1}
c_E	4085	5		

Δ_{50}

Correlation matrix

	N	$1/\tau$	c_E	Global
N	1.000	-0.997	0.406	0.997
$1/\tau$	-0.997	1.000	-0.427	0.998
c_E	0.406	-0.427	1.000	0.499

Best fit

	Value	Error	Err%	Unit
N	11.35	0.08		
$1/\tau$	-0.403	0.006		μs^{-1}
c_E	6055	6		

 Δ_{30}

Correlation matrix

	N	$1/\tau$	c_E	Global
N	1.000	-0.999	0.620	0.999
$1/\tau$	-0.999	1.000	-0.633	0.999
c_E	0.620	-0.633	1.000	0.682

Best fit

	Value	Error	Err%	Unit
N	12.9	0.2		
$1/\tau$	-0.38	0.01		μs^{-1}
c_E	5337	7		

 Δ_{20}

Correlation matrix

	N	$1/\tau$	c_E	Global
N	1.000	-0.998	0.394	0.998
$1/\tau$	-0.998	1.000	-0.409	0.998
c_E	0.394	-0.409	1.000	0.473

Best fit

	Value	Error	Err%	Unit
N	14.1	0.1		
$1/\tau$	-0.48	0.01		μs^{-1}
c_E	4295	5		

 Δ_{10}

Correlation matrix

	N	$1/\tau$	c_E	Global
N	1.000	-0.998	0.335	0.998
$1/\tau$	-0.998	1.000	-0.352	0.998
c_E	0.335	-0.352	1.000	0.424

Best fit

	Value	Error	Err%	Unit
N	13.6	0.2		
$1/\tau$	-0.48	0.01		μs^{-1}
c_E	3346	4		

C.2 Noise

The behaviour of the event spectrum is exponential, thereby the following function was fitted:

$$y = A \exp\left(-\frac{(x - \mu)^2}{2\sigma^2}\right) + c_N. \quad (\text{C.2})$$

 C

Correlation matrix

	A	μ	σ	c_N	Global
A	1.000	0.170	0.574	-0.150	0.694
μ	0.170	1.000	0.321	0.010	0.350
σ	0.574	0.321	1.000	0.364	0.762
c_N	-0.150	0.010	0.364	1.000	0.582

Best fit

	Value	Error	Err%	Unit
A	1.43×10^3	0.03×10^3		
μ	17.66	0.05		μs
σ	2.03	0.07		μs
c_N	6312	9		

$$V_{00}$$

Correlation matrix

	A	μ	σ	c_N	Global
A	1.000	0.038	-0.615	-0.078	0.726
μ	0.038	1.000	-0.062	-0.064	0.131
σ	-0.615	-0.062	1.000	-0.435	0.786
c_N	-0.078	-0.064	-0.435	1.000	0.625

Best fit

	Value	Error	Err%	Unit
A	4.16×10^3	0.06×10^3		
μ	17.85	0.03		μs
σ	2.24	0.06		μs
c_N	29.87×10^3	0.02×10^3		

$$V_{01}$$

Correlation matrix

	A	μ	σ	c_N	Global
A	1.000	0.082	-0.670	-0.030	0.744
μ	0.082	1.000	-0.154	-0.031	0.200
σ	-0.670	-0.154	1.000	-0.391	0.794
c_N	-0.030	-0.031	-0.391	1.000	0.565

Best fit

	Value	Error	Err%	Unit
A	3.53×10^3	0.05×10^3		
μ	17.73	0.03		μs
σ	2.18	0.06		μs
c_N	29.84×10^3	0.01×10^3		

$$V_{05}$$

Correlation matrix

	A	μ	σ	c_N	Global
A	1.000	0.074	-0.545	-0.138	0.649
μ	0.074	1.000	-0.120	0.023	0.122
σ	-0.545	-0.120	1.000	-0.351	0.698
c_N	-0.138	0.023	-0.351	1.000	0.527

Best fit

	Value	Error	Err%	Unit
A	0.58×10^3	0.01×10^3		
μ	18.16	0.05		μs
σ	1.85	0.06		μs
c_N	1411	4		

 V_{10}

Correlation matrix

	A	μ	σ	c_N	Global
A	1.000	0.164	-0.491	-0.157	0.620
μ	0.164	1.000	-0.319	0.119	0.319
σ	-0.491	-0.319	1.000	-0.389	0.703
c_N	-0.157	0.119	-0.389	1.000	0.557

Best fit

	Value	Error	Err%	Unit
A	0.29×10^3	0.01×10^3		
μ	18.22	0.06		μs
σ	1.58	0.07		μs
c_N	653	3		

 N_{15}

Correlation matrix

	A	μ	σ	c_N	Global
A	1.000	0.105	-0.584	-0.144	0.682
μ	0.105	1.000	-0.182	-0.014	0.201
σ	-0.584	-0.182	1.000	-0.324	0.725
c_N	-0.144	-0.014	-0.324	1.000	0.557

Best fit

	Value	Error	Err%	Unit
A	1.47×10^3	0.03×10^3		
μ	17.61	0.04		μs
σ	2.18	0.06		μs
c_N	6107	7		

 N_{30}

Correlation matrix

	A	μ	σ	c_N	Global
A	1.000	0.416	-0.856	0.138	0.890
μ	0.416	1.000	-0.519	0.122	0.541
σ	-0.856	-0.519	1.000	-0.411	0.920
c_N	0.138	-0.122	-0.411	1.000	0.557

Best fit

	Value	Error	Err%	Unit
A	1.44×10^3	0.04×10^3		
μ	17.56	0.06		μs
σ	2.8	0.1		μs
c_N	6177	8		

 N_{50}

Correlation matrix

	A	μ	σ	c_N	Global
A	1.000	0.267	-0.597	-0.061	0.692
μ	0.267	1.000	-0.647	0.117	0.687
σ	-0.597	-0.647	1.000	-0.347	0.844
c_N	-0.061	0.117	-0.347	1.000	0.525

Best fit

	Value	Error	Err%	Unit
A	1.50×10^3	0.03×10^3		
μ	17.76	0.08		μs
σ	2.1	0.1		μs
c_N	6850	8		

 Δ_{50}

Correlation matrix

	A	μ	σ	c_N	Global
A	1.000	0.000	-0.644	-0.081	0.690
μ	0.000	1.000	-0.023	-0.043	0.666
σ	-0.644	-0.023	1.000	-0.246	0.711
c_N	-0.081	-0.043	-0.246	1.000	0.401

Best fit

	Value	Error	Err%	Unit
A	1.38×10^3	0.03×10^3		
μ	18.03	0.04		μs
σ	1.88	0.06		μs
c_N	5871	5		

 Δ_{30}

Correlation matrix

	A	μ	σ	c_N	Global
A	1.000	0.323	-0.641	-0.036	0.733
μ	0.323	1.000	-0.597	0.134	0.627
σ	-0.641	-0.597	1.000	-0.413	0.851
c_N	-0.036	0.134	-0.413	1.000	0.597

Best fit

	Value	Error	Err%	Unit
A	1.51×10^3	0.03×10^3		
μ	17.04	0.07		μs
σ	3.0	0.1		μs
c_N	6611	8		

$$\Delta_{20}$$

Correlation matrix

	A	μ	σ	c_N	Global
A	1.000	0.215	-0.553	-0.120	0.681
μ	0.215	1.000	-0.550	0.081	0.598
σ	-0.553	-0.550	1.000	-0.384	0.816
c_N	-0.120	0.081	-0.384	1.000	0.591

Best fit

	Value	Error	Err%	Unit
A	1.68×10^3	0.03×10^3		
μ	17.65	0.06		μs
σ	2.20	0.08		μs
c_N	7.70×10^3	0.01×10^3		

$$\Delta_{10}$$

Correlation matrix

	A	μ	σ	c_N	Global
A	1.000	0.190	-0.571	-0.120	0.678
μ	0.190	1.000	-0.484	0.043	0.530
σ	-0.571	-0.484	1.000	-0.339	0.788
c_N	-0.120	0.043	-0.339	1.000	0.544

Best fit

	Value	Error	Err%	Unit
A	1.86×10^3	0.03×10^3		
μ	17.60	0.05		μs
σ	2.02	0.07		μs
c_N	8653	9		

C.3 All data

The behaviour of the whole spectrum has two componente, an exponential and a gaussian one, thereby the following function was fitted:

$$y = N_T e^{-x/\tau_T} + A_T \exp\left(-\frac{(x - \mu_T)^2}{2\sigma_T^2}\right) + c_T . \quad (\text{C.3})$$

C

Correlation matrix

	A_T	μ_T	σ_T	N_T	$1/\tau_T$	c_T	Global
A_T	1.000	-0.178	-0.236	0.733	-0.737	-0.329	0.826
μ_T	-0.178	1.000	-0.103	-0.103	0.110	-0.142	0.302
σ_T	-0.236	-0.103	1.000	-0.656	0.662	-0.263	0.794
N_T	0.733	-0.103	-0.656	1.000	0.999	0.544	0.999
$1/\tau_T$	-0.737	0.110	0.662	0.999	1.000	-0.558	0.999
c_T	-0.329	-0.142	-0.263	0.544	-0.558	1.000	0.689

Best fit

	Value	Error	Err%	Unit
A_T	1.42×10^3	0.06×10^3		
μ_T	18.13	0.05		μs
σ_T	1.24	0.05		μs
N_T	12.4	0.1		
$1/\tau_T$	-0.31	0.01		μs^{-1}
c_T	12.00×10^3	0.01×10^3		

 V_{00}

Correlation matrix

	A_T	μ_T	σ_T	N_T	$1/\tau_T$	c_T	Global
A_T	1.000	0.003	0.107	0.588	-0.597	0.426	0.759
μ_T	0.003	1.000	0.329	0.223	-0.218	0.114	0.353
σ_T	0.107	0.329	1.000	0.651	-0.661	0.454	0.813
N_T	0.588	0.223	0.651	1.000	-0.997	0.763	0.998
$1/\tau_T$	-0.597	-0.218	-0.661	-0.997	1.000	-0.783	0.996
c_T	0.426	0.114	0.454	0.763	-0.783	1.000	0.848

Best fit

	Value	Error	Err%	Unit
A_T	5.2×10^3	0.1×10^3		
μ_T	17.76	0.02		μs
σ_T	1.01	0.03		μs
N_T	12.49	0.07		
$1/\tau_T$	-0.233	0.005		μs^{-1}
c_T	4.00×10^3	0.03×10^3		

V_{01}

Correlation matrix

	A_T	μ_T	σ_T	N_T	$1/\tau_T$	c_T	Global
A_T	1.000	-0.025	-0.051	0.496	-0.513	0.288	0.706
μ_T	-0.025	1.000	0.391	0.259	-0.255	0.111	0.409
σ_T	-0.051	0.391	1.000	0.527	-0.544	0.290	0.749
N_T	0.496	0.259	0.527	1.000	-0.995	0.607	0.997
$1/\tau_T$	-0.513	-0.255	-0.544	-0.995	1.000	-0.634	0.997
c_T	0.288	0.111	0.290	0.607	-0.634	1.000	0.713

Best fit

	Value	Error	Err%	Unit
A_T	3.55×10^3	0.09×10^3		
μ_T	17.78	0.03		μs
σ_T	0.95	0.03		μs
N_T	12.00	0.05		
$1/\tau_T$	-0.215	0.004		μs^{-1}
c_T	29.33×10^3	0.02×10^3		

V_{05}

Correlation matrix

	A_T	μ_T	σ_T	N_T	$1/\tau_T$	c_T	Global
A_T	1.000	-0.401	-0.083	0.480	-0.479	-0.076	0.720
μ_T	-0.401	1.000	-0.543	-0.742	0.744	-0.099	0.757
σ_T	0.083	-0.543	1.000	0.768	-0.789	-0.076	0.887
N_T	0.480	-0.742	0.786	1.000	-1.000	0.071	0.994
$1/\tau_T$	-0.479	0.744	-0.789	-1.000	1.000	-0.075	0.998
c_T	-0.076	-0.099	-0.076	0.071	-0.075	1.000	0.439

Best fit

	Value	Error	Err%	Unit
A_T	0.77×10^3	0.03×10^3		
μ_T	18.09	0.09		μs
σ_T	1.7	0.1		μs
N_T	14.4	0.8		
$1/\tau_T$	-0.57	0.06		μs^{-1}
c_T	5023	5		

V_{10}

Correlation matrix

	A_T	μ_T	σ_T	N_T	$1/\tau_T$	c_T	Global
A_T	1.000	0.601	-0.997	0.001	-0.003	-0.003	0.997
μ_T	0.601	1.000	-0.592	-0.003	-0.005	0.003	0.608
σ_T	-0.997	-0.592	1.000	-0.001	0.000	0.000	0.997
N_T	0.001	0.003	-0.001	1.000	-0.949	0.430	0.964
$1/\tau_T$	-0.003	-0.005	0.000	-0.949	1.000	-0.596	0.972
c_T	0.002	0.003	0.000	0.430	-0.596	1.000	0.736

Best fit

	Value	Error	Err%	Unit
A_T	7×10^3	5×10^3		
μ_T	17.40	0.002		μs
σ_T	0.049	0.008		μs
N_T	7.2	0.1		
$1/\tau_T$	-0.108	0.008		μs^{-1}
c_T	3288	4		

 N_{15}

Correlation matrix

	A_T	μ_T	σ_T	N_T	$1/\tau_T$	c_T	Global
A_T	1.000	0.082	0.179	0.774	-0.783	0.559	0.862
μ_T	0.082	1.000	0.376	0.256	-0.252	0.155	0.397
σ_T	0.179	0.376	1.000	0.543	-0.549	0.382	0.737
N_T	0.774	0.256	0.543	1.000	-0.998	0.738	0.999
$1/\tau_T$	-0.783	-0.252	-0.549	-0.998	1.000	-0.750	0.999
c_T	0.559	0.155	0.382	0.738	-0.750	1.000	0.789

Best fit

	Value	Error	Err%	Unit
A_T	1.01×10^3	0.08×10^3		
μ_T	17.24	0.06		μs
σ_T	1.06	0.05		μs
N_T	11.1	0.1		
$1/\tau_T$	-0.214	0.009		μs^{-1}
c_T	11.14×10^3	0.01×10^3		

 N_{30}

Correlation matrix

	A_T	μ_T	σ_T	N_T	$1/\tau_T$	c_T	Global
A_T	1.000	-0.139	0.176	0.693	-0.699	0.248	0.800
μ_T	-0.139	1.000	0.160	-0.039	0.047	-0.096	0.287
σ_T	0.176	0.160	1.000	0.604	-0.612	0.187	0.763
N_T	0.693	-0.039	0.604	1.000	-0.998	0.451	0.998
$1/\tau_T$	-0.699	0.047	-0.612	-0.998	1.000	-0.467	0.999
c_T	0.248	-0.096	0.187	0.451	-0.467	1.000	0.602

Best fit

	Value	Error	Err%	Unit
A_T	1.37×10^3	0.06×10^3		
μ_T	18.26	0.05		μs
σ_T	1.26	0.05		μs
N_T	12.2	0.1		
$1/\tau_T$	-0.30	0.01		μs^{-1}
c_T	11,206	9		

 N_{50}

Correlation matrix

	A_T	μ_T	σ_T	N_T	$1/\tau_T$	c_T	Global
A_T	1.000	-0.997	-0.999	0.023	-0.025	0.013	0.999
μ_T	-0.977	1.000	0.970	-0.039	0.043	-0.021	0.996
σ_T	-0.999	0.970	1.000	-0.019	0.019	-0.011	1.000
N_T	0.023	-0.039	-0.019	1.000	-0.985	0.504	0.989
$1/\tau_T$	-0.025	0.043	0.019	-0.985	1.000	-0.576	0.990
c_T	0.013	-0.021	-0.011	0.504	-0.576	1.000	0.688

Best fit

	Value	Error	Err%	Unit
A_T	0.1×10^6	0.9×10^6		
μ_T	17.81	0.02		μs
σ_T	0.03	0.03		μs
N_T	10.69	0.05		
$1/\tau_T$	-0.188	0.003		μs^{-1}
c_T	11.08×10^3	0.01×10^3		

$$\Delta_{50}$$

Correlation matrix

	A_T	μ_T	σ_T	N_T	$1/\tau_T$	c_T	Global
A_T	1.000	-0.101	0.159	0.685	-0.693	0.289	0.794
μ_T	-0.101	1.000	0.230	0.030	-0.022	-0.063	0.308
σ_T	0.159	0.230	1.000	0.585	-0.593	0.218	0.753
N_T	0.685	0.030	0.585	1.000	-0.998	0.510	0.998
$1/\tau_T$	-0.693	-0.022	-0.593	-0.998	1.000	-0.528	0.998
c_T	0.289	-0.063	0.218	0.510	-0.528	1.000	0.650

Best fit

	Value	Error	Err%	Unit
A_T	1.34×10^3	0.06×10^3		
μ_T	18.16	0.05		μs
σ_T	1.19	0.05		μs
N_T	12.08	0.1		
$1/\tau_T$	-0.284	0.01		μs^{-1}
c_T	11.94×10^3	0.01×10^3		

$$\Delta_{30}$$

Correlation matrix

	A_T	μ_T	σ_T	N_T	$1/\tau_T$	c_T	Global
A_T	1.000	-0.045	0.132	0.671	-0.682	0.298	0.784
μ_T	-0.045	1.000	0.321	0.125	-0.119	-0.002	0.348
σ_T	0.132	0.321	1.000	0.557	-0.566	0.224	0.734
N_T	0.671	0.124	0.557	1.000	-0.997	0.513	0.998
$1/\tau_T$	-0.682	-0.119	-0.566	-0.997	1.000	-0.532	0.998
c_T	0.298	-0.002	0.224	0.513	-0.532	1.000	0.633

Best fit

	Value	Error	Err%	Unit
A_T	1.25×10^3	0.06×10^3		
μ_T	18.17	0.05		μs
σ_T	1.14	0.05		μs
N_T	11.8	0.1		
$1/\tau_T$	-0.260	0.008		μs^{-1}
c_T	11,881	9		

Δ_{20}

Correlation matrix

	A_T	μ_T	σ_T	N_T	$1/\tau_T$	c_T	Global
A_T	1.000	-0.211	-0.045	0.524	-0.524	0.071	0.724
μ_T	-0.211	1.000	0.026	-0.266	0.277	-0.257	0.369
σ_T	-0.045	-0.026	1.000	0.466	-0.468	-0.001	0.722
N_T	0.524	-0.266	0.466	1.000	-0.998	0.472	0.998
$1/\tau_T$	-0.524	0.227	-0.468	-0.998	1.000	-0.500	0.999
c_T	0.071	-0.257	-0.001	0.472	-0.500	1.000	0.774

Best fit

	Value	Error	Err%	Unit
A_T	1.50×10^3	0.05×10^3		
μ_T	18.29	0.05		μs
σ_T	1.27	0.04		μs
N_T	13.0	0.1		
$1/\tau_T$	-0.36	0.01		μs^{-1}
c_T	11.17×10^3	0.02×10^3		

 Δ_{10}

Correlation matrix

	A_T	μ_T	σ_T	N_T	$1/\tau_T$	c_T	Global
A_T	1.000	-0.055	0.146	0.680	-0.689	0.311	0.789
μ_T	-0.055	1.000	0.296	0.106	-0.099	-0.014	0.338
σ_T	0.146	0.296	1.000	0.567	-0.576	0.235	0.740
N_T	0.680	0.106	0.567	1.000	-0.998	0.530	0.998
$1/\tau_T$	-0.689	-0.099	-0.576	-0.998	1.000	-0.549	0.998
c_T	0.311	-0.014	0.235	0.530	-0.549	1.000	0.654

Best fit

	Value	Error	Err%	Unit
A_T	1.27×10^3	0.06×10^3		
μ_T	18.17	0.05		μs
σ_T	1.15	0.05		μs
N_T	11.8	0.1		
$1/\tau_T$	-0.265	0.008		μs^{-1}
c_T	11,189	9		

Bibliography

- [1] A. A. Aguilar-Arevalo, C. E. Anderson, A. O. Bazarko, S. J. Brice, B. C. Brown, L. Bugel, J. Cao, L. Coney, J. M. Conrad, D. C. Cox, A. Curioni, Z. Djurcic, D. A. Finley, B. T. Fleming, R. Ford, F. G. Garcia, G. T. Garvey, J. Grange, C. Green, J. A. Green, T. L. Hart, E. Hawker, R. Imlay, R. A. Johnson, G. Karagiorgi, P. Kasper, T. Katori, T. Kobilarcik, I. Kourbanis, S. Koutsoliotas, E. M. Laird, S. K. Linden, J. M. Link, Y. Liu, Y. Liu, W. C. Louis, K. B M Mahn, W. Marsh, C. Mauger, V. T. McGary, G. McGregor, W. Metcalf, P. D. Meyers, F. Mills, G. B. Mills, J. Monroe, C. D. Moore, J. Mousseau, R. H. Nelson, P. Nienaber, J. A. Nowak, B. Osmanov, S. Ouedraogo, R. B. Patterson, Z. Pavlovic, D. Perevalov, C. C. Polly, E. Prebys, J. L. Raaf, H. Ray, B. P. Roe, A. D. Russell, V. Sandberg, R. Schirato, D. Schmitz, M. H. Shaevitz, F. C. Shoemaker, D. Smith, M. Soderberg, M. Sorel, P. Spentzouris, J. Spitz, I. Stancu, R. J. Stefanski, M. Sung, H. A. Tanaka, R. Tayloe, M. Tzanov, R. G. Van De Water, M. O. Wascko, D. H. White, M. J. Wilking, H. J. Yang, G. P. Zeller, and E. D. Zimmerman. First measurement of the muon neutrino charged current quasielastic double differential cross section. *Physical Review D - Particles, Fields, Gravitation and Cosmology*, 81(9):1–22, 2010.
- [2] A. A. Aguilar-Arevalo, B. C. Brown, L. Bugel, G. Cheng, E. D. Church, J. M. Conrad, R. Dharmapalan, Z. Djurcic, D. A. Finley, R. Ford, F. G. Garcia, G. T. Garvey, J. Grange, W. Huelsnitz, C. Ignarra, R. Imlay, R. A. Johnson, G. Karagiorgi, T. Katori, T. Kobilarcik, W. C. Louis, C. Mariani, W. Marsh, G. B. Mills, J. Mirabal, C. D. Moore, J. Mousseau, P. Nienaber, B. Osmanov, Z. Pavlovic, D. Perevalov, C. C. Polly, H. Ray, B. P. Roe, A. D. Russell, M. H. Shaevitz, J. Spitz, I. Stancu, R. Tayloe, R. G. Van De Water, M. O. Wascko, D. H. White, D. A. Wickremasinghe, G. P. Zeller, and E. D. Zimmerman. First measurement of the muon antineutrino double-differential charged-current quasielastic cross section. *Physical Review D - Particles, Fields, Gravitation and Cosmology*, 88(3), 2013.
- [3] I Anghel, J F Beacom, M Bergevin, C Blanco, F Di Lodovico, a Elagin, H Frisch, J Griskevich, R Hill, G Jocher, T Katori, F Krennrich, J Learned, M Malek, R Northrop, C Pilcher, E Ramberg, J Repond, R Sacco, M C Sanchez, M Smy, H Sobel, R Svoboda, S M Usman, M Vagins, G Varner, R Wagner, a Weinstein, M Wetstein, L Winslow, L Xia, M Yeh, Fermi National, National Geospatial-intelligence Agency, and West Lafayette. The Accelerator Neutrino Neutron Interaction Experiment. pages 1–56, 2014.
- [4] I. Anghel, J. F. Beacom, M. Bergevin, G. Davies, F. Di Lodovico, A. Elagin, H. Frisch, R. Hill, G. Jocher, T. Katori, J. Learned, R. Northrop, C. Pilcher, E. Ramberg, M. C. Sanchez, M. Smy, H. Sobel, R. Svoboda, S. Usman, M. Vagins, G. Varner, R. Wagner, M. Wetstein, L. Winslow, and M. Yeh. Expression of Interest: The Atmospheric Neutrino Neutron Interaction Experiment (ANNIE). pages 1–22, 2014.
- [5] S. Chatrchyan, V. Khachatryan, A. M. Sirunyan, A. Tumasyan, W. Adam, E. Aguilo,

T. Bergauer, M. Dragicevic, J. Er??, C. Fabjan, M. Friedl, R. Fr??hwirth, V. M. Ghete, J. Hammer, M. Hoch, N. H??rmann, J. Hrubec, M. Jeitler, W. Kiesenhofer, V. Kn??nz, M. Krammer, I. Kr??tschmer, D. Liko, W. Majerotto, I. Mikulec, M. Pernicka, B. Rahbaran, C. Rohringer, H. Rohringer, R. Sch??fbeck, J. Strauss, F. Szoncs??, A. Taurok, W. Waltenberger, G. Walzel, E. Widl, C. E. Wulz, V. Chekhovsky, I. Emeliantchik, A. Litomin, V. Makarenko, V. Mossolov, N. Shumeiko, A. Solin, R. Stefanovitch, J. Suarez Gonzalez, A. Fedorov, M. Korzhik, O. Mishevitch, R. Zuyeuski, M. Bansal, S. Bansal, W. Beaumont, T. Cornelis, E. A. De Wolf, D. Druzhkin, X. Janssen, S. Luyckx, L. Mucibello, S. Ochesanu, B. Roland, R. Rougny, M. Selvaggi, Z. Staykova, H. Van Haevermaet, P. Van Mechelen, N. Van Remortel, A. Van Spilbeeck, F. Blekman, S. Blyweert, J. D'Hondt, O. Devroede, R. Gonzalez Suarez, R. Goorens, A. Kalogeropoulos, M. Maes, A. Olbrechts, S. Tavernier, W. Van Doninck, L. Van Lancker, P. Van Mulders, G. P. Van Onsem, I. Villella, B. Clerbaux, G. De Lent-decker, V. Dero, J. P. Dewulf, A. P R Gay, T. Hreus, A. L??onard, P. E. Marage, A. Mohammadi, T. Reis, S. Rugovac, L. Thomas, C. Vander Velde, P. Vanlaer, J. Wang, J. Wickens, V. Adler, K. Beernaert, A. Cimmino, S. Costantini, G. Garcia, M. Grunewald, B. Klein, J. Lellouch, A. Marinov, J. Mccartin, A. A. Ocampo Rios, D. Ryckbosch, N. Strobbe, F. Thyssen, M. Tytgat, S. Walsh, E. Yazgan, N. Zaganidis, S. Basegmez, G. Bruno, R. Castello, L. Ceard, J. De Favereau De Jeneret, C. Delaere, P. Demin, T. du Pree, D. Favart, L. Forthomme, A. Giannanco, G. Gr??goire, J. Hollar, V. Lemaitre, J. Liao, O. Militaru, C. Nuttens, D. Pagano, A. Pin, K. Piotrkowski, N. Schul, J. M. Vizan Garcia, N. Beliy, T. Caebergs, E. Daubie, G. H. Hammad, G. A. Alves, L. Brito, M. Correa Martin, T. Martins, M. E. Pol, M. H G Souza, W. L. Ald?? J??nior, W. Carvalho, A. Cust??dio, E. M. Da Costa, D. De Jesus Damiao, C. De Oliveira Martins, S. Fonseca De Souza, D. Matos Figueiredo, L. Mundim, H. Nogima, V. Oguri, W. L. Prado Da Silva, A. Santoro, A. Sznajder, A. Vilela Pereira, T. S. Anjos, C. A. Bernardes, F. A. Dias, T. R. Fernandez Perez Tomei, E. M. Gregores, R. L. Iope, C. Lagana, S. M. Lietti, F. Marinho, P. G. Mercadante, S. F. Novaes, Sandra S. Padula S., L. Dimitrov, V. Genchev, P. Iaydjiev, S. Piperov, M. Rodozov, S. Stoykova, G. Sultanov, V. Tcholakov, R. Trayanov, I. Vankov, M. Vutova, C. Roumenin, D. Uzunova, R. Zashariev, A. Dimitrov, R. Hadjiiska, V. Kozhuharov, L. Litov, B. Pavlov, P. Petkov, J. G. Bian, G. M. Chen, H. S. Chen, K. L. He, C. H. Jiang, W. G. Li, D. Liang, S. Liang, X. Meng, G. Sun, H. S. Sun, J. Tao, J. Wang, X. Wang, Z. Wang, H. Xiao, M. Xu, M. Yang, J. Zang, X. Zhang, Z. Zhang, Z. Zhang, W. R. Zhao, Z. Zhu, C. Asawatangtrakuldee, Y. Ban, J. Cai, S. Guo, Y. Guo, W. Li, H. T. Liu, S. Liu, Y. Mao, S. J. Qian, H. Teng, D. Wang, Y. L. Ye, L. Zhang, B. Zhu, W. Zou, C. Avila, J. P. Gomez, B. Gomez Moreno, A. F. Osorio Oliveros, J. C. Sanabria, N. Godinovic, D. Lelas, R. Plestina, D. Polic, I. Puljak, Z. Antunovic, M. Kovac, V. Brigljevic, S. Duric, K. Kadija, J. Luetic, S. Morovic, A. Attikis, M. Galanti, G. Mavromanolakis, J. Mousa, C. Nicolaou, F. Ptochos, P. A. Razis, M. Finger, M. Finger, A. Aly, Y. Assran, A. Awad, S. Elgammal, A. Ellithi Kamel, S. Khalil, M. A. Mahmoud, A. Mahrous, A. Radi, A. Hektor, M. Kadastik, K. Kannike, M. M??ntel, M. Raidal, L. Rebane, A. Strumia, A. Tiko, P. Eerola, G. Fedi, M. Voutilainen, E. Anttila, J. H??rk??nen, A. Heikkinen, V. Karim??ki, H. M. Katajisto, R. Kinnunen, M. J. Kortelainen, M. Kotam??ki, T. Lamp??n, K. Lassila-Perini, S. Lehti, T. Lind??n, P. Luukka, T. M??enp????, T. Peltola, E. Tuominen, J. Tuominiemi, E. Tuovinen, D. Ungaro, T. P. Vanhala, L. Wendland, K. Banzuzi, A. Karjalainen, A. Korpela, T. Tuuva, M. Anfreville, M. Besancon, S. Choudhury, M. Dejardin, D. Denegri, B. Fabbro, J. L. Faure, F. Ferri, S. Ganjour, F. X. Gentit, A. Givernaud, P. Gras, G. Hamel de Monchenault, P. Jarry, F. Kircher, M. C. Lemaire, E. Locci, J. Malcles, I. Mand-

javidze, A. Nayak, J. P. Pansart, J. Rander, J. M. Reymond, A. Rosowsky, I. Shreyber, M. Titov, P. Verrecchia, J. Badier, S. Baffioni, F. Beaudette, E. Becheva, L. Benhabib, L. Bianchini, M. Bluj, C. Broutin, P. Busson, M. Cerutti, D. Chamont, C. Charlot, N. Daci, T. Dahms, M. Dalchenko, L. Dobrzynski, Y. Geerebaert, R. Granier de Cassagnac, M. Haguenuauer, P. Hennion, G. Milleret, P. Min??, C. Mironov, I. N. Naranjo, M. Nguyen, C. Ochando, P. Paganini, T. Romanteau, D. Sabes, R. Salerno, A. Sartirana, Y. Sirois, C. Thiebaux, C. Veelken, A. Zabi, J. L. Agram, J. Andrea, A. Besson, D. Bloch, D. Bodin, J. M. Brom, M. Cardaci, E. C. Chabert, C. Collard, E. Conte, F. Drouhin, C. Ferro, J. C. Fontaine, D. Gel??, U. Goerlach, C. Goetzmann, L. Gross, D. Huss, P. Juillot, E. Kieffer, A. C. Le Bihan, J. Pansanel, Y. Pattois, P. Van Hove, D. Boutigny, D. Mercier, G. Baulieu, S. Beauceron, N. Beuppere, M. Bedjidian, O. Bondu, G. Boudoul, S. Brochet, J. Chasserat, R. Chierici, C. Combaret, D. Contardo, P. Depasse, H. El Mamouni, J. Fay, S. Gascon, N. Girraud, M. Gouzevitch, R. Haroutunian, B. Ille, T. Kurca, M. Lethuillier, N. Lumb, H. Mathez, L. Mirabito, S. Perries, L. Sgandurra, V. Sordini, Y. Tschudi, M. Vander Donckt, P. Verdier, S. Viret, V. Roinishvili, L. Rurua, N. Amaglobeli, I. Bagaturia, B. Chiladze, R. Kvataadze, D. Lomidze, R. Shanidze, Z. Tsamalaidze, R. Adolphi, G. Anagnostou, C. Autermann, S. Beranek, R. Brauer, W. Braunschweig, B. Calpas, M. Edelhoff, L. Feld, N. Heracleous, O. Hindrichs, R. Jussen, W. Karpinski, K. Klein, K. L??belsmeyer, J. Merz, A. Ostapchuk, D. Pandoulas, A. Perieanu, F. Raupach, J. Sammet, S. Schael, D. Schmitz, A. Schultz von Dratzig, R. Siedling, D. Sprenger, H. Weber, B. Wittmer, M. Wlochal, V. Zhukov, M. Ata, P. Biallass, J. Caudron, E. Dietz-Laursonn, D. Duchardt, M. Erdmann, R. Fischer, A. G??th, T. Hebbeker, C. Heidemann, G. Hilgers, K. Hoepfner, C. Hof, T. Klimkovich, D. Klingebiel, P. Kreuzer, C. Magass, M. Merschmeyer, A. Meyer, M. Olszewski, P. Papacz, B. Philipps, H. Pieta, H. Reithler, S. A. Schmitz, L. Sonnenschein, M. Sowa, J. Steggemann, D. Teyssier, M. Weber, M. Bontenackels, V. Cherepanov, Y. Erdogan, G. Fl??gge, H. Geenen, M. Geisler, W. Haj Ahmad, F. Hoehle, B. Kargoll, T. Kress, Y. Kuessel, J. Lingemann, A. Nowack, L. Perchalla, O. Pooth, P. Sauerland, A. Stahl, M. H. Zoeller, M. Aldaya Martin, J. Behr, W. Behrenhoff, U. Behrens, M. Bergholz, A. Bethani, K. Borras, A. Burgmeier, A. Cakir, L. Calligaris, A. Campbell, E. Castro, F. Costanza, D. Dammann, C. Diez Pardos, G. Eckerlin, D. Eckstein, A. Flossdorf, G. Flucke, A. Geiser, I. Glushkov, P. Goettlicher, A. Grebenyuk, P. Gunnellini, S. Habib, J. Hauk, G. Hellwig, H. Jung, M. Kasemann, P. Katsas, C. Kleinwort, H. Kluge, A. Knutsson, M. Kr??mer, D. Kr??cker, E. Kuznetsova, W. Lange, B. Lewendel, W. Lohmann, B. Lutz, R. Mankel, I. Marfin, M. Marienfeld, I. A. Melzer-Pellmann, A. B. Meyer, J. Mnich, C. Muhl, A. Mussgiller, S. Naumann-Emme, O. Novgorodova, J. Olzem, A. Parenti, H. Perrey, A. Petrukhin, D. Pitzl, A. Raspereza, P. M. Ribeiro Cipriano, C. Riedl, E. Ron, C. Rosemann, M. Rosin, J. Salfeld-Nebgen, R. Schmidt, T. Schoerner-Sadenius, N. Sen, A. Spiridonov, M. Stein, J. Tomaszewska, D. Volyansky, R. Walsh, C. Wissing, C. Youngman, V. Blobel, J. Draeger, H. Endrele, J. Erfle, U. Gebbert, M. G??rner, T. Hermanns, R. S. H??ing, K. Kaschube, G. Kaussen, H. Kirschenmann, R. Klanner, J. Lange, B. Mura, F. Nowak, T. Peiffer, N. Pietsch, D. Rathjens, C. Sander, H. Schettler, P. Schleper, E. Schlieckau, A. Schmidt, M. Schr??der, T. Schum, M. Seidel, J. Sibille, V. Sola, H. Stadie, G. Steinbr??ck, J. Thomsen, L. Vanelderden, C. Barth, J. Bauer, J. Berger, P. Bl??m, C. B??ser, V. Buege, Z. Y. Chen, S. Chowdhury, T. Chwalek, D. Daeuwel, W. De Boer, A. Descroix, A. Dierlamm, G. Dirkes, M. Fahrer, M. Feindt, U. Felzmann, M. Frey, A. Furgeri, I. Gebauer, A. Gessler, J. Gruschke, M. Guthoff, C. Hackstein, F. Hartmann, F. Hauler, T. Hauth, S. Heier, S. M. Heindl, M. Heinrich, A. Heiss, H. Held, K. H. Hoffmann, S. Honc, U. Husemann, M. Imhof, C. Jung, S. Junghans, I. Katkov,

U. Kerzel, D. Knoblauch, J. R. Komaragiri, M. Kr??ber, T. Kuhr, T. Liamsuwan, P. Lobelle Pardo, D. Martschei, A. Menchikov, X. Mol, D. M??rmann, S. Mueller, Th M??ller, D. Neuberger, M. B. Neuland, M. Niegel, A. N??rnberg, O. Oberst, A. Oehler, T. Ortega Gomez, J. Ott, C. Piasecki, A. Poschlad, G. Quast, K. Rabbertz, F. Ratnikov, N. Ratnikova, M. Renz, S. R??cker, F. Roederer, A. Sabellek, C. Saout, A. Scheurer, D. Schieferdecker, P. Schieferdecker, F. P. Schilling, M. Schmanau, G. Schott, W. Schwerdtfeger, H. J. Simonis, A. Skiba, F. M. Stober, A. Theel, W. H. Th??mmel, D. Troendle, A. Trunov, R. Ulrich, J. Wagner-Kuhr, S. Wayand, M. Weber, T. Weiler, M. Zeise, E. B. Ziebarth, M. Zvada, G. Daskalakis, T. Gerialis, S. Kesisoglou, A. Kyriakis, D. Loukas, I. Manolakos, A. Markou, C. Markou, C. Mavrommatis, E. Ntomari, L. Gouskos, A. Panagiotou, N. Saoulidou, I. Evangelou, C. Foudas, P. Kokkas, N. Manthos, I. Papadopoulos, V. Patras, F. A. Triantis, G. Bencze, C. Hajdu, P. Hidas, D. Horvath, F. Sikler, V. Veszpremi, G. Vesztergombi, P. Zalan, N. Beni, S. Czellar, A. Fenyvesi, J. Molnar, J. Palinkas, Z. Szillasi, J. Karancsi, P. Raics, Z. L. Trocsanyi, B. Ujvari, G. Zilizi, S. B. Beri, V. Bhandari, V. Bhatnagar, N. Dhingra, R. Gupta, M. Kaur, J. M. Kohli, M. Z. Mehta, N. Nishu, L. K. Saini, A. Sharma, J. B. Singh, Ashok Kumar, Arun Kumar, S. Ahuja, A. Bhardwaj, S. Chatterji, B. C. Choudhary, P. Gupta, S. Malhotra, M. Naimuddin, K. Ranjan, V. Sharma, R. K. Shivpuri, S. Banerjee, S. Bhattacharya, S. Dutta, B. Gomber, Sa Jain, Sh Jain, R. Khurana, S. Sarkar, M. Sharan, A. Abdulsalam, R. K. Choudhury, D. Dutta, M. Ghodgaonkar, S. Kailas, S. K. Kataria, V. Kumar, P. Mehta, A. K. Mohanty, L. M. Pant, P. Shukla, A. Topkar, T. Aziz, S. Chendvankar, P. V. Deshpande, S. N. Ganguli, S. Ganguly, M. Guchait, A. Gurtu, M. Maity, K. Mazumdar, G. B. Mohanty, B. Parida, M. R. Patil, R. Raghavan, K. Sudhakar, N. Wickramage, B. S. Acharya, S. Banerjee, S. Bheesette, S. Dugad, S. D. Kalmani, M. R. Krishnaswamy, V. R. Lakkireddi, N. K. Mondal, V. S. Narasimham, N. Panayam, P. Verma, F. Ardalan, H. Arfaei, H. Bakshiansohi, S. M. Etesami, A. Fahim, M. Hashemi, A. Jafari, M. Khakzad, M. Mohammadi Najafabadi, S. Paktinat Mehdibadi, B. Safarzadeh, M. Zeinali, M. Abbrescia, L. Barbone, C. Calabria, S. S. Chhibra, A. Colaleo, D. Creanza, N. De Filippis, M. De Palma, G. De Robertis, G. Donvito, L. Fiore, G. Iaselli, F. Loddo, G. Maggi, M. Maggi, N. Manna, B. Marangelli, S. My, S. Natali, S. Nuzzo, N. Pacifico, A. Pompili, G. Pugliese, A. Ranieri, F. Romano, G. Selvaggi, L. Silvestris, G. Singh, V. Spinoso, R. Venditti, P. Verwilligen, G. Zito, G. Abbiendi, A. C. Benvenuti, D. Bonacorsi, S. Braibant-Giacomelli, L. Brigliadori, P. Capiluppi, A. Castro, F. R. Cavallo, M. Cuffiani, G. M. Dallavalle, F. Fabbri, A. Fanfani, D. Fasanella, P. Giacomelli, C. Grandi, L. Guiducci, S. Marcellini, G. Masetti, M. Meneghelli, A. Montanari, F. L. Navarria, F. Odorici, A. Perrotta, F. Primavera, A. M. Rossi, T. Rovelli, G. P. Siroli, R. Travaglini, S. Albergo, G. Cappello, M. Chiorboli, S. Costa, F. Noto, R. Potenza, M. A. Saizu, A. Tricomi, C. Tuve, G. Barbagli, V. Ciulli, C. Civinini, R. D'Alessandro, E. Focardi, S. Frosali, E. Gallo, C. Genta, S. Gonzi, M. Meschini, S. Paoletti, G. Parrini, R. Ranieri, G. Sguazzoni, A. Tropiano, L. Benussi, S. Bianco, S. Colafranceschi, F. Fabbri, D. Piccolo, P. Fabricatore, S. Farinon, M. Greco, R. Musenich, S. Tosi, A. Benaglia, L. Carbone, P. D'Angelo, F. De Guio, L. Di Matteo, P. Dini, F. M. Farina, S. Fiorendi, S. Gennai, A. Ghezzi, S. Malvezzi, R. A. Manzoni, A. Martelli, A. Massironi, D. Menasce, L. Moroni, P. Negri, M. Paganoni, D. Pedrini, A. Pullia, S. Ragazzi, N. Redaelli, S. Sala, T. Tabarelli de Fatis, S. Buontempo, C. A. Carrillo Montoya, N. Cavallo, A. De Cosa, O. Dogangun, F. Fabozzi, A. O M Iorio, L. Lista, S. Meola, M. Merola, P. Paolucci, P. Azzi, N. Bacchetta, M. Bellato, M. Benettoni, M. Biasotto, D. Bisello, A. Branca, R. Carlin, P. Checchia, T. Dorigo, U. Dosselli, F. Fanzago, F. Gasparini, U. Gasparini, P. Giubilato, F. Gonella, A. Gozzelino, M. Gulmini, K. Kanishchev, S. Lacaprara,

I. Lazzizzera, M. Loreti, M. Margoni, G. Maron, M. Mazzucato, A. T. Meneguzzo, F. Montecassiano, M. Passaseo, J. Pazzini, M. Pegoraro, N. Pozzobon, P. Ronchese, F. Simonetto, E. Torassa, M. Tosi, S. Vanini, S. Ventura, P. Zotto, G. Zumerle, U. Berzano, M. Gabusi, S. P. Ratti, C. Riccardi, P. Torre, P. Vitulo, M. Biasini, G. M. Bilei, L. Fan??, P. Lariccia, A. Lucaroni, G. Mantovani, M. Menichelli, A. Nappi, D. Passeri, P. Placidi, F. Romeo, A. Saha, A. Santocchia, L. Servoli, A. Spiezzi, S. Tarroni, M. Valdata, F. Angelini, S. Arezzini, P. Azzurri, G. Bagliesi, A. Basti, R. Bellazzini, J. Bernardini, T. Boccali, F. Bosi, A. Brez, G. Broccolo, F. Calzolari, A. Carboni, R. Castaldi, C. Cerri, A. Ciampa, R. T. D'Agnolo, R. Dell'Orso, F. Fiori, L. Fo??, A. Giassi, S. Giusti, A. Kraan, L. Latronico, F. Ligabue, S. Linari, T. Lomtadze, L. Martini, M. Massa, M. M. Massai, E. Mazzoni, A. Messineo, A. Moggi, F. Palla, F. Raffaelli, A. Rizzi, G. Sanguinetti, G. Segneri, A. T. Serban, P. Spagnolo, G. Spandre, P. Squillaciotti, R. Tenchini, G. Tonelli, A. Venturi, P. G. Verdini, S. Baccaro, L. Barone, A. Bartoloni, F. Cavallari, I. Dafinei, D. Del Re, M. Diemoz, C. Fanelli, M. Grassi, E. Longo, P. Meridiani, F. Micheli, S. Nourbakhsh, G. Organtini, R. Paramatti, S. Rahatlou, M. Sigamani, L. Soffi, I. G. Talamo, N. Amapane, R. Arcidiacono, S. Argiro, M. Arneodo, C. Biino, N. Cartiglia, M. Costa, N. Demaria, C. Mariotti, S. Maselli, E. Migliore, V. Monaco, M. Musich, M. M. Obertino, N. Pastrone, M. Pelliccioni, C. Peroni, A. Potenza, A. Romero, M. Ruspa, R. Sacchi, A. Solano, A. Staiano, F. Ambroglini, S. Belforte, V. Candelise, M. Casarsa, F. Cossutti, G. Della Ricca, B. Gobbo, C. Kavka, M. Marone, D. Montanino, A. Penzo, A. Schizzi, T. Y. Kim, S. K. Nam, S. Chang, J. Chung, S. W. Ham, D. Han, J. Kang, D. H. Kim, G. N. Kim, J. E. Kim, K. S. Kim, D. J. Kong, M. W. Lee, Y. D. Oh, H. Park, S. R. Ro, D. Son, D. C. Son, J. S. Suh, J. Y. Kim, Zero J. Kim, S. Song, S. Choi, D. Gyun, B. Hong, M. Jo, Y. Jo, M. Kang, H. Kim, T. J. Kim, K. S. Lee, D. H. Moon, S. K. Park, K. S. Sim, M. Choi, G. Hahn, S. Kang, H. Kim, J. H. Kim, C. Park, I. C. Park, S. Park, G. Ryu, Y. Choi, Y. K. Choi, J. Goh, M. S. Kim, E. Kwon, B. Lee, J. Lee, S. Lee, H. Seo, I. Yu, M. Janulis, A. Juodagalvis, R. Naujikas, H. Castilla-Valdez, E. De La Cruz-Burelo, I. Heredia-de La Cruz, R. Lopez-Fernandez, R. Maga??a Villalba, J. Mart??nez-Ortega, A. S??nchez-Hern??ndez, L. M. Villasenor-Cendejas, S. Carrillo Moreno, F. Vazquez Valencia, H. A. Salazar Ibarguen, E. Casimiro Linares, A. Morelos Pineda, M. A. Reyes-Santos, P. Allfrey, D. Kroccheck, A. J. Bell, N. Bernardino Rodrigues, A. P H Butler, P. H. Butler, R. Doesburg, D. Pfeiffer, S. Reucroft, H. Silverwood, J. C. Williams, M. Ahmad, M. H. Ansari, M. I. Asghar, J. Butt, H. R. Hoorani, S. Khalid, W. A. Khan, T. Khurshid, S. Qazi, M. A. Shah, M. Shoaib, H. Bialkowska, B. Boimska, T. Frueboes, R. Gokieli, L. Goscilo, M. G??rski, M. Kazana, I. M. Kudla, K. Nawrocki, K. Romanowska-Rybinska, M. Szleper, G. Wrochna, P. Zalewski, G. Brona, K. Bunkowski, M. Cwiok, H. Czyrkowski, R. Dabrowski, W. Dominkik, K. Doroba, A. Kalinowski, M. Konecki, J. Krolikowski, W. Oklinski, K. Pozniak, W. Zabolotny, P. Zych, G. Kasprowicz, R. Romaniuk, R. Alemany-Fernandez, N. Almeida, P. Bargassa, A. David, P. Faccioli, P. G. Ferreira Parracho, M. Gallinaro, P. Q. Ribeiro, J. Seixas, J. Silva, J. Varela, P. Vischia, S. Afanasiev, I. Belotelov, P. Bunin, Y. Ershov, M. Gavrilenko, A. Golunov, I. Golutvin, N. Gorbounov, I. Gorbunov, I. Gramenitski, V. Kalagin, A. Kamenev, V. Karjavin, V. Konoplyanikov, V. Korenkov, G. Kozlov, A. Kurenkov, A. Lanev, A. Makankin, A. Malakhov, I. Melnitchenko, V. V. Mitsyn, P. Moisenz, D. Oleynik, A. Orlov, V. Palichik, V. Perelygin, A. Petrosyan, M. Savina, R. Semenov, S. Shmatov, S. Shulha, A. Skachkova, N. Skatchkov, V. Smetannikov, V. Smirnov, D. Smolin, E. Tikhonenko, S. Vasil'ev, A. Volodko, A. Zarubin, V. Zhiltsov, S. Evstyukhin, V. Golovtsov, Y. Ivanov, V. Kim, P. Levchenko, V. Murzin, V. Oreshkin, I. Smirnov, V. Sulimov, L. Uvarov, S. Vavilov, A. Vorobyev, An Vorobyev, Yu Andreev, A. Anisimov, A. Dermenev,

- S. Glinenko, N. Golubev, D. Gorbunov, A. Karneyeu, M. Kirsanov, N. Krasnikov, V. Matveev, A. Pashenkov, G. Pivovarov, V. E. Postoev, V. Rubakov, V. Shirinyants, A. Solovey, D. Tlisov, A. Toropin, S. Troitsky, V. Epshteyn, M. Erofeeva, V. Gavrilov, V. Kaftanov, I. Kiselevich, V. Kolosov, A. Konoplyannikov, M. Kossov, Y. Kozlov, A. Krokhutin, D. Litvintsev, N. Lychkovskaya, A. Oulianov, V. Popov, G. Safronov, S. Semenov, N. Stepanov, V. Stolin, E. Vlasov, V. Zaytsev, A. Zhokin, A. Belyaev, E. Boos, V. Bunichev, A. Demiyanov, M. Dubinin, L. Dudko, A. Ershov, A. Gribushin, V. Ilyin, A. Kaminskiy, V. Klyukhin, O. Kodolova, V. Korotkikh, A. Kryukov, I. Lokhtin, A. Markina, S. Obraztsov, M. Perfilov, S. Petrushanko, A. Popov, A. Proskuryakov, L. Sarycheva, V. Savrin, A. Snigirev, I. Vardanyan, V. Andreev, M. Azarkin, I. Dremin, M. Kirakosyan, A. Leonidov, G. Mesyats, S. V. Rusakov, A. Vinogradov, I. Azhgirey, I. Bayshev, S. Bitioukov, V. Grishin, V. Kachanov, A. Kalinin, D. Konstantinov, A. Korablev, V. Krychkine, A. Levine, V. Petrov, A. Ryabov, R. Ryutin, A. Sobol, V. Talov, L. Tourtchanovitch, S. Troshin, N. Tyurin, A. Uzunian, A. Volkov, P. Adzic, M. Djordjevic, M. Ekmedzic, D. Krpic, J. Milosevic, N. Smiljkovic, M. Zupan, M. Aguilar-Benitez, J. Alcaraz Maestre, P. Arce, C. Battilana, E. Calvo, M. Cerrada, M. Chamizo Llatas, N. Colino, B. De La Cruz, A. Delgado Peris, D. Dom??nguez V??quez, C. Fernandez Bedoya, J. P. Fern??ndez Ramos, A. Ferrando, J. Flix, M. C. Fouz, P. Garcia-Abia, O. Gonzalez Lopez, S. Goy Lopez, J. M. Hernandez, M. I. Josa, G. Merino, J. Puerta Pelayo, A. Quintario Olmeda, I. Redondo, L. Romero, J. Santaolalla, M. S. Soares, C. Willmott, C. Albaajar, G. Codispoti, J. F. de Troc??niz, H. Brun, J. Cuevas, J. Fernandez Menendez, S. Folgueras, I. Gonzalez Caballero, L. Lloret Iglesias, J. Piedra Gomez, J. A. Brochero Cifuentes, I. J. Cabrillo, A. Calderon, S. H. Chuang, J. Duarte Campderros, M. Felcini, M. Fernandez, G. Gomez, J. Gonzalez Sanchez, A. Graziano, C. Jorda, A. Lopez Virto, J. Marco, R. Marco, C. Martinez Rivero, F. Matorras, F. J. Munoz Sanchez, T. Rodrigo, A. Y. Rodr??guez-Marrero, A. Ruiz-Jimeno, L. Scodellaro, M. Sobron Sanudo, I. Vila, R. Vilar Cortabitarte, D. Abbaneo, P. Aspell, E. Auffray, G. Auzinger, M. Bachtis, J. Baechler, P. Baillon, A. H. Ball, D. Barney, J. F. Benitez, C. Bernet, W. Bialas, G. Bianchi, P. Bloch, A. Bocci, A. Bonato, C. Botta, H. Breuker, D. Campi, T. Camporesi, E. Cano, G. Cerminara, A. Charkiewicz, T. Christiansen, J. A. Coarasa Perez, B. Cur??, D. D'Enterria, A. Dabrowski, J. Daguin, A. De Roeck, S. Di Guida, M. Dobson, N. Dupont-Sagorin, A. Elliott-Peisert, M. Eppard, B. Frisch, W. Funk, A. Gaddi, M. Gastal, G. Georgiou, H. Gerwig, M. Giffels, D. Gigi, K. Gill, D. Giordano, M. Girone, M. Giunta, F. Glege, R. Gomez-Reino Garrido, P. Govoni, S. Gowdy, R. Guida, J. Gutleber, M. Hansen, P. Harris, C. Hartl, J. Harvey, B. Hegner, A. Hinzmamn, A. Honma, V. Innocente, P. Janot, K. Kaadze, E. Karavakis, K. Kloukinas, K. Kousouris, P. Lecoq, Y. J. Lee, P. Lenzi, R. Loos, C. Louren??o, N. Magini, T. M??ki, M. Malberti, L. Malgeri, M. Mannelli,. Observation of a new boson at a mass of 125 GeV with the CMS experiment at the LHC. *Physics Letters, Section B: Nuclear, Elementary Particle and High-Energy Physics*, 716(1):30–61, 2012.
- [6] S. Chatrchyan, V. Khachatryan, A. M. Sirunyan, A. Tumasyan, W. Adam, T. Bergauer, M. Dragicevic, J. Erö, C. Fabjan, M. Friedl, R. Fröhwirth, V. M. Ghete, C. Hartl, N. Hörmann, J. Hrubec, M. Jeitler, W. Kiesenhofer, V. Knünz, M. Krammer, I. Krätschmer, D. Liko, I. Mikulec, D. Rabady, B. Rahbaran, H. Rohringer, R. Schöfbeck, J. Strauss, A. Taurok, W. Treberer-Treberspurg, W. Waltenberger, C. E. Wulz, V. Mossolov, N. Shumeiko, J. Suarez Gonzalez, S. Alderweireldt, M. Bansal, S. Bansal, T. Cornelis, E. A. De Wolf, X. Janssen, A. Knutsson, S. Luyckx, L. Mucibello, S. Ochesanu, B. Roland, R. Rougny, H. Van Haevermaet, P. Van Mechelen, N. Van Remortel, A. Van Spilbeeck, F. Blekman, S. Blyweert, J. D'Hondt, N. Heracleous, A. Kalogeropoulos, J. Keaveney, T. J. Kim, S. Lowette, M. Maes, A. Olbrechts,

D. Strom, S. Tavernier, W. Van Doninck, P. Van Mulders, G. P. Van Onsem, I. Villella, C. Caillol, B. Clerbaux, G. De Lentdecker, L. Favart, A. P R Gay, A. Léonard, P. E. Marage, A. Mohammadi, L. Perniè, T. Reis, T. Seva, L. Thomas, C. Vander Velde, P. Vanlaer, J. Wang, V. Adler, K. Beernaert, L. Benucci, A. Cimmino, S. Costantini, S. Dildick, G. Garcia, B. Klein, J. Lellouch, J. McCartin, A. A. Ocampo Rios, D. Ryckbosch, S. Salva Diblen, M. Sigamani, N. Strobbe, F. Thyssen, M. Tytgat, S. Walsh, E. Yazgan, N. Zaganidis, S. Basegmez, C. Beluffi, G. Bruno, R. Castello, A. Caudron, L. Ceard, G. G. Da Silveira, C. Delaere, T. Du Pree, D. Favart, L. Forthomme, A. Giammanco, J. Hollar, P. Jez, M. Komm, V. Lemaitre, J. Liao, O. Militaru, C. Nuttens, D. Pagano, A. Pin, K. Piotrzkowski, A. Popov, L. Quertenmont, M. Selvaggi, M. Vidal Marono, J. M. Vizan Garcia, N. Belyi, T. Caebergs, E. Daubie, G. H. Hammad, G. A. Alves, M. Correa Martins Junior, T. Martins, M. E. Pol, M. H G Souza, W. L. Aldá Júnior, W. Carvalho, J. Chinellato, A. Custódio, E. M. Da Costa, D. De Jesus Damiao, C. De Oliveira Martins, S. Fonseca De Souza, H. Malbouisson, M. Malek, D. Matos Figueiredo, L. Mundim, H. Nogima, W. L. Prado Da Silva, J. Santao-lalla, A. Santoro, A. Sznajder, E. J. Tonelli Manganote, A. Vilela Pereira, C. A. Bernardes, F. A. Dias, T. R. Fernandez Perez Tomei, E. M. Gregores, C. Lagana, P. G. Mercadante, S. F. Novaes, Sandra S. Padula, V. Genchev, P. Iaydjiev, A. Marinov, S. Piperov, M. Rodozov, G. Sultanov, M. Vutova, A. Dimitrov, I. Glushkov, R. Hadjiiska, V. Kozhuharov, L. Litov, B. Pavlov, P. Petkov, J. G. Bian, G. M. Chen, H. S. Chen, M. Chen, R. Du, C. H. Jiang, D. Liang, S. Liang, X. Meng, R. Plestina, J. Tao, X. Wang, Z. Wang, C. Asawatangtrakuldee, Y. Ban, Y. Guo, Q. Li, W. Li, S. Liu, Y. Mao, S. J. Qian, D. Wang, L. Zhang, W. Zou, C. Avila, C. A. Carrillo Montoya, L. F. Chaparro Sierra, C. Florez, J. P. Gomez, B. Gomez Moreno, J. C. Sanabria, N. Godinovic, D. Lelas, D. Polic, I. Puljak, Z. Antunovic, M. Kovac, V. Brigljevic, K. Kadija, J. Luetic, D. Mekterovic, S. Morovic, L. Tikvica, A. Attikis, G. Mavromanolakis, J. Mousa, C. Nicolaou, F. Ptochos, P. A. Razis, M. Finger, M. Finger, A. A. Abdelalim, Y. Assran, S. Elgammal, A. Ellithi Kamel, M. A. Mahmoud, A. Radi, M. Kadastik, M. Müntel, M. Murumaa, M. Raidal, L. Rebane, A. Tiko, P. Eerola, G. Fedi, M. Voutilainen, J. Härkönen, V. Karimäki, R. Kinnunen, M. J. Kortelainen, T. Lampén, K. Lassila-Perini, S. Lehti, T. Lindén, P. Luukka, T. Mäenpää, T. Peltonen, E. Tuominen, J. Tuominiemi, E. Tuovinen, L. Wendland, T. Tuuva, M. Besancon, F. Couderc, M. Dejardin, D. Denegri, B. Fabbro, J. L. Faure, F. Ferri, S. Ganjour, A. Givernaud, P. Gras, G. Hamel De Monchenault, P. Jarry, E. Locci, J. Malcles, A. Nayak, J. Rander, A. Rosowsky, M. Titov, S. Baffioni, F. Beaudette, P. Busson, C. Charlot, N. Daci, T. Dahms, M. Dalchenko, L. Dobrzynski, A. Florent, R. Granier De Cassagnac, P. Miné, C. Mironov, I. N. Naranjo, M. Nguyen, C. Ochando, P. Paganini, D. Sabes, R. Salerno, Y. Sirois, C. Veelken, Y. Yilmaz, A. Zabi, J. L. Agram, J. Andrea, D. Bloch, J. M. Brom, E. C. Chabert, C. Collard, E. Conte, F. Drouhin, J. C. Fontaine, D. Gelé, U. Goerlach, C. Goetzmann, P. Juillet, A. C. Le Bihan, P. Van Hove, S. Gadrat, S. Beauceron, N. Beaupere, G. Boudoul, S. Brochet, J. Chasserat, R. Chierici, D. Contardo, P. Depasse, H. El Mamouni, J. Fan, J. Fay, S. Gascon, M. Gouzevitch, B. Ille, T. Kurca, M. Lethuillier, L. Mirabito, S. Perries, J. D. Ruiz Alvarez, L. Sgandurra, V. Sordini, M. Vander Donckt, P. Verdier, S. Viret, H. Xiao, Z. Tsamalaidze, C. Autermann, S. Beranek, M. Bontenackels, B. Calpas, M. Edelhoff, L. Feld, O. Hindrichs, K. Klein, A. Ostapchuk, A. Perieanu, F. Rau-pach, J. Sammet, S. Schael, D. Sprenger, H. Weber, B. Wittmer, V. Zhukov, M. Ata, J. Caudron, E. Dietz-Laursonn, D. Duchardt, M. Erdmann, R. Fischer, A. Güth, T. Hebbeker, C. Heidemann, K. Hoepfner, D. Klingebiel, S. Knutzen, P. Kreuzer, M. Merschmeyer, A. Meyer, M. Olschewski, K. Padeken, P. Papacz, H. Reithler, S. A. Schmitz, L. Sonnenschein, D. Teyssier, S. Thüer, M. Weber, V. Cherepanov,

Y. Erdogan, G. Flügge, H. Geenen, M. Geisler, W. Haj Ahmad, F. Hoehle, B. Kargoll, T. Kress, Y. Kuessel, J. Lingemann, A. Nowack, I. M. Nugent, L. Perchalla, O. Pooth, A. Stahl, I. Asin, N. Bartosik, J. Behr, W. Behrenhoff, U. Behrens, A. J. Bell, M. Bergholz, A. Bethani, K. Borras, A. Burgmeier, A. Cakir, L. Calligaris, A. Campbell, S. Choudhury, F. Costanza, C. Diez Pardos, S. Dooling, T. Dorland, G. Eckerlin, D. Eckstein, T. Eichhorn, G. Flucke, A. Geiser, A. Grebenyuk, P. Gunnellini, S. Habib, J. Hauk, G. Hellwig, M. Hempel, D. Horton, H. Jung, M. Kasemann, P. Katsas, J. Kieseler, C. Kleinwort, M. Krämer, D. Krücker, W. Lange, J. Leonard, K. Lipka, W. Lohmann, B. Lutz, R. Mankel, I. Marfin, I. A. Melzer-Pellmann, A. B. Meyer, J. Mnich, A. Mussgiller, S. Naumann-Emme, O. Novgorodova, F. Nowak, H. Perrey, A. Petrukhin, D. Pitzl, R. Placakyte, A. Raspereza, P. M. Ribeiro Cipriano, C. Riedl, E. Ron, M. Ö Sahin, J. Salfeld-Nebgen, R. Schmidt, T. Schoerner-Sadenius, M. Schröder, M. Stein, A. D R Vargas Trevino, R. Walsh, C. Wissing, M. Aldaya Martin, V. Blobel, H. Enderle, J. Erfle, E. Garutti, K. Goebel, M. Görner, M. Gosselink, J. Haller, R. S. Höing, H. Kirschenmann, R. Klanner, R. Kogler, J. Lange, I. Marchesini, J. Ott, T. Peiffer, N. Pietsch, D. Rathjens, C. Sander, H. Schettler, P. Schleper, E. Schlieckau, A. Schmidt, M. Seidel, J. Sibille, V. Sola, H. Stadie, G. Steinbrück, D. Troendle, E. Usai, L. Vanelderden, C. Barth, C. Baus, J. Berger, C. Böser, E. Butz, T. Chwalek, W. De Boer, A. Descroix, A. Dierlamm, M. Feindt, M. Guthoff, F. Hartmann, T. Hauth, H. Held, K. H. Hoffmann, U. Husemann, I. Katkov, A. Kornmayer, E. Kuznetsova, P. Lobelle Pardo, D. Martschei, M. U. Mozer, Th Müller, M. Niegel, A. Nürnberg, O. Oberst, G. Quast, K. Rabbertz, F. Ratnikov, S. Röcker, F. P. Schilling, G. Schott, H. J. Simonis, F. M. Stober, R. Ulrich, J. Wagner-Kuhr, S. Wayand, T. Weiler, R. Wolf, M. Zeise, G. Anagnostou, G. Daskalakis, T. Geralis, S. Kesisoglou, A. Kyriakis, D. Loukas, A. Markou, C. Markou, E. Ntomari, A. Psallidas, I. Topsis-Giotis, L. Gouskos, A. Panagiotou, N. Saoulidou, E. Stiliaris, X. Aslanoglou, I. Evangelou, G. Flouris, C. Foudas, P. Kokkas, N. Manthos, I. Papadopoulos, E. Paradas, G. Bencze, C. Hajdu, P. Hidas, D. Horvath, F. Sikler, V. Veszpremi, G. Vesztregombi, A. J. Zsigmond, N. Beni, S. Czellar, J. Molnar, J. Palinkas, Z. Szillasi, J. Karancsi, P. Raics, Z. L. Trocsanyi, B. Ujvari, S. K. Swain, S. B. Beri, V. Bhatnagar, N. Dhingra, R. Gupta, M. Kaur, M. Z. Mehta, M. Mittal, N. Nishu, A. Sharma, J. B. Singh, Ashok Kumar, Arun Kumar, S. Ahuja, A. Bhardwaj, B. C. Choudhary, A. Kumar, S. Malhotra, M. Naimuddin, K. Ranjan, P. Saxena, V. Sharma, R. K. Shivpuri, S. Banerjee, S. Bhattacharya, K. Chatterjee, S. Dutta, B. Gomber, Sa Jain, Sh Jain, R. Khurana, A. Modak, S. Mukherjee, D. Roy, S. Sarkar, M. Sharan, A. P. Singh, A. Abdulsalam, D. Dutta, S. Kailas, V. Kumar, A. K. Mohanty, L. M. Pant, P. Shukla, A. Topkar, T. Aziz, R. M. Chatterjee, S. Ganguly, S. Ghosh, M. Guchait, A. Gurtu, G. Kole, S. Kumar, M. Maity, G. Majumder, K. Mazumdar, G. B. Mohanty, B. Parida, K. Sudhakar, N. Wickramage, S. Banerjee, S. Dugad, H. Arfaei, H. Bakhshiansohi, H. Behnamian, S. M. Etesami, A. Fahim, A. Jafari, M. Khakzad, M. Mohammadi Najafabadi, M. Naseri, S. Paktnat Mehdiabadi, B. Safarzadeh, M. Zeinali, M. Grunewald, M. Abbrescia, L. Barbone, C. Calabria, S. S. Chhibra, A. Colaleo, D. Creanza, N. De Filippis, M. De Palma, L. Fiore, G. Iaselli, G. Maggi, M. Maggi, B. Marangelli, S. My, S. Nuzzo, N. Pacifico, A. Pompili, G. Pugliese, R. Radogna, G. Selvaggi, L. Silvestris, G. Singh, R. Venditti, P. Verwilligen, G. Zito, G. Abbiendi, A. C. Benvenuti, D. Bonacorsi, S. Braibant-Giacomelli, L. Brigliadori, R. Campanini, P. Capiluppi, A. Castro, F. R. Cavallo, G. Codispoti, M. Cuffiani, G. M. Dallavalle, F. Fabbrini, A. Fanfani, D. Fasanella, P. Giacomelli, C. Grandi, L. Guiducci, S. Marcellini, G. Masetti, M. Meneghelli, A. Montanari, F. L. Navarria, F. Odorici, A. Perrotta, F. Primavera, A. M. Rossi, T. Rovelli, G. P. Siroli, N. Tosi, R. Travaglini, S. Albergo,

G. Cappello, M. Chiorboli, S. Costa, F. Giordano, R. Potenza, A. Tricomi, C. Tuve, G. Barbagli, V. Ciulli, C. Civinini, R. D'Alessandro, E. Focardi, E. Gallo, S. Gonzi, V. Gori, P. Lenzi, M. Meschini, S. Paoletti, G. Sguazzoni, A. Tropiano, L. Benussi, S. Bianco, F. Fabbri, D. Piccolo, P. Fabbricatore, R. Ferretti, F. Ferro, M. Lo Vetere, R. Musenich, E. Robutti, S. Tosi, A. Benaglia, M. E. Dinardo, S. Fiorendi, S. Gennai, A. Ghezzi, P. Govoni, M. T. Lucchini, S. Malvezzi, R. A. Manzoni, A. Martelli, D. Menasce, L. Moroni, M. Paganoni, D. Pedrini, S. Ragazzi, N. Redaelli, T. Tabarelli De Fatis, S. Buontempo, N. Cavallo, F. Fabozzi, A. O M Iorio, L. Lista, S. Meola, M. Merola, P. Paolucci, P. Azzi, N. Bacchetta, D. Bisello, A. Branca, R. Carlin, P. Checchia, T. Dorigo, U. Dosselli, F. Fanzago, M. Galanti, F. Gasparini, U. Gasparini, P. Giubilato, F. Gonella, A. Gozzelino, K. Kanishchev, S. Lacaprara, I. Lazzizzera, M. Margoni, A. T. Meneguzzo, J. Pazzini, N. Pozzobon, P. Ronchese, F. Simonetto, E. Torassa, M. Tosi, P. Zotto, A. Zucchetta, G. Zumerle, M. Gabusi, S. P. Ratti, C. Riccardi, P. Vitulo, M. Biasini, G. M. Bilei, L. Fanò, P. Lariccia, G. Mantovani, M. Menichelli, F. Romeo, A. Saha, A. Santocchia, A. Spiezia, K. Androsov, P. Azzurri, G. Bagliesi, J. Bernardini, T. Boccali, G. Broccolo, R. Castaldi, M. A. Ciocci, R. Dell'Orso, F. Fiori, L. Foà, A. Giassi, M. T. Grippo, A. Kraan, F. Ligabue, T. Lomtadze, L. Martini, A. Messineo, C. S. Moon, F. Palla, A. Rizzi, A. Savoy-Navarro, A. T. Serban, P. Spagnolo, P. Squillaciotti, R. Tenchini, G. Tonelli, A. Venturi, P. G. Verdini, C. Vernieri, L. Barone, F. Cavallari, D. Del Re, M. Diemoz, M. Grassi, C. Jorda, E. Longo, F. Margaroli, P. Meridiani, F. Micheli, S. Nourbakhsh, G. Organtini, R. Paramatti, S. Rahatlou, C. Rovelli, L. Soffi, P. Traczyk, N. Amapane, R. Arcidiacono, S. Argiro, M. Arneodo, R. Bellan, C. Biino, N. Cartiglia, S. Casasso, M. Costa, A. Degano, N. Demaria, L. Finco, M. Machet, C. Mariotti, S. Maselli, E. Migliore, V. Monaco, M. Musich, M. M. Obertino, G. Ortona, L. Pacher, N. Pastrone, M. Pelliccioni, G. L. Pinna Angioni, A. Romero, R. Sacchi, A. Solano, A. Staiano, S. Belforte, V. Candelise, M. Casarsa, F. Cossutti, G. Della Ricca, B. Gobbo, C. La Licata, M. Marone, D. Montanino, A. Penzo, A. Schizzi, T. Umer, A. Zanetti, S. Chang, T. Y. Kim, S. K. Nam, D. H. Kim, G. N. Kim, J. E. Kim, D. J. Kong, S. Lee, Y. D. Oh, H. Park, D. C. Son, J. Y. Kim, Zero J. Kim, S. Song, S. Choi, D. Gyun, B. Hong, M. Jo, H. Kim, Y. Kim, K. S. Lee, S. K. Park, Y. Roh, M. Choi, J. H. Kim, C. Park, I. C. Park, S. Park, G. Ryu, Y. Choi, Y. K. Choi, J. Goh, M. S. Kim, E. Kwon, B. Lee, J. Lee, S. Lee, H. Seo, I. Yu, A. Juodagalvis, J. R. Komaragiri, H. Castilla-Valdez, E. De La Cruz-Burelo, I. Heredia-De La Cruz, R. Lopez-Fernandez, J. Martínez-Ortega, A. Sanchez-Hernandez, L. M. Villasenor-Cendejas, S. Carrillo Moreno, F. Vazquez Valencia, H. A. Salazar Ibarguen, E. Casimiro Linares, A. Morelos Pineda, D. Kroccheck, P. H. Butler, R. Doesburg, S. Reucroft, H. Silverwood, M. Ahmad, M. I. Asghar, J. Butt, H. R. Hoorani, S. Khalid, W. A. Khan, T. Khurshid, S. Qazi, M. A. Shah, M. Shoaib, H. Bialkowska, M. Bluj, B. Boimska, T. Frueboes, M. Górski, M. Kazana, K. Nawrocki, K. Romanowska-Rybinska, M. Szleper, G. Wrochna, P. Zalewski, G. Brona, K. Bunkowski, M. Cwiok, W. Dominiak, K. Doroba, A. Kalinowski, M. Konecki, J. Krolikowski, M. Misiura, W. Woluszak, P. Bargassa, C. Beirão Da Cruz E Silva, P. Faccioli, P. G. Ferreira Parracho, M. Gallinaro, F. Nguyen, J. Rodrigues Antunes, J. Seixas, J. Varela, P. Vischia, I. Golutvin, I. Gorbunov, A. Kamenev, V. Karjavin, V. Konoplyanikov, G. Kozlov, A. Lanev, A. Malakhov, V. Matveev, P. Moisenz, V. Palichik, V. Perelygin, M. Savina, S. Shmatov, S. Shulha, N. Skatchkov, V. Smirnov, A. Zarubin, V. Golovtsov, Y. Ivanov, V. Kim, P. Levchenko, V. Murzin, V. Oreshkin, I. Smirnov, V. Sulimov, L. Uvarov, S. Vavilov, A. Vorobyev, An Vorobyev, Yu Andreev, A. Dermenev, S. Ginenko, N. Golubev, M. Kirsanov, N. Krasnikov, A. Pashenkov, D. Tlisov, A. Toropin, V. Epshteyn, V. Gavrilov, N. Lychkovskaya, V. Popov, G. Safronov, S. Semenov,

A. Spiridonov, V. Stolin, E. Vlasov, A. Zhokin, V. Andreev, M. Azarkin, I. Dremin, M. Kirakosyan, A. Leonidov, G. Mesyats, S. V. Rusakov, A. Vinogradov, A. Belyaev, E. Boos, V. Bunichev, M. Dubinin, L. Dudko, A. Ershov, A. Gribushin, V. Klyukhin, O. Kodolova, I. Lokhtin, S. Obraztsov, S. Petrushanko, V. Savrin, I. Azhgirey, I. Bayshev, S. Bitioukov, V. Kachanov, A. Kalinin, D. Konstantinov, V. Krychkine, V. Petrov, R. Ryutin, A. Sobol, L. Tourtchanovitch, S. Troshin, N. Tyurin, A. Uzunian, A. Volkov, P. Adzic, M. Djordjevic, M. Ekmedzic, J. Milosevic, M. Aguilar-Benitez, J. Alcaraz Maestre, C. Battilana, E. Calvo, M. Cerrada, M. Chamizo Llatas, N. Colino, B. De La Cruz, A. Delgado Peris, D. Domínguez Vázquez, C. Fernandez Bedoya, J. P. Fernández Ramos, A. Ferrando, J. Flix, M. C. Fouz, P. Garcia-Abia, O. Gonzalez Lopez, S. Goy Lopez, J. M. Hernandez, M. I. Josa, G. Merino, E. Navarro De Martino, J. Puerta Pelayo, A. Quintario Olmeda, I. Redondo, L. Romero, M. S. Soares, C. Willmott, C. Albajar, J. F. De Trocóniz, H. Brun, J. Cuevas, J. Fernandez Menendez, S. Folgueras, I. Gonzalez Caballero, L. Lloret Iglesias, J. A. Brochero Cifuentes, I. J. Cabrillo, A. Calderon, S. H. Chuang, J. Duarte Campderros, M. Fernandez, G. Gomez, J. Gonzalez Sanchez, A. Graziano, A. Lopez Virto, J. Marco, R. Marco, C. Martinez Rivero, F. Matorras, F. J. Munoz Sanchez, J. Piedra Gomez, T. Rodrigo, A. Y. Rodríguez-Marrero, A. Ruiz-Jimeno, L. Scodellaro, I. Vila, R. Vilar Cortabitarte, D. Abbanco, E. Auffray, G. Auzinger, M. Bachtis, P. Baillon, A. H. Ball, D. Barney, J. Bendavid, L. Benhabib, J. F. Benitez, C. Bernet, G. Bianchi, P. Bloch, A. Bocci, A. Bonato, O. Bondu, C. Botta, H. Breuker, T. Camporesi, G. Cerminara, T. Christiansen, J. A. Coarasa Perez, S. Colafranceschi, M. D'Alfonso, D. D'Enterria, A. Dabrowski, A. David, F. De Guio, A. De Roeck, S. De Visscher, S. Di Guida, M. Dobson, N. Dupont-Sagorin, A. Elliott-Peisert, J. Eugster, G. Franzoni, W. Funk, M. Giffels, D. Gigi, K. Gill, M. Girone, M. Giunta, F. Glege, R. Gomez-Reino Garrido, S. Gowdy, R. Guida, J. Hammer, M. Hansen, P. Harris, V. Innocente, P. Janot, E. Karavakis, K. Kousouris, K. Krajczar, P. Lecoq, C. Lourenço, N. Magini, L. Malgeri, M. Mannelli, L. Masetti, F. Meijers, S. Mersi, E. Meschi, F. Moortgat, M. Mulders, P. Musella, L. Orsini, E. Palencia Cortezon, E. Perez, L. Perrozzi, A. Petrilli, G. Petrucciani, A. Pfeiffer, M. Pierini, M. Pimiä, D. Piparo, M. Plagge, A. Racz, W. Reece, G. Rolandi, M. Rovere, H. Sakulin, F. Santanastasio, C. Schäfer, C. Schwick, S. Sekmen, A. Sharma, P. Siegrist, P. Silva, M. Simon, P. Sphicas, J. Steggemann, B. Stieger, M. Stoye, A. Tsirou, G. I. Veres, J. R. Vlimant, H. K. Wöhri, W. D. Zeuner, W. Bertl, K. Deiters, W. Erdmann, R. Horisberger, Q. Ingram, H. C. Kaestli, S. König, D. Kotlinski, U. Langenegger, D. Renker, T. Rohe, F. Bachmair, L. Bäni, L. Bianchini, P. Bortignon, M. A. Buchmann, B. Casal, N. Chanon, A. Deisher, G. Dissertori, M. Dittmar, M. Donegà, M. Dünser, P. Eller, C. Grab, D. Hits, W. Lustermann, B. Mangano, A. C. Marini, P. Martinez Ruiz Del Arbol, D. Meister, N. Mohr, C. Nägeli, P. Nef, F. Nessi-Tedaldi, F. Pandolfi, L. Pape, F. Pauss, M. Peruzzi, M. Quittnat, F. J. Ronga, M. Rossini, A. Starodumov, M. Takahashi, L. Tauscher, K. Theofilatos, D. Treille, R. Wallny, H. A. Weber, C. Amsler, V. Chiochia, A. De Cosa, C. Favaro, A. Hinzmamn, T. Hreus, M. Ivova Rikova, B. Kilminster, B. Millan Mejias, J. Ngadiuba, P. Robmann, H. Snoek, S. Taroni, M. Verzetti, Y. Yang, M. Cardaci, K. H. Chen, C. Ferro, C. M. Kuo, S. W. Li, W. Lin, Y. J. Lu, R. Volpe, S. S. Yu, P. Bartalini, P. Chang, Y. H. Chang, Y. W. Chang, Y. Chao, K. F. Chen, P. H. Chen, C. Dietz, U. Grundler, W. S. Hou, Y. Hsiung, K. Y. Kao, Y. J. Lei, Y. F. Liu, R. S. Lu, D. Majumder, E. Petrakou, X. Shi, J. G. Shiu, Y. M. Tzeng, M. Wang, R. Wilken, B. Asavapibhop, N. Suwonjandee, A. Adiguzel, M. N. Bakirci, S. Cerci, C. Dozen, I. Dumanoglu, E. Eskut, S. Girgis, G. Gokbulut, E. Gurpinar, I. Hos, E. E. Kangal, A. Kayis Topaksu, G. Onengut, K. Ozdemir, S. Ozturk, A. Polatoz, K. Sogut, D. Sunar Cerci, B. Tali, H. Topakli,

- M. Vergili, I. V. Akin, T. Aliev, B. Bilin, S. Bilmis, M. Deniz, H. Gamsizkan, A. M. Guler, G. Karapinar, K. Ocalan, A. Ozpineci, M. Serin, R. Sever, U. E. Surat, M. Yalvac, M. Zeyrek, E. Glmez, B. Isildak, M. Kaya, O. Kaya, S. Ozkorucuklu, H. Bahtiyar, E. Barlas, K. Cankocak, Y. O. Gnaydin, F. I. VardarII, M. Ycel, L. Levchuk, P. Sorokin, J. J. Brooke, E. Clement, D. Cussans, H. Flacher, R. Frazier, J. Goldstein, M. Grimes, G. P. Heath, H. F. Heath, J. Jacob, L. Kreczko, C. Lucas, Z. Meng, D. M. Newbold, S. Paramesvaran, A. Poll, S. Senkin, V. J. Smith, T. Williams, K. W. Bell, A. Belyaev, C. Brew, R. M. Brown, D. J A Cockerill, J. A. Coughlan, K. Harder, S. Harper, J. Ilic, E. Olaiya, D. Petyt, C. H. Shepherd-Themistocleous, A. Thea, I. R. Tomalin, W. J. Womersley, S. D. Worm, M. Baber, R. Bainbridge, O. Buchmuller, D. Burton, D. Colling, N. Cripps, M. Cutajar, P. Dauncey, G. Davies, M. Della Negra, W. Ferguson, J. Fulcher, D. Futyan, A. Gilbert, A. Guneratne Bryer, G. Hall, Z. Hatherell, J. Hays, G. Iles, M. Jarvis, G. Karapostoli, M. Kenzie, R. Lane, R. Lucas, L. Lyons, A. M. Magnan, J. Marrouche, B. Mathias, R. Nandi, J. Nash, A. Nikitenko, J. Pela, M. Pesaresi, K. Petridis, M. Pioppi, D. M. Raymond, S. Rogeresson, A. Rose, C. Seez, P. Sharp, A. Sparrow, A. Tapper, M. Vazquez Acosta, T. Virdee, S. Wakefield, N. Wardle, J. E. Cole, P. R. Hobson, A. Khan, P. Kyberd, D. Leggat, D. Leslie, W. Martin, I. D. Reid, P. Symonds, L. Teodorescu, M. Turner, J. Dittmann, K. Hatakeyama, A. Kasmi, H. Liu, T. Scarborough, O. Charaf, S. I. Cooper, C. Henderson, P. Rumerio, A. Avetisyan, T. Bose, C. Fantasia, A. Heister, P. Lawson, D. Lazic, J. Rohlf, D. Sperka, J. St. John, L. Sulak, J. Alimena, S. Bhattacharya, G. Christopher, D. Cutts, Z. Demiragli, A. Ferapontov, A. Garabedian, U. Heintz, S. Jabeen, G. Kukartsev, E. Laird, G. Landsberg, M. Luk, M. Narain, M. Segala, T. Sinthuprasith, T. Speer, J. Swanson, R. Breedon, G. Breto, M. Calderon De La Barca Sanchez, S. Chauhan, M. Chertok, J. Conway, R. Conway. Measurement of the properties of a Higgs boson in the four-lepton final state. *Physical Review D - Particles, Fields, Gravitation and Cosmology*, 89(9):1–45, 2014.
- [7] Carlo Giunti and Chung W. Kim. Fundamentals of Neutrino Physics and Astrophysics. *Fundamentals of Neutrino Physics and Astrophysics*, pages 1–728, 2010.
- [8] Joseph Grange and Teppei Katori. Charged current quasi-elastic cross-section measurements in MiniBooNE. *Modern Physics Letters A*, 29(12):1430011, apr 2014.
- [9] Hirokazu Ishino. Gadolinium study for Super-Kamiokande. pages 1–4, 2009.
- [10] Teppei Katori. Meson Exchange Current (MEC) Models in Neutrino Interaction Generators. page 6, 2013.
- [11] M. Martini, M. Ericson, G. Chanfray, and J. Marteau. Neutrino and antineutrino quasielastic interactions with nuclei. *Physical Review C - Nuclear Physics*, 81(4):1–5, 2010.
- [12] MiniBooNE Collaboration. The Neutrino Flux prediction at MiniBooNE. *Physical Review D - Particles, Fields, Gravitation and Cosmology*, 79(7):1–38, jun 2008.
- [13] Y. Nakajima, J. L. Alcaraz-Aunion, S. J. Brice, L. Bugel, J. Catala-Perez, G. Cheng, J. M. Conrad, Z. Djurcic, U. Dore, D. A. Finley, A. J. Franke, C. Giganti, J. J. Gomez-Cadenas, P. Guzowski, A. Hanson, Y. Hayato, K. Hiraide, G. Jover-Manas, G. Karagiorgi, T. Katori, Y. K. Kobayashi, T. Kobilarcik, H. Kubo, Y. Kurimoto, W. C. Louis, P. F. Loverre, L. Ludovici, K. B M Mahn, C. Mariani, S. Masuika, K. Matsuoka, V. T. McGary, W. Metcalf, G. B. Mills, G. Mitsuka, Y. Miyachi, S. Mizugashira, C. D. Moore, T. Nakaya, R. Napora, P. Nienaber, D. Orme, M. Otani, A. D. Russell, F. Sanchez, M. H. Shaevitz, T. A. Shibata, M. Sorel, R. J. Stefanski, H. Takei, H. K.

- Tanaka, M. Tanaka, R. Tayloe, I. J. Taylor, R. J. Tesarek, Y. Uchida, R. Van De Water, J. J. Walding, M. O. Wascko, H. B. White, M. Yokoyama, G. P. Zeller, and E. D. Zimmerman. Measurement of inclusive charged current interactions on carbon in a few-GeV neutrino beam. *Physical Review D - Particles, Fields, Gravitation and Cosmology*, 83(1):1–19, 2011.
- [14] R. A. Smith and E. J. Moniz. Neutrino Reactions on Nuclear Targets. *Nuclear Physics, Section B*, 43(2):605–622, 1972.
- [15] Jan T. Sobczyk. Multinucleon ejection model for Meson Exchange Current neutrino interactions. 2012.